ABSTRACT

ANNAMAREDDY, VENKATA AJAY KRISHNA CHOUDARY. Dynamics and Tolerance of Superionics in Extreme Environment. (Under the direction of Prof. Jacob Eapen.)

Superionic conductors are multi-component solid-state systems in which one sub-lattice exhibits exceptional ionic conductivity, which is comparable to molten state; among other things, the high ionic conductivity facilitates their use as solid-state electrolytes. Uranium di-oxide (UO_2) – the material of choice for fuel in most nuclear reactors – also shows superionic behavior, although very little is understood currently on the fast ion transport in UO_2, and its implication. This dissertation aims to provide a better understanding of the dynamical characteristics of superionic conductors under both equilibrium and non-equilibrium thermodynamic conditions.

In the first part, the emphasis is on equilibrium fluctuations and associated properties of Type II superionic conductors. Using atomistic simulations as well as available neutron and x-ray scattering data, the order-disorder transition or onset of superionic state for Type II conductors at a certain characteristic temperature (T_α) is first revealed. T_α marks a structural and kinetic crossover from a crystalline state to a semi-ordered state and is clearly different from the well-known thermodynamic superionic transition (T_λ). Though not favored by entropic forces, collective and cooperative dynamical effects, reminiscent of glassy states, are manifested in the temperature range spanned by T_α and T_λ. Using atomistic simulations, dynamical heterogeneity (DH) – presence of clustered mobile and immobile regions in a static-homogeneous system – a ubiquitous feature of supercooled liquids and glassy states, is shown to germinate at T_α. Using reliable metrics, the DH is shown to strengthen with increasing temperature, peak at an intermediate temperature between T_α and T_λ, and then recede. This manifestation of DH in superionics markedly differs from that in supercooled liquids through its initial growth against the destabilizing entropic barriers.

Atomistic simulations further show that DH in superionics arises from facilitated dynamics, or the phenomenon of dynamic facilitation (DF). Using mobility transfer function,

which gives the probability of a neighbor of a mobile ion becoming mobile relative to that of a random ion becoming mobile, it is shown that mobility propagates continuously to the neighboring ions with the strength of the DF increasing at the order-disorder temperature (T_α), exhibiting a maximum at an intermediate temperature, and then decreasing as the temperature approaches T_λ. This waxing and waning behavior with temperature is nearly identical to the variation of DH. Thus the close correspondence between DH and DF strongly indicates that DF underpins the heterogeneous dynamics in Type II superionic conductors.

In a dynamically facilitated system, a jammed region can become unjammed only if it is physically adjacent to a mobile region. Remarkably, a string-like displacement of ions, the quintessential mode of particle mobility in jammed systems, is shown to operate in Type II superionics as well. The probability distribution of the length of the string is shown to vary exponentially, which is identical to that observed in supercooled and jammed states. Thus the demonstration of DH, DF and string-like cooperative ionic displacements in superionics that closely parallel the dynamic characteristics of supercooled liquids and glassy states, significantly augments the already existing but scant list of phenomenological similarities between these two distinct types of materials.

The second part of this dissertation deals with non-equilibrium displacement-cascade simulations of UO_2 that is used as a nuclear fuel. UO_2 is known to resist amorphization even when subjected to intense nuclear radiations; analysis based on structure and energy does explain this behavior from a thermodynamic perspective. Radiation is inherently dynamic (non-equilibrium), and thus it is pertinent to understand the dynamics of the displaced ions during the annealing process. In this dissertation, the mechanism of dynamic recovery following a radiation knock at the atomistic level is investigated. It is shown that oxygen ions following a radiation perturbation exhibit correlated motion, which is similar to that in high temperature superionic state. Quite remarkably, the displaced oxygen ions also undergo fast recovery to their native lattice sites through collective string-like displacements that show an exponential distribution. Thus the superionic characteristics of UO_2 under equilibrium conditions are also instrumental in fast defect recovery following a radiation perturbation.

Dynamics and Tolerance of Superionics in Extreme Environment

by
Venkata Ajay Krishna Choudary Annamareddy

A dissertation submitted to the Graduate Faculty of
North Carolina State University
in partial fulfillment of the
requirements for the Degree of
Doctor of Philosophy

Nuclear Engineering

Raleigh, North Carolina

March 2016

APPROVED BY:

Prof. Jacob Eapen Chair, Advisory Committee	Prof. Korukonda Linga Murty Advisory Committee
Prof. Jerzy Bernholc Advisory Committee	Prof. Ronald Scattergood Advisory Committee

DEDICATION

To all my teachers.

To my family.

To Rajkumar Hirani, for professing to PURSUE EXCELLENCE (3 idiots).

BIOGRAPHY

Ajay Annamareddy was born in Tadepalligudem, Andhra Pradesh, India, as the youngest of three children in 1984 to Veera Brahmam and Suryakumari. He received an undergraduate science degree in his hometown and went on to pursue a Master's degree in Nuclear Physics from Andhra University, Visakhapatnam. With diligence and passion, he performed well in the academics and subsequently joined IIT-Kanpur for the Master's program in Nuclear Engineering. After completing his studies at IIT-Kanpur, he came to North Carolina State University for pursuing a PhD degree in Nuclear Engineering during the Fall of 2010. Here, he began learning the wonderful discipline of materials science and got the opportunity to apply his knowledge in physics and computer programming to work on *Materials Simulations.* He married his sweetheart, Sandhya, in 2011 and the couple was blessed with a daughter, Akshara, in 2014.

ACKNOWLEDGEMENTS

A long-term commitment to PhD requires a lot of guidance and motivation from different sources, and I would like to take this opportunity to thank my guru and research advisor, *Prof. Jacob Eapen*, for his many years of effort in guiding me through this work. Apart from being a great mentor, *Prof. Eapen* inculcated values such as ethics in research, time-management, and a strong sense of commitment towards work among his group. I hope he continues to be a role-model for many in the future.

I would also like to thank all my committee members *Professors K. L. Murty*, *Jerzy Bernholc*, and *Ronald Scattergood* for serving in my dissertation committee. These are researchers that I look up to, and I deeply appreciate the time and effort they have invested in my dissertation. I further would like to thank *Prof. K. L. Murty* for supporting me in my final semester.

The diverse classes that I have attended during this journey have helped me immeasurably in widening my knowledge. Hopefully, I will be able to pursue research in these areas in the future. NC STATE is privileged with several excellent teachers and I would like to thank all those I have greatly benefited from, in the chronological order – *Professors Ayman Hawari* (Nuclear Engineering), *Dmitriy Anistratov* (Nuclear Engineering), *Jacob Eapen* (Nuclear Engineering), *Jerzy Bernholc* (Physics), *Keith Gubbins* (Chemical Engineering), *Ilse Ipsen* (Math), *Douglas Irving* (Materials Science and Engineering), and *Elena Jakubikova* (Chemistry).

PhD students tend to spend significant time in their offices and I am lucky to have wonderful colleagues to befriend with, as well as in getting a lot of support on research. *Walid* (Mohamed) and *Xiaojun* (Mei), as senior members in the group, were very helpful when I started on my research. I went on to further develop the *Rbox* molecular dynamics (MD) program, which they have initiated, and subsequently utilized it for most of my PhD work.

Avinash (Dongare), who is now a faculty member at the University of Connecticut, was exceptional as a mentor, even though I was only able to work alongside him for a few months. Oh boy! I really wished to have worked longer with him. Next, comes my friends in the Radiant group: *Anant* (Raj), *Jin* (Wang) and I started at the same time at NC STATE and they were always there to teach me various things I was not good at. *Anant* would also be completing soon and I am positive that he would go places. *Jin* is currently working on his PhD with *Avinash* at UCONN and I wish him all the best. I can never forget all the good times I had with *Prithwish* (Nandi), while he was a post-doctoral researcher in our group. We frequented the shops at the Hillsborough Street, and sadly those enjoyable moments would never come back again. I learned so many things from *Prithwish*, especially on materials science and scripting in Linux. I thank him for all his support and wish him good luck in the future. In *Dillon* (Sanders), I see vast potential as a researcher and I would like to see him succeed immensely. We have had a great time talking about different things, especially on tennis (of course, he did most of the talking); we also played tennis on rare occasions. I also would like to thank *William* (Lowe) for his help on numerous occasions and wish him good luck in the future.

Other IIT-Kanpur family members in the department also deserve special mention here: *Rudro* (-dip Majumdar), *Paridhi* (Athe), *Arka* (Datta), and *Shefali* (Saxena). Thank you guys! I certainly had a wonderful time with all of you. The staff in the NE department had been very cordial and had helped us in many way – many thanks to *Ganga* (Atukorala), *Lisa* (Marshall), and *Robert* (Green). *Chintan* (Kanani), as the IT specialist for the department, was always our go-to man if something went wrong with our office computers. He saved us on more than a few occasions. Thank you very much, *Chintan*.

PhD life quickly becomes uneventful without great friends and I would like to thank all of them: *Arun* (Kumar Kadavelugu), *Prasen* (-jit Khanikar), *Boopa* (-thy Kombaiah) and *Viji*, *Samir* (Hazra), *Kasu* (-naidu Vechalapu) and *Jayasri*, *Srinivas* (Rao Singamaneni) and *Bharathi akka* and *Siddhu*, *Lucky* (Mehra) and *Sushi* (-la Chaudhari). We had countless great

times together and they had always motivated me with their brilliance at work. I hope we will stay in close touch, forever!

Back home (in India), there are numerous people I would need to acknowledge. First and foremost, my mentor *Professor Munshi* at IIT-K was most encouraging during my Master's and during the time when I was applying for PhD programs in the US. Thank you, sir! I would also like to thank *Professors M. L. N. Raju, K. Premchand,* and *S. Bhuloka Reddy*, who were my professors at the Andhra University. I would always cherish my time with them.

My *parents*, who let me pursue whatever I wanted to, are especially to be thanked for. Special thanks to my *Amma* (Mother), who incessantly urged me to study hard during childhood, a lot of times in vain; she can rightfully take the credit for my success now☺. My *mother-in-law* took care of our baby for almost a year in Raleigh and presently raises her in India, and she deserves a big Thanks from all of my family. Both my *sisters* (Uma *Akka* and Maruthi *Devi*) and their families have been supportive over the years. I love you all!

Finally, I would want to express my deepest appreciation to my darling wife *Sandhya*. By taking care of all the household chores, as she was managing her own PhD studies, she ensured that I could work that *extra*-minute without disruptions – I cannot express how proud I am of her! And our little girl, *Akshara*, born almost a year before our graduation, brought the greatest joy to our family.

TABLE OF CONTENTS

LIST OF FIGURES

LIST OF TABLES

Chapter 1: INTRODUCTION

Superionic or fast-ion conductors are multi-component systems that are characterized by rapid diffusion of one of the sub-lattices at temperatures considerably lower than their melting temperatures [1]. Hence, superionic materials exhibit outstanding ionic conductivities within the solid state and their conductivities often reach values that are comparable to those in the liquid state [2]. This facilitates their utilization in several important applications like fuel cells [3], high-energy-density batteries [4], hydrogen storage [5] and thermoelectrics [6]. Uranium di-oxide (UO_2) – the fuel material of choice in most nuclear reactors – also shows superionic behavior, although very little is understood currently on the fast ion transport in UO_2, and its implication.

This dissertation aims to investigate the dynamical properties of superionic conductors under both equilibrium and radiative (non-equilibrium) conditions. The general characteristics and the properties of superionic conductors are first described in this chapter, followed by a general discussion on the motivation for the current research. And finally, the objective and the outline of the dissertation are elucidated.

1.1 Superionic conductors

Michael Faraday has been credited with the discovery of superionic conductors when he uncovered extremely high ionic conductivities in β-PbF_2 and Ag_2S [2] within the solid state; Ag_2S is now known to be a mixed ionic/electronic conductor. Superionic conductors are classified into two broad categories depending on the nature of transition to the highly conducting state. Type I conductors exhibit an abrupt increase in the conductivity by several orders of magnitude at a critical temperature that corresponds to a thermodynamic phase

change, whereas in Type II conductors the conductivity increases gradually over a broad temperature range [7]. Figure 1.1 shows the temperature variation of ionic conductivity for model Type I and Type II superionic conductors (AgI and β-PbF_2, respectively) along with that of a normal ionic solid (NaCl).

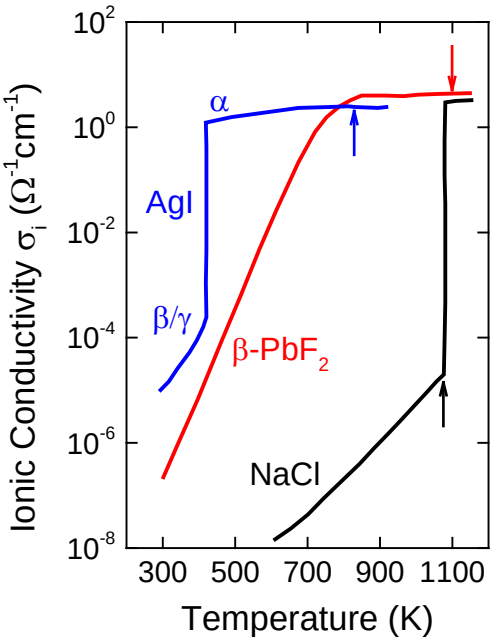

Figure 1.1 Variation of ionic conductivity with temperature for a normal ionic solid (NaCl) and two superionic conductors, AgI (Type I) and β-PbF_2 (Type II). The arrows represent the melting point of the conductors. A normal ionic solid shows nominal increase in the conductivity during the solid state and exhibits a sharp increase by few orders of magnitude during the phase change to molten state. In superionic conductors, the conductivity rises to liquid state values within the solid state. The plot is digitized from [7].

This work focusses almost exclusively on Type II superionic conductors, particularly fluorites. While there is no noticeable first order phase transformation in Type II conductors, a second order phase transition – also known as superionic or lambda (λ) transition – occurs in all Type II materials, which is manifested as a divergent specific heat at a critical temperature (T_λ) below the melting point [7]. Neutron scattering experiments on various fluorite-structured superionic

conductors reveal that the anions are highly disordered at temperatures near T_λ [8], resulting in liquid-like ionic diffusivities; Figure 1.2 shows a schematic of a fluorite crystal structure. On the other hand, the cations typically show stable lattice configuration by the virtue of higher binding energies that maintain the crystal structure up to the melting point. Thus the dominant disorder in fluorite conductors arise from the dynamically displaced anions, which include Frenkel type defects involving anion interstitials. Superionic conductors are said to be in a superionic state when one of the sub-lattices becomes highly disordered and mobile. In particular, the fluorite conductors are regarded to be in a superionic state when the anions become mobile and the ionic conductivity approaches that of a typical liquid.

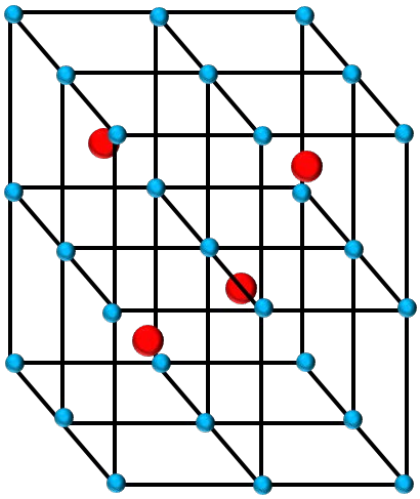

Figure 1.2 Schematic of the fluorite crystal structure with smaller and larger ions representing the anions and cations, respectively. The anions form a cubic arrangement while the cations occupy alternate cube centers.

As shown in Figure 1.2, the anions arrange themselves in a simple-cubic lattice with the cations occupying alternate cube centers (also known as the tetrahedral sites) in fluorites. The unoccupied cube centers are octahedral sites in the fluorite-structure. It is inferred from experiments that at temperatures well below T_λ, the dominant defects are anion Frenkel pairs,

with the interstitial ions mostly occupying the octahedral sites [7]. However, with an increase in the temperature, the defect concentration increases. The presence of anion vacancies at closer distances destabilizes the octahedral interstitials, resulting in a fundamental change in the nature of defects [9]. Neutron scattering studies of fluorites at temperatures approaching T_λ indicate that the anions, rather than occupying the empty cube centers, are only slightly displaced from their tetrahedral positions towards the octahedral sites, with simultaneous relaxation of the neighboring ions. These defects are dynamic in nature, hence termed as dynamic Frenkel pairs, with typical lifetimes that are $O(1)$ *ps*. Observations with coherent neutron diffuse scattering within well-defined regions of the reciprocal space give a definitive indication of the presence of dynamical correlations between the defective anions [7]; different cluster models have been proposed in the past to predict the most probable configuration of these disordered anions [10]. The study of dynamical correlations among anions in Type II superionic conductors using statistical mechanics and atomistic simulations forms an integral part of this dissertation.

1.2 Motivation and objectives of the current research

As already mentioned, fluorite superionic conductors have an underlying crystalline state by the virtue of a stable cation sub-lattice configuration. Madden and co-workers have shown that the dynamics of the disordered anions are similar to that in glassy (amorphous) or jammed states [11, 12]. For example, it has been shown that the variation of resistivity – a measure of mobility – in several Type II superionic conductors exhibits a non-Arrhenius behavior that is analogous to that of variation of viscosity – a measure of viscous transport – in supercooled liquids [13]. This correspondence can be observed from Figure 1.3, which shows the variation of resistivity for different fluorite superionics [11]. An exponential variation of viscosity

represents a simple activated process for the relaxation of shear stresses in a fluidic state, while a non-exponential variation indicates possible cooperative effects. Analogously, a non-exponential change in the resistivity in superionic conductors can result from correlated and cooperative dynamics.

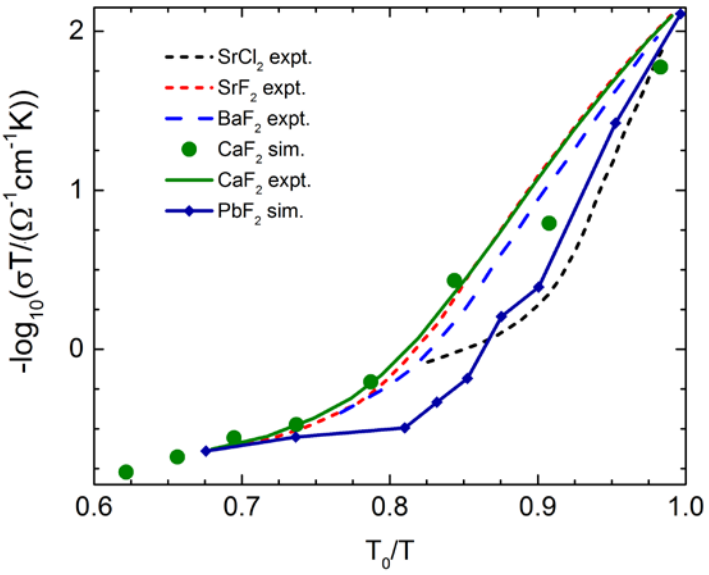

Figure 1.3 Variation of ionic resistivity, or inverse of ionic conductivity (σ), with temperature. T_0 has been chosen as the temperature at which the ionic conductivity has a value of $10^{-2.2}\ \Omega^{-1}\cdot cm^{-1}$. The behavior of the plot changes little when T_λ is chosen for T_0. The plot is digitized from [11].

Apart from similarities in transport properties, the variation of time-correlation functions also shows identical behavior. For example, the decay of time-correlation functions in supercooled liquids exhibit two-step relaxation with a non-exponential ("stretching") behavior at intermediate times [14]; an analogous behavior is also observed in superionics. Figure 1.4 shows the variation of $F_s(k,\tau)$ with time for fluorine ions in CaF_2 at different temperatures, clearly manifesting both the features.

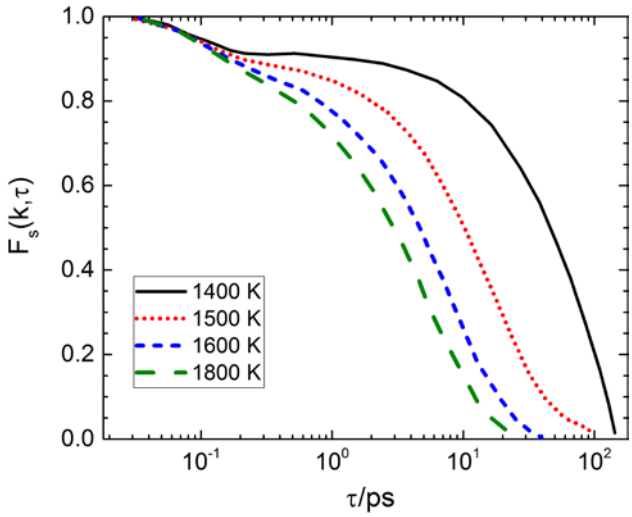

Figure 1.4 Self-intermediate scattering function, $F_s(k,\tau)$, for fluorine ions in CaF_2. The wave-vector k is chosen to be considerably smaller than the inverse lattice constant. At the lowest temperature, the two-step decay is evident with a *stretching* relaxation before falling-off at longer times. The plot is digitized from [11].

These similarities set a platform to inquire on the possible manifestation of another well-known phenomenon concerning supercooled or glassy states in superionic conductors – dynamical heterogeneity (DH) [15-18]. DH refers to the observation that atoms or molecules in a deeply supercooled state partition themselves into dynamically different states. Thus DH indicates a spatial grouping of *dynamically-alike* atoms with one group having a higher mobility than the other. The discovery of DH is considered to be one of the milestones in the study of glasses and supercooled liquids [19], and jammed systems, in general. Since nothing is known about DH in superionic conductors, a key objective of this dissertation is to probe the possible manifestation of DH in Type II superionic conductors (or superionics). A central challenge, however, for this inquiry arises from the difference in behavior of the dynamically jammed states in superionics and supercooled states. While slow relaxation is aided by decreasing entropy in the supercooled state, which eventually takes the system far away from equilibrium and towards the glass transition, any possible DH and cooperative dynamics in superionics

would necessarily have to evolve against the destabilizing entropic forces under equilibrium conditions.

Uranium dioxide (UO_2), a well-known material for nuclear fuel in light water reactors (LWRs), is a Type II superionic conductor. It is also known that UO_2 resists amorphization under intense radiation [20]. It is, therefore, natural to inquire whether the tolerance to amorphization is related to the glassy dynamics exhibited by Type II superionics. Thus another objective for the current dissertation is to investigate the dynamic response of UO_2 when subjected to radiation, and determine the dynamical conditions that are responsible for defect recovery after irradiation.

Several theories have been proposed in the past to explain the amorphization tolerance of materials under irradiation. These include the role of high ionicity, a low crystallization-to-melting temperature ratio [21], chemical bond effects, as determined from the electronic density maps that indicate the proclivity of certain atomic rearrangements to amorphize [22], and the topological freedom underlying certain crystalline materials [23]. For UO_2, the role played by the recombination of oxygen Frenkel pairs, which are the dominant defects created during irradiation [24], and the high ionicity [21] have been considered as possible pathways for amorphization resistance. The salient features of fluorites and closely-related-structures in curbing amorphization have also been studied in detail. Sickafus and co-workers have demonstrated the ability of fluorite structures to accommodate disorder and point defects by virtue of low defect formation energies, thereby avoiding lattice instability and amorphization [25]. Further, Sickafus and co-workers have also shown that compounds with natural atomic disordering tendencies or, equivalently, having low order-disorder (O-D) transformation energies, are associated with better resistance to amorphization [26]. Computer simulations have also shed light on radiation-tolerance of fluorite-structured compounds, including UO_2,

by showing the tendency of the displaced ions, following radiation, to anneal quickly. Interestingly, the activation energy of recombination is much lower than the activation energy of normal diffusive motion [27]. Remarkably, this Frenkel pair recombination also plays the decisive role in determining the amorphization resistance of pyrochlores, a close variant of the fluorites [28]. However, the defect recovery of UO_2 has never been studied from the perspective of its superionic character. In this dissertation, computer simulations are performed to study the response of UO_2 under irradiation conditions. This investigation entails non-equilibrium simulations which mimics the interaction of a neutron or ion with the crystalline medium. Thus, this dissertation encompasses equilibrium simulations of Type II superionics along with non-equilibrium simulations of UO_2 that follow the displacement cascade evolution.

1.3 Outline of this dissertation

This dissertation is mainly divided into two parts. The first part focusses on the equilibrium simulations of Type II superionic conductors with an emphasis on the character of dynamic disorder, cooperativity, and correlations. The dynamic characteristics near the λ-transition are determined using classical atomistic simulations while those at lower temperatures are evaluated using temperature accelerated dynamics (TAD), a technique that falls under the umbrella of accelerated molecular dynamics (AMD). The second part of this dissertation focuses on non-equilibrium simulations of UO_2 subjected to irradiation knocks. In the following, I will elaborate the two parts in detail.

The first part focuses on classical atomistic simulations under equilibrium conditions, where the system is not acted upon by external forces. Fluctuations play a central role in determining correlations under equilibrium conditions. Thus in Chapter 2, the main elements

of statistical mechanics is discussed. One of the aims of this study is to investigate whether an order-disorder (O-D) transition exists in Type II superionic conductors. So in Chapter 3, data from experiments and molecular simulations are employed to identify possible signatures of O-D transition in Type II superionics. For UO_2, which is the fuel in most nuclear reactors, this O-D transition or onset temperature, possibly marks the first significant deviation from its ideal crystalline behavior. For Type II conductors a few atomistic simulations at the microscopic level show that the disordered ions, at high temperatures, hop from one native site to another [29]. This hopping takes place over a time scale that is $O(1–10)$ *ps* indicating liquid-like characteristics that have been likened to those in the supercooled liquids with the superionic transition temperature (T_λ) corresponding to the glass transition temperature (T_g) [11]. One of the reasons why the glass transition is an important problem is that the basic physics associated with it such as slow cooperative relaxation, non-exponentiality, and dynamic heterogeneity is generic, and thus found in many diverse dynamical systems. Given the correspondence between the glass transition and the superionic temperatures [11]**,** it is plausible that Type II superionics can potentially exhibit generic glass-like dynamics despite the underlying crystalline structure in these systems. In particular, such a comparison elicits an intriguing but unresolved question: Do Type II superionic conductors portray dynamical heterogeneity (DH) – a definitive hallmark of supercooled and glassy states? Although the similarities between superionics and supercooled states have been brought out before, a concrete understanding of the evolution of dynamical heterogeneity is nebulous. So in Chapter 4, investigations are directed to probe the presence of DH in superionics. It is revealed, for the first time, that DH varies non-monotonically with temperature – a behavior that is very different in glassy states where DH exhibits a monotonic increase with decreasing temperatures. It is further shown in Chapter 5 that the phenomena of dynamic facilitation (DF), originally introduced to explain the microscopic mechanism of slow relaxation in supercooled systems, provides the necessary

microscopic underpinning of DH in superionics. In a dynamically facilitated system, a jammed region can become unjammed only if it is physically adjacent to a mobile region. Finally, the string-like displacements of atoms in a deeply supercooled state, the quintessential mode of atom mobility in jammed systems, is shown to operate in Type II superionics as well. Remarkably, the probability distribution of the length of the string is shown to vary exponentially, which is identical to that observed in supercooled and jammed states (Chapter 6). Thus the demonstration of DH, DF and string-like cooperative atomic displacements in superionics, in line with the dynamic characteristics of supercooled liquids, significantly augments the already existing but scant list of phenomenological similarities between these two distinct types of materials, and establishes Type II superionics as a prototypical jammed system above the O-D transition temperatures but below the superionic transition temperature.

The second part of this dissertation deals with non-equilibrium displacement cascade simulations of UO_2. As mentioned earlier, the nuclear fuel in light water reactors, which is comprised of UO_2, is subjected to different kinds of radiation such as neutrons and gamma photons that emanate primarily through the fissioning of U^{235} nuclei. These radiations change the structure and dynamics of the fuel, clad and other structural members over a timespan that ranges from nanoseconds to several years. Inside the fuel, the energetic fission products, ranging from insoluble volatile gases such as xenon and krypton, to a wide assortment of elements [30], also create numerous defects. Over time, these radiation-induced defects may aggregate, leading to undesirable properties such as swelling, hardening, and amorphization, all of which can lead to severe damage in reactor materials [31]. Amorphization refers to structural transformation from a crystalline solid phase to a solid that lacks long-range order, and is deleterious for materials operating inside a reactor [32]. During the operation of a reactor, nuclear fuel has been observed to undergo significant swelling (attributed to the

accumulation of gaseous fission products) as well as polygonization – the division of each grain into 10^4 - 10^5 sub-grains, especially at the peripheral regions subjected to high burnup [33]. Changes to the structure and porosity of the grains, along with the formation of defect clusters and dislocation loops have also been observed [34, 35]. However, UO_2 is known to resist amorphization even when subjected to intense nuclear radiations [20, 36]. So this work aims to understand the mechanism of the dynamic recovery, at the atomistic level, following radiation knocks. Thus the second major objective of this dissertation is to analyze the short-time dynamical response of UO_2 following radiation impacts, using non-equilibrium atomistic simulations (Chapter 7). Even though properties such as high ionicity and low defect formation energy in UO_2 have been emphasized in the past to account for its tolerance to amorphization, the dynamical response and mechanism of defect recovery in UO_2 following radiation is not known in much detail. Radiation is inherently dynamic (non-equilibrium), and thus it is pertinent to understand the dynamics of the displaced ions during the annealing process. One of the sub-objectives of this work is to examine whether the native behavior of oxygen ions at superionic conditions are also exhibited by the displaced ions that are created through displacement cascades in UO_2. In Chapter 7, it is shown that oxygen ions following a radiation perturbation knock exhibit correlated motion, which is similar to that in high temperature superionic state. Interestingly, the displaced oxygen ions also undergo fast recovery through collective string-like displacements. Thus the superionic characteristics of UO_2 under equilibrium conditions are also instrumental in fast defect recovery following radiation.

Chapter 2: THEORY

The key objective of this dissertation, as briefed in Chapter 1, is to uncover of the dynamical correlations in superionic conductors under equilibrium and irradiation conditions. The dynamical correlations are highly non-linear and are not tractable to theoretical approaches that result in closed form solutions. In this dissertation the collective and correlated behavior of superionics is extracted through classical atomistic or molecular dynamics (MD) simulations and analyzed through the time-tested principles of classical/quantum mechanics and statistical mechanics. This chapter elucidates the key ideas of multibody mechanics and statistical mechanics, which are relevant to this investigation.

2.1.1 Schrödinger equation and Born-Oppenheimer approximation

Investigation of atomic motion invariably begins with the Schrödinger equation. Consider a system having *N* nuclei and *n* total number of electrons. The Schrödinger equation can be written as:

$$\left[\sum_{i=1}^{n}\frac{-\hbar^2}{2m}\nabla_i^2+\sum_{i>j}\frac{e^2}{\left|\boldsymbol{r}_i-\boldsymbol{r}_j\right|}+\sum_{I=1}^{N}\frac{-\hbar^2}{2M_I}\nabla_I^2+\sum_{I>J}\frac{Z_IZ_Je^2}{\left|\boldsymbol{R}_I-\boldsymbol{R}_J\right|}-\sum_{i,I}\frac{Z_Ie^2}{\left|\boldsymbol{R}_I-\boldsymbol{r}_i\right|}\right]\Psi(\boldsymbol{r},\boldsymbol{R})=E\Psi(\boldsymbol{r},\boldsymbol{R}) \quad (2.1)$$

This is a multi-component, inseparable many-body equation that cannot be solved analytically. The expression in the brackets represents the Hamiltonian of the system; the first two terms represent kinetic energy of electrons and electron-electron potential energy, respectively, while the third and fourth terms represent kinetic energy of nuclei and inter-nuclei interaction, respectively. The last term represents the attractive electron-nuclear potential and couples the motion of electrons and nuclei. The wave function $\Psi(\boldsymbol{r},\boldsymbol{R})$ is a function of all the electron

coordinates $\boldsymbol{r} \equiv (\boldsymbol{r_1}, \boldsymbol{r_2}, \ldots, \boldsymbol{r_n})$ and nuclear coordinates $\boldsymbol{R} \equiv (\mathbf{R_1}, \boldsymbol{R_2}, \ldots, \mathbf{R_N})$. If Equation 2.1 can be solved for all the eigenfunctions $\Psi_n(\boldsymbol{r}, \boldsymbol{R})$ and corresponding eigenvalues E_n of the Hamiltonian, one would be able to obtain any property of interest. Since the analytical solution of Equation 2.1 is impossible for many body interactions, approximations have to be introduced for simplifying Equation 2.1. Except for the presence of the last term in the Hamiltonian which couples nuclear and electronic coordinates, one would be able to separate Equation 2.1 into two equations, each depending on the coordinates of either nuclei ($\boldsymbol{R}$) or electrons ($\boldsymbol{r}$). Such an approximation reduces the dimensionality and complexity dramatically, and the total solution can be simply be expressed as the product of the solutions of the two parts, i.e. $\Psi_n(\boldsymbol{r}, \boldsymbol{R}) = \psi_n(\boldsymbol{r})\varphi_n(\boldsymbol{R})$. The corresponding eigenvalue E_n is simply the sum of the two energy eigenvalues.

A similar, but not exactly identical, method of simplifying Equation 2.1 is by invoking the Born-Oppenheimer approximation, which takes advantage of the vast disparate timescales between the motion of electrons and the nuclei, owing to the enormous difference in their masses [37]. The characteristic frequencies of typical atomic vibration (~10^{13} s^{-1}) and electronic motion (~10^{15} s^{-1}) also reflect this disparity. The nuclei, heavier by three to four orders of magnitude relative to that of an electron, will appear to be fixed in space by the electrons. Thus, the electrons will rearrange 'instantaneously' to any change in the nuclear positions and the nuclei will experience only a time-averaged electronic potential. This reasoning lead Born and Oppenheimer to suggest solving for electronic eigenstates initially for a given configuration of nuclei ($\boldsymbol{R}$), and then using the resulting energies into the second equation for nuclei for solving for nuclei eigenstates. The electron eigenvalue equation is given by:

$$\left[\sum_{i=1}^{n}\frac{-\hbar^2}{2m}\nabla_i^2+\sum_{i>j}\frac{e^2}{\left|\boldsymbol{r}_i-\boldsymbol{r}_j\right|}-\sum_{i,I}\frac{Z_I e^2}{\left|\boldsymbol{R}_I-\boldsymbol{r}_i\right|}\right]\psi_n(\boldsymbol{r},\boldsymbol{R})=\varepsilon_n(\boldsymbol{R})\psi_n(\boldsymbol{r},\boldsymbol{R}) \tag{2.2}$$

The electron eigenstates $\psi_n(\boldsymbol{r},\boldsymbol{R})$ and energies $\varepsilon_n(\boldsymbol{R})$ parametrically depend only on $\boldsymbol{R}$ with no dependence on the gradients acting on the coordinates of nuclei. For a given nuclear coordinate $\boldsymbol{R}$, there will be a set of energy levels, labeled as ground-state electron energy $\varepsilon_0(\boldsymbol{R})$ and excited energy levels $\varepsilon_1(\boldsymbol{R})$, $\varepsilon_2(\boldsymbol{R})$ etc. The nuclear coordinate $\boldsymbol{R}$ can be varied continuously over the *N*-dimensional space and at each point, a set of electronic energy levels can be ascertained. All the eigenvalues $\varepsilon_i(\boldsymbol{R})$ obtained over the *N*-dimensional space gives rise to an energy surface known as the Born-Oppenheimer surface or potential energy surface (PES). The nuclei, which were assumed frozen during the electron eigenvalue calculation, now move in the potential created by the other nuclei as well as the electronic PES; the ground-state PES is usually the one of interest. The PES can provide information on several properties: For example, the equilibrium structure can be found from the minima of this surface, and the energetic barriers to kinetic processes such as diffusion can be obtained from the minima and saddle points of the potential energy surface. The equation for the nuclei eigenstates is given by:

$$\left[\sum_{I=1}^{N}\frac{-\hbar^2}{2M_I}\nabla_I^2+\sum_{I>J}\frac{Z_I Z_J e^2}{\left|\boldsymbol{R}_I-\boldsymbol{R}_J\right|}+\varepsilon_i(\boldsymbol{R})\right]\varphi_n(\boldsymbol{R})=E\varphi_n(\boldsymbol{R}) \tag{2.3}$$

For each electronic surface, the nuclear eigenvalue equation now results in a set of energy levels. These are the rotational and vibrational energies of nuclear motion.

2.1.2 *Ab-initio* molecular dynamics (AIMD)

The nuclei, owing to their large mass (*again*!), can be treated by means of classical laws without any appreciable error. This is especially true for heavier nuclei and also for temperatures significantly higher than 0 *K*. This forms the basis of *ab-initio* molecular dynamics where Equation 2.2 is first solved for the electronic eigenstates and the forces on the nuclei determined using the Hellmann-Feynman theorem. In an iterative strategy, the positions of the nuclei can be advanced in accordance to the classical Newton's laws of motion using the forces derived from the electronic structure, and the whole process can be repeated by solving the electronic eigenvalue equation corresponding to the new $\boldsymbol{R}$. The numerical scheme of evolving a system of *N* nuclei in time by evaluating Born-Oppenheimer PES *on the fly* is known as *ab-initio molecular dynamics* (*AIMD*). One of the problems associated with *ab-initio* MD is that the electronic PES has to be evaluated with good convergence; otherwise, the atomistic dynamics often fail to conserve energy leading to the PES acting either as a heat sink or a source, gradually draining or adding energy to the system. A variant of the *ab-initio* MD method that is more stable has been devised by Car and Parrinello [38]. Unfortunately, all *ab-initio* MD methods are computationally expensive and are usually limited to studies involving atoms on the order of hundreds, and for a time period of a few picoseconds.

2.1.3 Classical molecular dynamics (MD)

A completely different, but more efficient, method of simulating atomic motion is by using a *parametrized* form of Born-Oppenheimer surface and obtaining the inter-nuclear forces from the nuclear positions. This technique is referred to as *empirical* or *classical* MD method and can be understood by inspecting the nuclei eigenvalue equation (Equation 2.3). For a given configuration of nuclei, $\boldsymbol{R}$, the second term in the brackets is just a constant, and hence, the

total potential energy, which is the sum of the second and third terms, can be expressed as $U(\boldsymbol{R})$, the interatomic potential, that determines the motion of nuclei. The basis of empirical MD simulations is that this $U(\boldsymbol{R})$ can now be approximated by a function, thereby circumventing the problem of solving the electron eigenvalue problem for $\varepsilon_i(\boldsymbol{R})$ in Equation 2.3, for a given configuration of the nuclei. In this way, the electronic degrees of freedom are completely integrated out and all electronic effects are incorporated in the interatomic potential $U(\boldsymbol{R})$. Now, rather than solving the Schrödinger equation, Newton's *classical* laws of motion can be applied for determining the positions and momenta of the atoms. This approximation works except for the lightest of the atoms. The key advantage, however, lies is the ability to deal with millions of atoms over time scales as long as nanoseconds or even up to microseconds. In this work, the dynamics of the superionic state is evaluated solely based on the empirical MD approach.

The only input to the empirical MD method is the interatomic potential energy or potential for short; $U(\boldsymbol{r}_1,\boldsymbol{r}_2,...,\boldsymbol{r}_N)$ describes the potential energy of the system as a function of the coordinates of the atoms. From Newtonian mechanics, the force acting on the i^{th} atom can be evaluated as $\boldsymbol{F}_i = -\nabla_{r_i} U$. The potential, in general, can be expanded as a many-body expression given by:

$$U(\boldsymbol{r}_1,\boldsymbol{r}_2,...,\boldsymbol{r}_N) = \sum_i U_1(r_i) + \sum_i \sum_{j>i} U_2(\boldsymbol{r}_i,\boldsymbol{r}_j) + \sum_i \sum_{j>i} \sum_{k>j} U_3(\boldsymbol{r}_i,\boldsymbol{r}_j,\boldsymbol{r}_k) + .. \qquad (2.4)$$

Here, U_1 is a one-body term that can arise from an external field, and U_2 is a two-body potential that defines the interaction between any pair of atoms in the system; it is solely a function of the distance between the atoms $r = |\boldsymbol{r}_i - \boldsymbol{r}_j|$, and independent of the presence of other atoms. U_3 is a three-body potential that arise when the interaction of a pair of atoms is

modified by the presence of a third atom. As discussed subsequently, two body potentials are most appropriate for predicting the structural and dynamical properties of Type II superionics. Thus, in this dissertation, the potentials are limited to those with two-body interactions. For systems interacting through pair potentials, the force on i^{th} atom can be simplified as: $\boldsymbol{F}_i = \sum_{j \neq i} \boldsymbol{f}_{ij}$ where $\boldsymbol{f}_{ij}$ represents the force acting on i^{th} atom from the interaction with the j^{th} atom.

Thus, the force on each atom can be expressed as the sum of the forces from all other atoms in the system. This force accelerates the atom in accordance to the Newton's II law: $\boldsymbol{F}_i = m\boldsymbol{a}_i = m\frac{d^2 x_i}{dt^2}$. In the MD method, this differential equation is solved numerically to update the position and momentum of each atom. Since Newton's II law of motion is of the second order, it necessitates specifying two initial conditions. In general, the position and velocity of all the atoms in the system are specified at the start of the simulation, $t = 0$, and the system is advanced one time-step per iteration.

2.1.4 Interatomic potentials

Two superionic materials UO_2 and CaF_2 are prominently investigated in this study. UO_2 is modeled by a potential of the form given by:

$$V_{\alpha\beta}\left(r_{\alpha\beta}\right) = z_\alpha z_\beta / r_{\alpha\beta} + A_{\alpha\beta} e^{\left(-r_{\alpha\beta}/\rho_{\alpha\beta}\right)} - C_{\alpha\beta}/r_{\alpha\beta}^6 + D_{\alpha\beta}\left[e^{-2B_{\alpha\beta}\left(r_{\alpha\beta}-r_{\alpha\beta}^*\right)} - 2e^{-B_{\alpha\beta}\left(r_{\alpha\beta}-r_{\alpha\beta}^*\right)}\right] \quad (2.5)$$

Here, the indices α and β label the ionic species, r denotes distance between the ions, and z is the charge. The first term in Equation 2.5 represents the well-known Coulombic interaction between the charged ions, while the second and third terms represent the repulsive interaction due to overlap of the electron clouds and the attractive van der Waals interaction, respectively. The last term represents the Morse term to describe the energy of covalent bonding, attributed

only to anion-cation interactions. To account for the partial charge transfer between the ions, each ion has a fractional (non-formal) effective charge, which is the product of its 'formal' charge and an ionicity parameter. The parameters are taken from Yakub *et al.* [39], and are listed in Table 2.1.

Table 2.1 Parameters for the Yakub *et al.* potential.

z_+ (e)	z_- (e)	A_{++} (eV)	A_{--} (eV)	A_{+-} (eV)	ρ(Å)	C_{--}(eV·Å^6)	D_{++} (eV)	B_{+-} (Å^{-1})	r^*_{+-} (Å)
2.2208	-1.1104	187.03	883.12	432.18	0.3422	3.996	0.5055	1.864	2.378

Here, $\rho = \rho_{++} = \rho_{--} = \rho_{+-}$ and, also, $C_{++} = C_{+-} = 0$ and $D_{--} = D_{+-} = 0$.

Another set of parameters has been suggested by Basak *et al*. for UO_2 [40]. These parameters are listed in Table 2.2.

Table 2.2 Parameters for the Basak *et al.* potential.

z_+ (e)	z_- (e)	A_{++} (eV)	A_{--} (eV)	A_{+-} (eV)	ρ(Å)	C_{--}(eV·Å^6)	D_{++} (eV)	B_{+-} (Å^{-1})	r^*_{+-} (Å)
2.40	-1.20	294.75	1633.66	693.92	0.327022	3.950	0.5774	1.65	2.369

Here, $\rho = \rho_{++} = \rho_{--} = \rho_{+-}$ and, also, $C_{++} = C_{+-} = 0$ and $D_{--} = D_{+-} = 0$.

CaF_2 is modeled by a potential of the form:

$$V_{\alpha\beta}\left(r_{\alpha\beta}\right) = z_\alpha z_\beta / r_{\alpha\beta} + A_{\alpha\beta} e^{\left(-r_{\alpha\beta}/\rho_{\alpha\beta}\right)} - C_{\alpha\beta}/r_{\alpha\beta}^6 \qquad (2.6)$$

Equation 2.6 does not contain the Morse term and the parameters for CaF_2 are adopted from Gillan [41]; these are listed in Table 2.3. It may be noted that $C_{++} = C_{+-} = 0$.

Table 2.3 Values of various parameters for Gillan potential.

z_+ (e)	z_- (e)	A_{++} (eV)	A_{--} (eV)	A_{+-} (eV)	ρ_{++}(Å)	ρ_{--}(Å)	ρ_{+-}(Å)	C_{--}(eV·Å^6)
2.0	-1.0	0.0	1808	674.3	0.0	0.293	0.336	109.1

2.1.5 Interatomic potentials for cascade simulations

The potentials discussed in the previous section describe the interatomic interactions quite accurately at normal separation of the atoms. However, in non-equilibrium displacement cascade simulations, atoms approach very close to each other (within 1 Å), and the potentials described previously fail to accurately describe the forces of interaction. For short interionic distances, the well-known Ziegler-Biersack-Littmark (ZBL) potential accurately describes the ionic interactions through the screened Coulombic forces between the nuclei [42]. The ZBL potential belongs to the class of a pair potential and is expressed as [42]:

$$V_{\alpha\beta}^{ZBL}\left(r_{\alpha\beta}\right)=\frac{1}{4\pi\varepsilon_0}\frac{z_1 z_2 e^2}{r_{\alpha\beta}}\phi\left(r_{\alpha\beta}/a\right) \tag{2.7}$$

The ZBL potential has two terms – the first one is the Coulomb repulsive term, with z_1 and z_2 denoting the number of protons in each nuclei, while the second part is the universal screening function, where *a* is the function of Bohr radius a_0 which is cast in the form:

$$a=\frac{0.8854\times a_0}{z_1^{0.23}+z_2^{0.23}} \tag{2.8}$$

The screening function $\phi(x)$ is expressed as [42]:

$$\phi(x)=0.1818e^{-3.2x}+0.5099e^{-0.9423x}+0.2802e^{-0.4029x}+0.02817e^{-0.2016x} \tag{2.9}$$

For displacement cascade simulations, the ZBL potential is stitched with the equilibrium pair potentials described earlier such that there is a smooth transitioning without any discontinuity in force [43]. We have applied a Fermi-like function f_F, as formulated below, for a smooth interpolation. With the Fermi function defined as,

$$f_F\left(r_{\alpha\beta}\right)=\frac{1}{1+e^{-A_F\left(r_{\alpha\beta}-r_c\right)}} \tag{2.10}$$

the combined pairwise potential is expressed as:

$$V_{\alpha\beta}\left(r_{\alpha\beta}\right)=f_F\left(r_{\alpha\beta}\right)V_{\alpha\beta}^{Eq}+\left(1-f_F\left(r_{\alpha\beta}\right)\right)V_{\alpha\beta}^{ZBL}. \tag{2.11}$$

In the above equation, $V_{\alpha\beta}^{Eq}$ is the equilibrium pair-potential and $V_{\alpha\beta}^{ZBL}$ is the ZBL potential. Equation 2.11 is the form of the potential that is applied in this work for radiation-damage simulations of UO_2 (Chapter 7). The values for the constants A_F and r_c are chosen as 14 $Å^{-1}$ and 1 Å, respectively; these values have been determined by verifying the suitability of the potential to predict the correct equilibrium properties after being perturbed by a small radiation knock perturbation. Note that z(U) = 92 and z(O) = 8 and the interacting ion-pair in Equation 2.7 can be any of the three possible pairs: U-U, O-O and U-O.

2.2 Statistical mechanics

Atomistic methods described in the previous section enables the prediction of the atomic displacements, momenta and forces of each atom or ion at any instant of time. Thus microscopic details of the system can be predicted with sufficient accuracy. Statistical mechanics connects these microscopic details with macroscopic properties and response [44-46]. Properties can be evaluated using equilibrium statistical mechanics, while the response of a system that deviates from equilibrium can be analyzed using non-equilibrium statistical mechanics. An ensemble or an assembly of systems is a central concept in statistical mechanics – these copies are defined such that they have statistically equivalent macroscopic properties such as temperature, pressure or chemical potential, but with very different dynamical trajectories in phase-space. A macroscopic property *P*, typically, an experimental observable,

is simply an average over all ensemble copies. Ensembles typically have a correspondence to thermodynamic systems. Most dynamical and structural correlations in this dissertation are averaged in ensembles with constant number of atoms (*N*), constant pressure (*P*), and constant temperature (*T*) – *NPT*, or with *NVT*, where *V* denotes the constant volume of the system. These ensembles are analogous to experimental systems, the results of which are used to validate the atomistic simulation results.

2.2.1 Phase space

The dynamic evolution of a microscopic system is described by the concept of *phase space*. In the following, the concept of phase space is formalized followed by a discussion on the ergodic hypothesis, which connects time averages from atomistic simulations to ensemble averages.

The microscopic state of a particle at any time *t* is described by specifying its instantaneous position and momentum $(\mathbf{r},\mathbf{p})$ with a total of 6 coordinates. Correspondingly, the microscopic state of an *N*-particle system is specified by 6*N* coordinates. Phase space denotes a 6*N* dimensional mathematical space in which there is an axis for every position and momentum coordinate; thus a microscopic state of the system is described by a *point* in the phase space. The evolution of the coordinates **r** and **p** in time *t* is given by the Hamiltonian equations of motion, defined as [45]:

$$\begin{aligned}\dot{\mathbf{r}}_i &= \frac{\partial H(\mathbf{r},\mathbf{p})}{\partial \mathbf{p}_i} \\ \dot{\mathbf{p}}_i &= -\frac{\partial H(\mathbf{r},\mathbf{p})}{\partial \mathbf{r}_i}\end{aligned} \tag{2.12}$$

Here $H(\mathbf{r},\mathbf{p})$ is the Hamiltonian of the system. The set of coordinates $(\mathbf{r},\mathbf{p})$ evolves with time as shown in Equation 2.12, and accordingly, a representative point carves out a trajectory in

the phase space. If the total energy of the system is a constant, say E, then the phase space trajectory will be restricted to the hypersurface, $H(\mathbf{r},\mathbf{p}) = E$, of constant energy.

Under equilibrium, a system evolves with no external force acting on it. As mentioned previously, the concept of ensemble averaging is used [46] to calculate macroscopic properties. An ensemble, first introduced by Gibbs, is a collection or replicas of imaginary systems having statistically equivalent macroscopic properties but each with a *distinct* microstate. This definition is in line with the observation that a given macrostate corresponds to many microstates [47]. The ensemble is represented by a set of distinct points in the 6N-dimensional phase space. The value of any equilibrium property of the system – for example, the system pressure – can be obtained as the average value of this property over all members of the ensemble – this is known as ensemble averaging.

2.2.2 Ergodic hypothesis

Time dependent atomistic simulations give positions and velocities of all particles (atoms, ions etc.) at every instant of time. Constructing an ensemble average is an arduous task because the number of microstates corresponding to any given macroscopic state is extremely large [46]. The ergodic hypothesis, originally developed by Boltzmann and Maxwell, can be applied here to make progress: It states that the value of a property obtained as an *ensemble average* over all replicas of the original system is equal to the *time average* of the property over a trajectory of the original system in the phase space. This equivalence is central to time dependent atomistic simulations, and it allows to interpret the simulation results in a statistically meaningful way. If a system is able to explore all parts of the phase space, it is known as an *ergodic system* while on the other hand, non-ergodic systems have parts of the phase space that are inaccessible. Technically, atomistic simulations can never explore all accessible regions of

the phase space within reasonable computational times. However, it can explore a subset of the accessible regions that are statistically identical or that are representative, if the system do not deviate far away from equilibrium.

2.3 Temperature accelerated dynamics (TAD)

One of the major limitations of classical atomistic or MD simulations is that it is limited to time scales of nano- or microseconds; this limitation is not inherent from the theory but stems from the limited computational resources. Further, the integration of equations of motion is sequential in nature, and hence, parallelization does not circumvents the problem. Several atomistic methods have been developed in the past to extend the time-scales of atomistic simulations by several orders of magnitude. These include a set of accelerated molecular dynamics (AMD) methods developed by Arthur Voter [48, 49] that are applicable to systems that are characterized by rare events such as diffusion of defects in a solid state. Thus for most times, a system remains in a small phase space volume that correspond to the vibration of atoms, which is occasionally punctuated by a transition to another small region in the phase space. These small phase space volumes correspond to local minima in the potential energy surface (PES), and this state-to-state dynamics is well-described by the transition state theory (TST). All AMD methods attempt to accelerate the state-to-state transitions within reasonable computational times. There are three AMD methods which are most useful: temperature accelerated dynamics (TAD) [50], hyperdynamics [51, 52], and parallel replica method [53]. While each method accomplishes long-time simulations in characteristic ways, TST [54, 55] provides the theoretical foundation for all methods.

In this work, TAD is applied for studying the dynamics of superionics at low temperatures relative to the superionic transition temperature. TAD accelerates the dynamics

of *activated* processes in solid state, and it works by raising the temperature of the system and identifying those events that should occur at the initial temperature [48, 50]. TAD relies on the harmonic TST approximation, which is valid for many solid-state diffusive processes and relatively easy to implement within the framework of atomistic simulations.

In TAD [50], the system temperature is raised from the desired temperature (T_{low}) to a higher temperature (T_{high}) to accelerate the escape rate from each potential energy basin. Although raising the temperature is a well-known and often-used approach for accelerating diffusive events, it does not give the correct state-to-state evolution for temperature T_{low} as the relative escape probabilities change with temperature. However, if, from among the transitions occurring rapidly at T_{high}, the correct T_{low} transitions can be selected and the others prevented, then the system will evolve from state to state appropriately for temperature T_{low} [50]. The key to TAD (or, any AMD method) is in recognizing that the right sequence of state-to-state transitions can be predicted correctly as long as the relative probability of finding each of the possible escape paths is preserved [50]. A main premise in TAD is the applicability of harmonic transition state theory (HTST), which gives an expression for the rate-constant of an event i as [50]:

$$k_i = \nu_i e^{-E_i/(k_B T)} \tag{2.13}$$

where E_i is the energy difference between the basin minimum and the saddle point, ν_i is a temperature-independent pre-exponential factor that depends on the vibrational spectrum at the minimum and the saddle point, and k_B is the Boltzmann constant. Hence, the temperature dependence of the transition rates follows the Arrhenius relation. In TAD, one performs a basin constrained MD where the trajectory of the system is confined to a particular potential energy basin at T_{high} [50]. Whenever the system tries to escape to a new potential basin with the

execution of an event, the waiting time for each new transition pathway is recorded and the saddle point for the transition is determined using the nudged elastic band (NEB) method [56]; thereafter the system is reflected back to the original state (basin) and the process repeated. In this way, the basin constrained MD generates a list of escape paths and attempted escape times $t_{i,\text{high}}$ for different events i at the temperature T_{high}. Now, the goal is to determine the waiting time $t_{i,\text{low}}$ at the original temperature from the observed $t_{i,\text{high}}$. To obtain this, the assumption that any infrequent event system obeys first-order kinetics is used, which is described as [50]:

$$p_i(t)dt = k_i e^{-k_i t} dt \tag{2.14}$$

where k_i is the rate constant for escape. Now, consider a process, i, at two different temperatures, T_{low} and T_{high} ($T_{\text{low}} \leq T_{\text{high}}$), with corresponding rate constants, $k_{i,\text{low}}$ and $k_{i,\text{high}}$. Since the waiting times $t_{i,\text{low}}$ and $t_{i,\text{high}}$ at the two temperatures are exponentially distributed, it follows that the products $k_{i,\text{low}}t_{i,\text{low}}$ and $k_{i,\text{high}}t_{i,\text{high}}$ have identical distributions. Hence it can be shown that $k_{i,\text{low}}t_{i,\text{low}} = k_{i,\text{high}}t_{i,\text{high}}$. Combining this equality with Equation 2.13, the following can be derived.

$$t_{i,\text{low}} = t_{i,\text{high}} e^{E_i\left(\beta_{\text{low}} - \beta_{\text{high}}\right)} \tag{2.15}$$

Equation 2.15 gives the waiting time $t_{i,\text{low}}$, having determined $t_{i,\text{high}}$ earlier. Also note that the energy barrier E_i is also calculated, using the NEB method, after each event is detected. As a consequence, a set of event times generated in a high-temperature simulation can be mapped to a set of much longer wait times in the low-temperature system. However, because this mapping involves the energy barrier of the transition event (E_i), which is different for each event, the first event at the high temperature may not be the earliest event at the low

temperature. Equation 2.15 is shown graphically in Figure 2.1 which is an Arrhenius-style plot (ln(1/*t*) versus 1/*T*), with time progressing downwards; note 1/*t* is the inverse of the waiting or escape time.

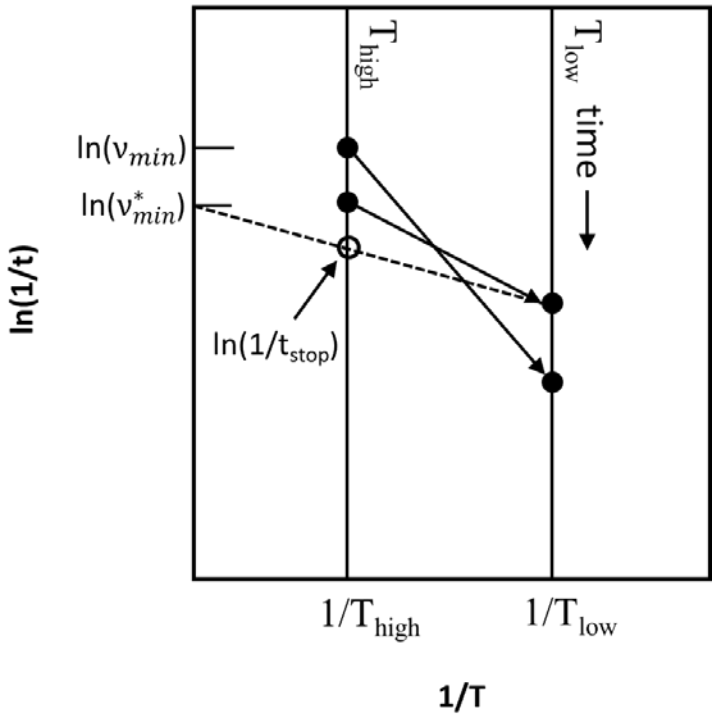

Figure 2.1 Pictorial representation of the TAD method [50].

The straight line with an arrow represents an extrapolation of $t_{i,\text{high}}$ to $t_{i,\text{low}}$.This can be better understood by reformulating Equation 2.15 as:

$$t_{i,\text{low}} = t_{i,\text{high}} e^{E_i\left(\beta_{\text{low}} - \beta_{\text{high}}\right)}$$

$$\Rightarrow \frac{t_{i,\text{high}}}{t_{i,\text{low}}} = \frac{\left(1/t_{i,\text{low}}\right)}{\left(1/t_{i,\text{high}}\right)} = e^{-E_i\left(\beta_{\text{low}} - \beta_{\text{high}}\right)}$$

$$\therefore \ \ln\left(1/t_{i,\text{low}}\right) - \ln\left(1/t_{i,\text{high}}\right) = -E_i\left(\beta_{\text{low}} - \beta_{\text{high}}\right) \tag{2.16}$$

Equation 2.16 thus shows that the slope of a line in Figure 2.1 is equal to $-\beta E_i$, where E_i is the energy barrier for the event. It is important to realize that the extrapolation lines may cross, so that the order of the escape times differs at the two temperatures. It is therefore essential to continue the MD simulation at T_{high} until one can be confident that the shortest waiting time at T_{low} has been found. TAD simulations are stopped using a characteristic minimum frequency of the system. Similar to MD simulations, TAD also requires the specification of the interatomic or interionic potential of the system.

2.4 Structural correlation functions

In this section, some of the commonly used structural metrics that are applied in this dissertation are discussed. These metrics are evaluated as time averages from atomistic simulations.

2.4.1. Radial distribution function, *g*(*r*)

The radial distribution function RDF or $g(r)$ gives information on the structure of the system by expressing, on average, the spatial distribution of atoms. The density field at a point $\boldsymbol{r}$ and time t can be expressed as [57]:

$$\rho(\mathbf{r},t) = \sum_i \delta(\mathbf{r} - \mathbf{r}_i(t)) \tag{2.17}$$

The sum is over all the atoms in the system and Equation 2.17 defines the local number density in terms of the average occupancy of a small volume of space at **r**, estimated at time *t*. Note that the delta function in Equation 2.17 has the units of reciprocal volume. The probability density of finding $N(N\text{-}1)$ pairs of particles in an N-particle system is given by**:**

$$\rho_N^2\left(\mathbf{r},\mathbf{r}'\right)=\left\langle\sum_{i=1}^{N}\sum_{i\neq j}^{N}\delta\left(\mathbf{r}-\mathbf{r}_i\right)\delta\left(\mathbf{r}'-\mathbf{r}_j\right)\right\rangle \tag{2.18}$$

For homogeneous isotropic systems, this probability depends only on the relative separation between the particles. Thus

$$g_N^2\left(\mathbf{r}_1,\mathbf{r}_2\right)=g\left(|\,\mathbf{r}_1-\mathbf{r}_2\,|\right)\equiv g\left(\mathbf{r}\right)=\frac{\rho_N^2\left(|\,\mathbf{r}_1-\mathbf{r}_2\,|\right)}{\rho^2} \tag{2.19}$$

Thus $\rho g(\mathbf{r})$ gives the conditional probability of finding a particle at distance $\mathbf{r}$ from the origin given that there is a particle at origin. The above expression can be simplified as

$$g\left(\mathbf{r}\right)=\frac{1}{N\rho}\sum_{i=1}^{N}\sum_{k\neq i}^{N}\left\langle\delta\left(\mathbf{r}-\left(\mathbf{r}_i-\mathbf{r}_k\right)\right)\right\rangle \tag{2.20}$$

Typically, RDF is defined as a pair correlation function which assumes spherical symmetry. Thus pair correlation is expressed as

$$g\left(r\right)=\frac{1}{4\pi r^2}\frac{1}{N\rho}\sum_{i=1}^{N}\sum_{k\neq i}^{N}\left\langle\delta\left(\mathbf{r}-|\mathbf{r}_i-\mathbf{r}_k|\right)\right\rangle \tag{2.21}$$

Both radial distribution and pair correlation are interchangeably used in this dissertation. Note that RDF is now expressed as an ensemble average, which according to the ergodic hypothesis is simply an average of time. Thus in atomistic simulations, RDF is calculated as a time average of several configurations of the system at different times.

Crystalline, liquid and gaseous states have very different atomic arrangements and these states can be uniquely identified through $g(r)$. In a crystal, the RDF shows repeating peaks that indicates the presence of long-ranged order. Liquids generally have short-range order and this is reflected by few prominent peaks in the RDF. As observed in Figure 2.2 the RDF peaks for the liquids state flatten out to a value of 1 at large distances from origin; by definition, $g(r)=1$ implies that the density at this location is same as the macroscopic density.

For gases at high pressure, the RDF typically shows only a single peak that corresponds to the nearest neighbor.

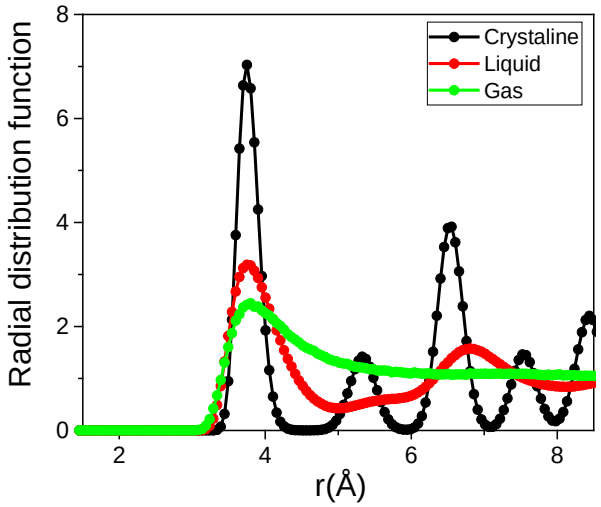

Figure 2.2 Typical RDF variation in solid, liquid and gaseous states.

RDF is often used to determine the coordination number of a structure. The equation relating them is derived here. Let N be the total number of atoms in the system and $n(r)dr$ is the number of atoms in a shell between r and $r+dr$ such that $\int_0^\infty n(r)dr = N$. The volume of the shell between r and $r+dr$ can be evaluated to be

$$\frac{4}{3}\pi\left(r+dr\right)^3 - \frac{4}{3}\pi r^3 \approx 4\pi r^2 dr. \tag{2.22}$$

Now, the definition of $g(r)$ is given by

$$g(r) = \frac{\left(\dfrac{n(r)dr}{4\pi r^2 dr}\right)}{\rho} \tag{2.23}$$

The coordination number (β) can be written in terms of $n(r)dr$ as $\int_0^{r_c} n(r)dr = \beta,$ where r_c is the nearest neighbor distance (or the position corresponding to first peak in the RDF). Since

the atoms are in constant thermal motion, r_c is usually taken as the position corresponding to first minimum in RDF. Finally,

$$\beta = \int_0^{r_c} g(r)\rho 4\pi r^2 dr \;\Rightarrow \beta = 4\pi\rho \int_0^{r_c} g(r) r^2 dr \tag{2.24}$$

Equation 2.24 gives the desired relation between β and $g(r)$.

2.5 Dynamical correlation functions

The dynamical correlation functions to be discussed are generally space-time correlation functions that can be obtained from the trajectory of an MD simulation; some of these are also accessible from experiments such as neutron and x-ray scattering. Correlation functions generally span the full range of length and time scales, from slow long-wavelength modes describing the continuum in the hydrodynamic limit, right down to the atomic level [58]. Several space-time correlation functions are used in this dissertation to characterize the superionic dynamics and these are elucidated in this Section.

2.5.1 van Hove self-correlation function, $G_s(r,t)$

The van Hove self-correlation function, $G_s(r,t)$, is a spatio-temporal quantity that describes the correlation of the same (or *self*) atom at different times. It is given by the expression [57]:

$$G_s(r,t) \equiv \left\langle \frac{1}{N} \sum_{i=1}^{N} \delta\left(r - \left|\mathbf{r}_i(t) - \mathbf{r}_i(0)\right|\right) \right\rangle \tag{2.25}$$

Thus $G_s(r,t)$ indicates the probability of finding an atom in a small volume element $d\mathbf{r}$, centered at r, and time t, when the *same* atom is at the origin at time t = 0; Figure 2.3 shows this pictorially.

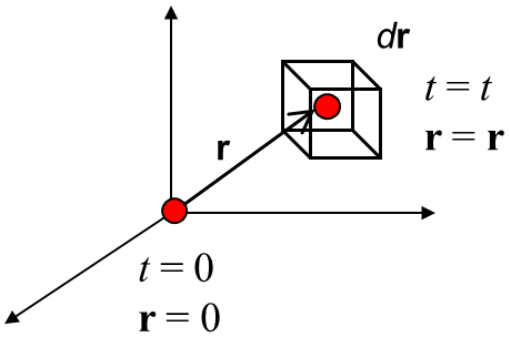

Figure 2.3 For an atom at the origin at time $t = 0$, $G_s(r,t)$ indicates the probability of finding this atom in a volume element $d\mathbf{r}$, centered at $\mathbf{r}$, and time t.

For any given time t,

$$\int G_s(r,t)dr = 1 \tag{2.26}$$

when integrated over all space, and, at $t = 0$, $G_s(r,0) = \delta(r)$. The position of an atom at both long times and large distances becomes uncorrelated to its original position and thus becomes equally probable to be found anywhere in the system. From the normalization shown in Equation 2.26, we can see the value of G_s as collapsing from δ function (at $t = 0$) to zero at larger r. During the period of collapse, the shape of $G_s(r,t)$ is approximately Gaussian, except at the initial times [59].

2.5.2 Density correlator

The density field shown in Equation 2.17 can be transformed to Fourier space as:

$$\begin{aligned}\rho_{\mathbf{k}}(t) &= \int \rho(\mathbf{r},t)e^{-i\mathbf{k}.\mathbf{r}}d\mathbf{r} \\ &= \sum_i e^{-i\mathbf{k}.\mathbf{r}_i(t)}\end{aligned} \tag{2.27}$$

The density-correlator $F(\mathbf{k},t)$, also known as the intermediate scattering function, is defined as the correlation of the density function in Fourier space, and is expressed as

$$F(\mathbf{k},t) = \frac{1}{N}\left\langle \rho_{-\mathbf{k}}(0)\rho_{\mathbf{k}}(t)\right\rangle = \frac{1}{N}\sum_{ij}\left\langle e^{-i\mathbf{k}.\mathbf{r}_i(0)}e^{i\mathbf{k}.\mathbf{r}_j(t)}\right\rangle \tag{2.28}$$

It may be noted that $\sum_i \mathbf{k}_i = 0$ because **k** takes both positive and negative values to conserve momentum. $F(\mathbf{k},t)$ measures the fluctuation of the density on a length scale ~$2\pi/k$ where $k = |\mathbf{k}|$. When k is large, the density correlator is probing very short length scales [60] and when k is small – the smallest value is fixed by the simulation volume – the continuum scales are probed. The self-intermediate scattering function is the self-part of the density auto-correlator and is given by

$$F_s(\mathbf{k},t) = \left\langle e^{i\mathbf{k}.(\mathbf{r}_i(t)-\mathbf{r}_i(0))}\right\rangle \tag{2.29}$$

$F_s(\mathbf{k},t)$ should be statistically similar for each particle in the system by virtue of ensemble averaging in Equation 2.29. At time t = 0, $F_s(\mathbf{k},t)$ is unity and as time evolves, F_s exhibits a smooth decay indicating the lack of correlation at long times. The decay rate is higher for higher k, indicating that shorter-wavelength fluctuations die out more rapidly [61]. In slowly evolving systems such as in supercooled liquids, $F_s(\mathbf{k},t)$ shows a pronounced caging period where particles are trapped in a cage formed by the neighbors.

2.5.3 Dynamic structure function

The dynamic structure function is the time Fourier transform of the density correlator. It is given by [58]:

$$S(\mathbf{k},\omega) = \frac{1}{2\pi}\int_{-\infty}^{\infty} F(\mathbf{k},t)\exp(i\omega t)\,dt \tag{2.30}$$

The dynamic structure factor, when integrated over all angular frequencies, give rise to the static structure factor, $S(\mathbf{k})$, defined as

$$S(\mathbf{k}) = \int_{-\infty}^{\infty} S(\mathbf{k},\omega)\, d\omega = F(\mathbf{k},0) \tag{2.31}$$

The static structure function $S(\mathbf{k})$, which reduces to the initial value of the density correlation function, can be directly measured by neutron or x-ray scattering/diffraction experiments. And finally, $S(\mathbf{k})$ is related to the radial distribution function through the equation [62]:

$$S(\mathbf{k}) = 1 + \rho \int_V \left[g(\mathbf{r}) - 1 \right] e^{i\mathbf{k}.\mathbf{r}}\, d\mathbf{r} \tag{2.32}$$

Thus experimental observables such as structure function, dynamic structure function, and density correlator (intermediate scattering function) can be directly compared to results from atomistic simulations.

2.5.4 Four-point susceptibility function, $\chi_4(t)$

For characterizing the spatially heterogeneous dynamics in slowly evolving systems such as supercooled liquids, several multipoint correlation functions have been devised in the past. In particular, a four-point susceptibility function (χ_4) has served as a metric to characterize the growing length scales with decreasing temperature in supercooling of liquids. For a system containing N atoms and a chosen wave-vector $\mathbf{k}$, $\chi_4(t)$ is given by the expression [63]:

$$\chi_4(t) = N\left[\left\langle \left(\frac{1}{N} \sum_i \cos \mathbf{k}.\left[\mathbf{r}_i(t) - \mathbf{r}_i(0) \right] \right)^2 \right\rangle - \left\langle \frac{1}{N} \sum_i \cos \mathbf{k}.\left[\mathbf{r}_i(t) - \mathbf{r}_i(0) \right] \right\rangle^2 \right] \tag{2.33}$$

In supercooled liquids, $\chi_4(t)$ typically grows in time before decreasing at longer times. This non-monotonic variation is attributed to the transient nature of the dynamic heterogeneity [64]. Toninelli *et al.* [63] have characterized some universal features of $\chi_4(t)$ in glassy systems: At short time scales when atoms exhibits ballistic motion, $\chi_4(t)$ increases in time as t^4. This is followed by an elastic regime characterized by a t or $t^{1/2}$ growth depending on whether phonons

are propagative or diffusive, culminating with χ_4 showing a maximum at a time that is $O(\tau_\alpha)$, where τ_α is the alpha relaxation time. This maximum is followed by a fast decay to zero at long times. In Chapter 4, $\chi_4(t)$ is applied to characterize the spatial heterogeneous dynamics of the disordered ions in superionic conductors.

2.5.5 Spatial correlation of dynamic propensity, $C_d(r,t)$

The propensity of an atom is defined as the square of the displacement of the atom, averaged over all several copies of iso-configurational ensemble [65]. The correlation in propensity of atoms in the system, known as the spatial correlation of the propensity – $C_d(r,t)$ [66], is used as an alternative metric to characterize the heterogeneous dynamics in superionic conductors. $C_d(r,t)$ for a system of N atoms is defined as:

$$C_d(r,t) = \frac{\left\langle \delta w(i,t)\delta w(j,t) \right\rangle}{\left\langle \left[\delta w(t)\right]^2 \right\rangle} \tag{2.34}$$

In the above equation, i and j are two atoms such that the magnitude of the distance between them falls within an interval of Δr, centered at r. $w(i,t)$ is the propensity $\left\langle r^2 \right\rangle_{ic}$ of i^{th} ion at time t with $\delta w(i,t) \equiv w(i,t) - \left\langle w(t) \right\rangle$ denoting the instantaneous fluctuation in the propensity of i^{th} ion. The correlation in the propensity fluctuation is then normalized to $\left\langle [\delta w(t)]^2 \right\rangle = \frac{1}{N}\sum_{i=1}^{N}[\delta w(i,t)]^2$.

Analysis by Razul *et al*. [66] shows that C_d is a reliable metric for studying the heterogenous dynamics in supercooled systems. Studies on Kob-Andersen binary Lennard-Jones supercooled liquid shows that C_d depicts a peak amplitude, which (*i*) manifests at times that scale with τ_α, and (*ii*) increases monotonically with decreasing temperature. In Chapter 4, the equivalence of χ_4 and C_d is shown in characterizing the spatially heterogeneous dynamics for

supercooled states. It is further shown that χ_4 is not appropriate for superionic states because it fails to distinguish a crystalline structure from a deeply supercooled states. On the other hand, C_d has the ability to distinguish supercooled-like states that is morphing from a crystalline structure – key strength that is indispensable in the study of correlated dynamics in superionic conductors.

Chapter 3: ORDER-DISORDER TRANSITION IN TYPE II SUPERIONIC CONDUCTORS

3.1 Introduction

Neutron scattering experiments reveal that the disordered anions form a significant fraction of the total as the superionic transition is approached from lower temperatures. Thus it is tempting to inquire whether a crossover temperature or an onset of superionicity, or simply an order-disorder (O-D) transition exists, where the dynamic disorder is first manifested in Type II conductors. Unlike the superionic transition temperature T_λ, the concept of a superionic onset temperature, which is defined as T_α in this work, is not well-formed even though, as shown later, experimental evidences do attest to such a transition. In this chapter, existing experimental data is analyzed to identify possible signatures of T_α for various fluorite superionics. Molecular dynamics (MD) simulations of UO_2 and CaF_2 are also performed to identify such as transition.

3.2 Evidence of order-disorder (O-D) transition in Type II superionics from experiments

In Figure 3.1, we provide experimental confirmation (from reported data) on a crossover temperature (T_α) that marks the onset of disorder, which is distinctly different from T_λ – the superionic transition temperature. The figure portrays neutron scattering/diffraction data which includes both integrated coherent diffuse scattering per anion (X^D), and the fraction of disordered anions (n_d) that is deduced by assuming a particular defective model, for different

fluorite-type ionic conductors. Neutron scattering and diffraction measurements give information on ions that leave the native lattice sites, and hence, they provide quantitative estimates on the disorder of the system. It is compelling to observe that there is a definitive onset of disorder, which is particularly evident from a very recent investigation on $SrCl_2$, as well as for PbF_2 and UO_2. For UO_2, the two neutron scattering data sets in Figure 3.1 indicate that T_α^* is $\approx 2000\ K$, approximately [67] which is distinct from the superionic temperature of $T_\lambda \approx 2610\ K$ [7]. For $SrCl_2$, CaF_2 and PbF_2, the disorder onset temperatures are 920 *K*, 1180 *K*, and 570 *K*, respectively; these onset temperatures are different from known T_λ values ($SrCl_2$: 1001 *K*, CaF_2: 1430 *K*, PbF_2: 711 *K* [7]).

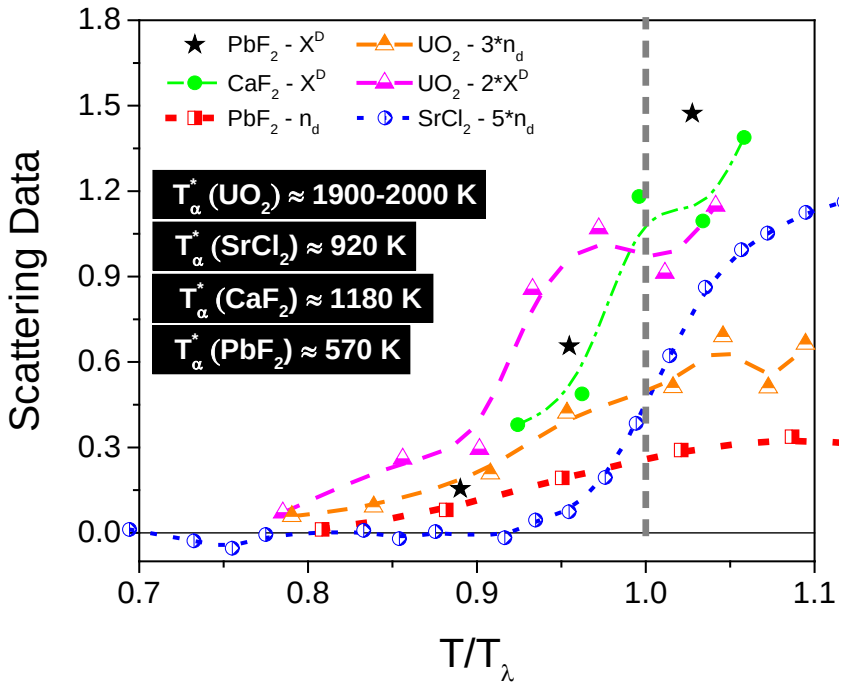

Figure 3.1 Neutron scattering and diffraction data for several (Type II) superionic conductors [10, 67-69] belonging to the fluorite–family. The superscript (*) denotes inferred values from experimental data and dashed/dotted lines serve to guide the eye. The change of slope in properties are checked by derivative analysis; however, the inferred numerical values are approximate.

Figure 3.2 depicts the experimental data on specific heat of UO_2 (closed symbols) [70], which shows a prominent peak at the superionic transition temperature ($T_\lambda \approx 2610\ K$) – a feature which is shared by all Type II superionic conductors. The semi–open symbols show the close agreement between the predictions from MD simulations [29] using the Yakub inter–ionic potential [71], and the experimental data [70]. It is illuminating to note that there is an approximate correspondence between the variation in thermo-physical properties, and the disorder onset temperature (T_α). In Figure 3.2, it can be noted that the specific heat shows a slope change at ~1950 *K*, which is close to the disorder onset temperature (~2000 *K*). The variation of lattice parameter with temperature [72, 73] (see inset) also shows a visible change in slope near 1950 *K*.

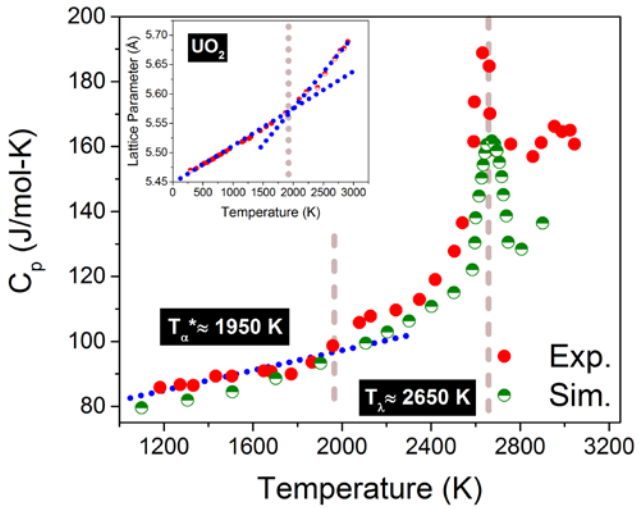

Figure 3.2 Specific heat of UO_2 (simulations are performed using MD [29] with Yakub potential [71]). (Inset) Lattice parameter as a function of temperature [72, 73].

The correlation of neutron scattering/diffraction data to the changes in ionic conductivity behavior is portrayed in Figure 3.3. The recent neutron diffraction data by Hull *et. al.* [68] on $SrCl_2$ shows an onset of disorder at 920 *K* while the ionic conductivity data [74], shown in

Figure 3.3(*a*), also depicts a change in slope at the same temperature (920 *K*). It is interesting to note that ionic conductivity portrays another slope change at 1025 *K* which is close to the experimental value of T_λ = 1001 *K* (from specific heat measurements) [10]. Another slope change can be detected at a lower temperature of ~800 *K*; the origin, however, is unknown. Thus the slopes in the ionic conductivity data alludes to possible transitions in superionic conductors.

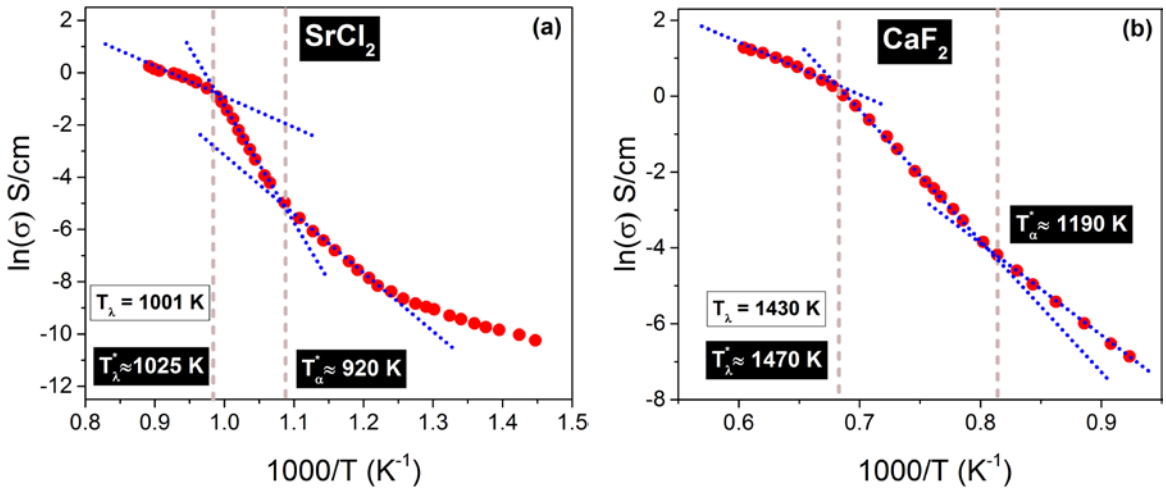

Figure 3.3 Ionic conductivities of (*a*) $SrCl_2$ and (*b*) CaF_2, respectively [74].

The conductivity data on CaF_2 [74] in Figure 3.3(*b*), which is similar to that in Figure 3.3(*a*) for $SrCl_2$, again helps in identifying two crossover temperatures, although the slope changes are more subtle. The disorder onset temperature of $T_\alpha^* \approx 1180$ *K*, estimated from a linear extrapolation of the neutron scattering data [10] in Figure 3.1, is close to a temperature of 1190 *K*, which is identified from the slope change in the conductivity data [74]. A second slope change at a temperature of 1470 *K* is also observed, which is close to T_λ = 1430 *K* [10]. Detailed conductivity data spanning both transition temperatures do not appear to be reported for PbF_2

and UO_2. Thus experimental data on neutron scattering and ionic conductivity data strongly attest to an O-D transition or a superionic onset temperature T_α.

Brillouin scattering technique can be indirectly employed to determine the elastic constants. Starting from low temperatures, the scattering frequencies/elastic constants generally decrease linearly with increasing temperature, and the linearity is broken typically near the temperature that corresponds to the onset of disorder (T_α). Figure 3.4 shows a comparison of the disorder onset temperature identified from neutron scattering (~1180 *K*) and the temperature at which linearity in Brillouin frequencies is broken (~1180 *K*) for CaF_2. In the next section, MD simulations are employed to study the order-disorder transition in two superionic conductors, UO_2 and CaF_2.

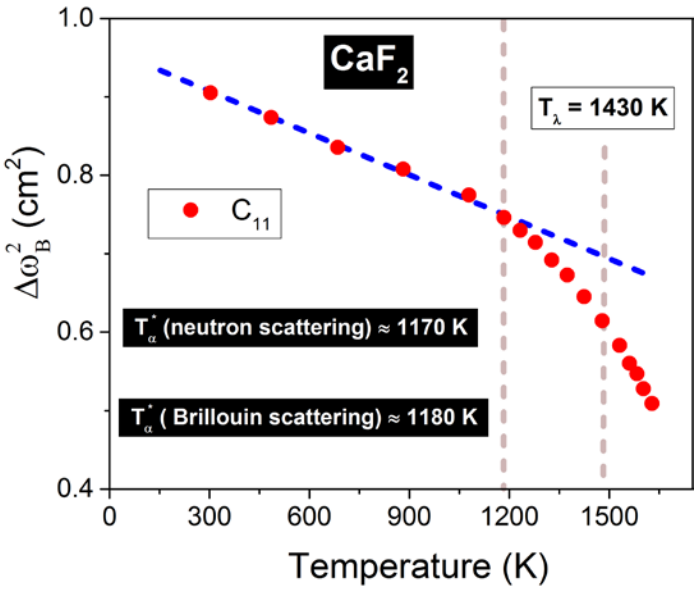

Figure 3.4 Brillouin scattering data for CaF_2 [75] showing the variation of the elasticity constant C_{11}. The temperature corresponding to the change in slope T_α correlates well with the data from neutron scattering experiments.

3.3 Evidence for order-disorder (O-D) transition from atomistic simulations

Two superionic conductors – UO_2 and CaF_2, are investigated using atomistic (MD) simulations for unveiling possible signatures that attest to an order-disorder transition. Owing to its importance as the most widely used nuclear fuel, a number of empirical potentials have been developed to model UO_2 and many of these have been compared in recent works involving equilibrium and non-equilibrium simulations [76-79]. In the current work, the short-range interactions are described using the Busing-Ida type potential form [80], with the parameters adopted from Yakub *et al.* [39, 71]. This rigid-ion potential has been benchmarked to a spectrum of properties [29, 71, 81] with reasonable accuracy. The form of the potential is given in Equation 2.5, while the parameters are listed in Table 2.1. For CaF_2, the ion interactions are modeled using Equation 2.6, with the parameters listed in Table 2.3. Simulations are performed with 2596-6144 ions with periodic boundary conditions along all the three directions. The long-ranged electrostatic interactions are evaluated by using Wolf method [82], which has been benchmarked to the standard Ewald sum method. In the Wolf method, both the Coulombic energies and forces are truncated at a fixed cutoff radius (10.2 Å in the current work) with charge compensation on the surface of the truncation sphere; the damping parameter is chosen as 0.3. The Newton's equations of motion are integrated using the leapfrog algorithm [58], with a time-step of 1 *fs*. The system is initially equilibrated for 200 *ps* in a *NPT* ensemble (at zero pressure); the simulations are then allowed to proceed in a *NVE* ensemble for evaluating the equilibrium static and dynamic properties.

3.3.1 Determination of T_λ from atomistic (MD) simulations

The interionic potentials are first validated by reproducing the characteristic superionic transition temperature T_λ using simulations and comparing to known experimental values. In Figure 3.5, the variation of specific heat at constant pressure, evaluated as the temperature derivative of total energy at zero pressure, is depicted as a function of temperature.

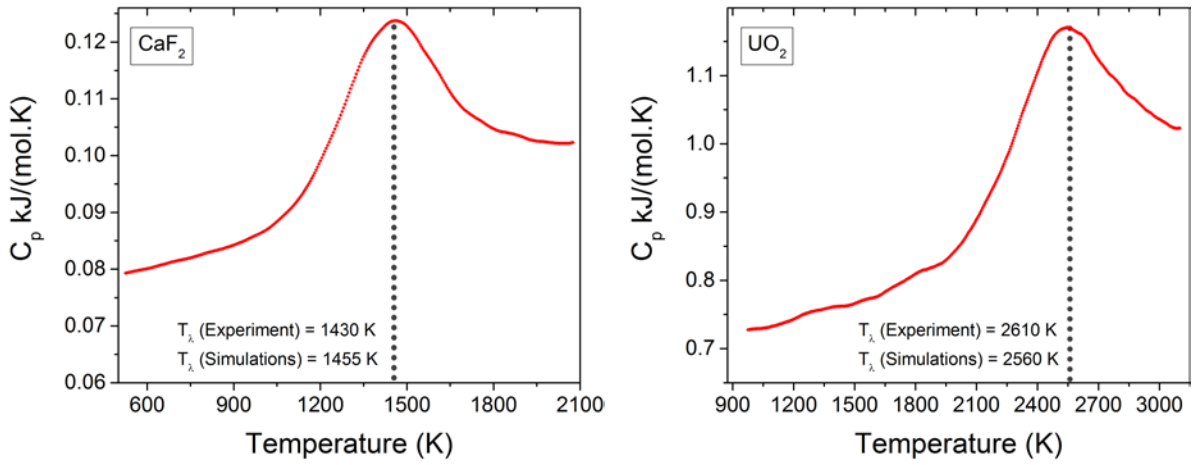

Figure 3.5 Variation of specific heat (C_p) with temperature for CaF_2 and UO_2, obtained from atomistic simulations.

The temperature corresponding to the peak in C_p represents the superionic transition temperature and the agreement with the experimentally measured T_λ is excellent for CaF_2 and UO_2. The error in both the cases is less than 2%. In the next sub-sections, structural metrics are introduced to identify T_α from atomistic simulations followed by dynamic metrics that further corroborate the O-D transition at T_α.

3.3.2 Structural evidence for T_α from atomistic simulations

For UO_2, at a temperature of 1900/2000 *K*, the onset of disorder is detected through discernible changes in the static properties such as the lattice parameter and Wendt-Abraham ratio (R^{WA}).

Figure 3.6 shows the variation of lattice parameter with temperature for UO_2. There is a clear change in slope, at ~2000 *K*, indicating the advent of disorder in the system.

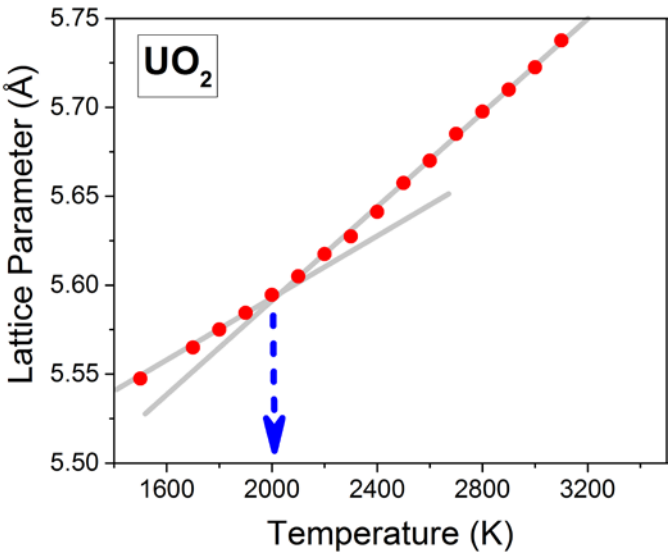

Figure 3.6 Temperature variation of lattice parameter in UO_2, obtained from MD simulations. The temperature corresponding to the change in slopes matches very well with the order-disorder temperature for UO_2 obtained from experiments (Figure 3.1).

Wendt-Abraham ratio (R^{WA}) is defined as the ratio of the first non-zero minimum in the anion–cation radial distribution function (g_{min}) to the first peak value (g_{max}), and it is a measure of the local packing, which is useful to probe fine structural changes; the Wendt-Abraham ratio is depicted for UO_2 and CaF_2 in Figure 3.7. Wendt and Abraham [83] originally had proposed this ratio to detect liquid–glassy/amorphous transition by monitoring the change of slope in R^{WA} for different thermodynamic states. The abscissa in Figure 3.7 is the normalized temperature with respect to T_α obtained from experiments [T_α (UO_2) = 1900 *K* and T_α (CaF_2) = 1180 *K*]. Below experimental T_α, R^{WA} is practically zero for both CaF_2 and UO_2, indicating a well-ordered crystalline structure with negligible probability of finding a neighboring ion between the lattice sites. Close to experimental T_α, R^{WA} becomes non-zero signaling an onset

of the disordered state; at higher temperatures, R^{WA} increases rapidly indicating enhanced disorder in the system. From Figure 3.7, it can be seen that MD simulations clearly identify an order-disorder temperature that is in excellent agreement with the experimental data.

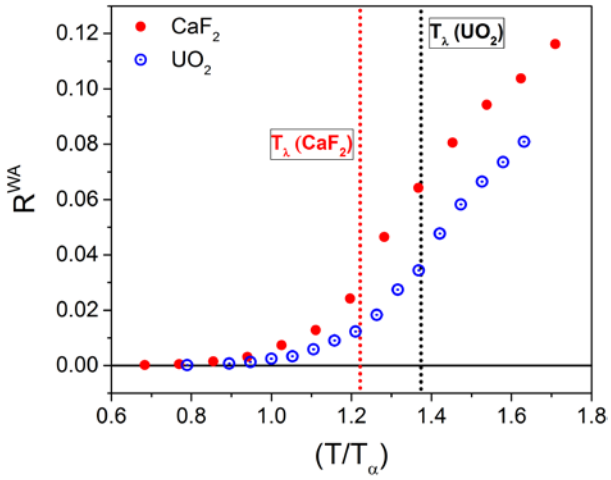

Figure 3.7 Wendt-Abraham ratio for CaF_2 and UO_2 showing the order-disorder transition for both the superionic conductors at T_α.

3.3.3 Dynamical evidence for T_α from atomistic simulations

In this section, a dynamical metric, namely, the mean square displacement (MSD) of the disordered ions, is analyzed to identify T_α in UO_2. Figure 3.8 shows the MSD of both uranium and oxygen ions in UO_2 over a wide range of temperatures, below the melting point. The uranium ions do not show any diffusive motion even at higher temperatures, as expected. However, for oxygen ions, an order-disorder transition is observed through the sub-diffusive dynamics that can be identified from the mean square displacements at a temperature of ~1900 *K*. This can clearly be confirmed from the inset of Figure 3.8(*b*), which shows the first signs of diffusive motion in the oxygen sub-lattice at ~1900 *K*. Thus both static and dynamic metrics from atomistic simulations establish an order-disorder transition temperature T_α, which is in excellent agreement with the experimental data.

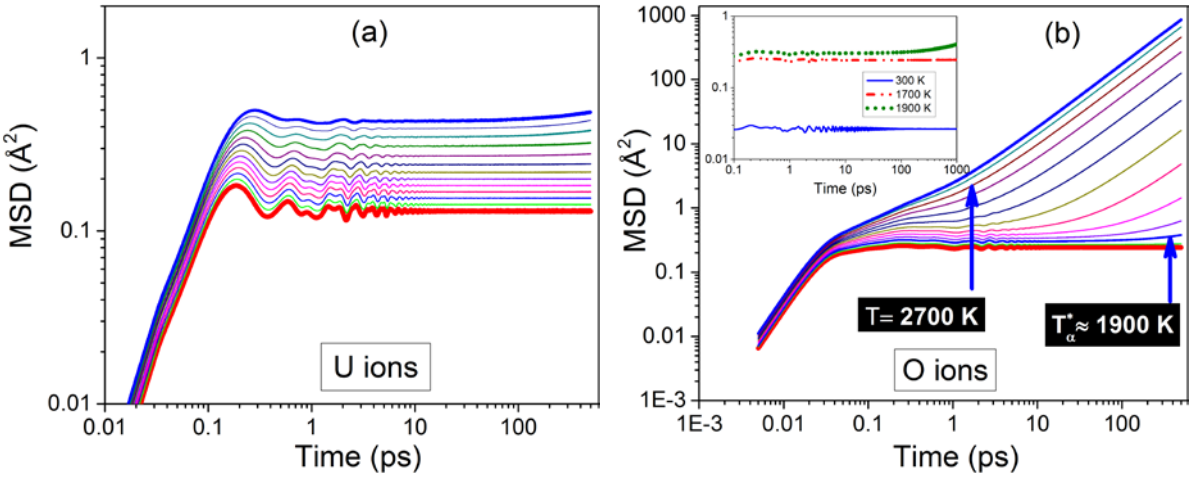

Figure 3.8 (*a*) Mean square displacement (MSD) of the U ions at various temperatures. (*b*) MSD of the O ions at different temperatures. The temperature increases from 1700 *K* (thick red) to 2900 *K* (thick blue), in steps of 100 *K*, in both the plots. (Inset) MSD of a smaller system (768 ions) with a longer time window of 1 *ns*. Note that all the states are completely in equilibrium – the flat plateau region in MSD at low temperatures indicates trapped dynamics, however, in a crystalline state. A significant change in the slope of MSD for the O ions is detected at ~1900/2000 *K*, which is corroborated by changes in properties such as lattice parameter and C_p, and evidence from scattering experiments that show anion mobility at ~2000 *K* [see Figure 3.1 and Figure 3.2].

3.3.4 Summary of transition temperatures in Type II superionic conductors

In Table 3.1, the order-disorder (O-D) transition temperature T_α [84], superionic-transition temperature T_λ [7], and melting temperature T_m [7] for various Type II superionic conductors discussed in this chapter are listed.

Table 3.1 Summary of different transition temperatures associated with various fluorite-structured superionics.

Conductor	T_α (*K*)	T_λ (*K*)	T_m (*K*)
UO_2	1900	2610	3120
CaF_2	1170	1430	1633
PbF_2	570	711	1158
$SrCl_2$	920	1001	1146

After the advent of disorder on the anion sub-lattice in fluorites at T_α, it is interesting to understand the role of interstitial sites in accommodating disorder. As discussed in Chapter 1, fluorites have vacant octahedral sites which are the main interstitial sites for displaced anions and cations. In the following section, the role of octahedrals in containing the disorder at temperatures above T_α is studied, by means of MD simulations.

3.4 Disorder in fluorite-structured Type II superionic conductors

Disorder in a solid state can either be classified as strongly structural such as long-lived defects, or strongly dynamic, which changes with time [85]. In this section, the nature of disorder in superionics is elucidated with evidence garnered from atomistic simulations. Type II conductors of interest in this study have a fluorite structure, which is shown in Figure 3.9(*a*). In these materials, the cations, which are relatively immobile species, arrange themselves in a face-centered-cubic (FCC) lattice arrangement. The anions arrange themselves in a simple-cubic lattice with the cations occupying alternate cube centers (also known as the tetrahedral sites) in fluorites. The octahedral sites remain vacant and these are the main interstitial positions for the displaced ions. The cations maintain their positions until melting, while the anions show significant disorder, both structural and dynamic. As shown subsequently, the anions have low energy thresholds for getting thermally displaced from the native sites, which results in mobile anions to hop from one tetrahedral site to another. The high value of ionic conductivity in Type II superionics, therefore, is currently attributed to the extensive lattice disorder on one of the sub-lattices at high temperatures, as well as to the ability to accommodate interstitial sites, especially at the empty octahedral sites, at low temperatures with both features providing copious conduction pathways for the charged carriers. The availability of empty octahedrals, which is numerically greater than the number of anions, thus provides a key structural pathway for fast ion diffusion.

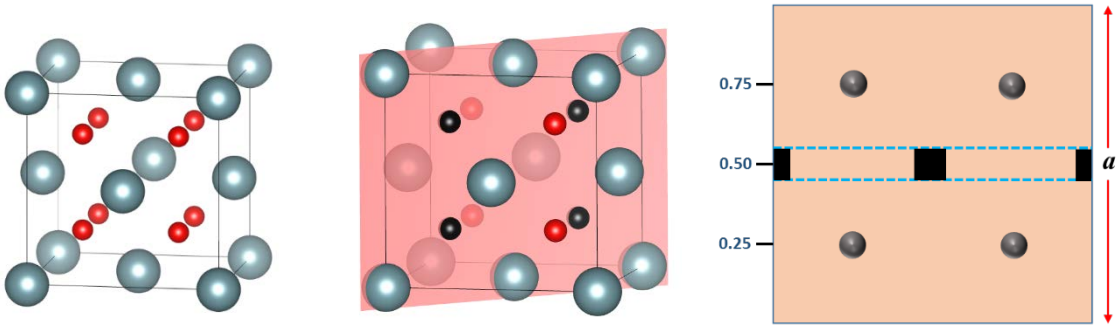

Figure 3.9 (*a*) The crystal structure of UO_2, with bigger ions representing uranium and smaller ions depicting oxygen. (*b*) The (110) plane of this unit cell has 4 oxygen ions, shown in black, and contains octahedral sites at mid-point of the plane as well as at the center of left and right edges. (*c*) The fluorite unit cell is partitioned into 51 equal-sized cells along each of the *x*, *y* and *z* directions, and every oxygen ion is consigned to one of the 51^3 cubes. For quantifying the significance of octahedral sites in accommodating displaced ions, the manifestation of disorder around them (areas shown in black) is compared to the total disorder in the region enclosed between dotted lines. "*a*" indicates the lattice constant of the fluorite unit-cell.

Neutron scattering studies performed on a variety of fluorites are analyzed through models that propose most probable sites for the disordered anions. These studies indicate that at temperatures well below T_λ, the displaced anions mostly occupy the octahedral interstitial sites and can be treated as Frenkel pairs (FPs). As temperature approaches T_λ the disorder increases and the interstitial ions on the octahedral sites become unstable due to the presence of vacancies at closer distances [9, 10]. This disorder is then referred to as *dynamic* FPs in view of its very short lifetime, which is of the order of ~1 *ps*. Hence, the disorder changes from stable FPs that portray a strong structural identity below T_α to dynamic FPs above T_α, where ions typically hop from one lattice site to another without forming permanent defects; the latter disorder exhibits a strong dynamic identity. This change is reflected in the diminishing role of octahedral interstitials in accommodating disorder; at lower temperatures (below T_α), the disorder is mostly contained in the octahedral sites by virtue of stable FPs whereas, at higher

temperatures (above T_α), displaced ions have a short lifetime at any displaced position thereby rendering the octahedral sites a relatively minor role for accommodating disorder. In other words, at higher temperatures, the probability of finding a displaced anion at the octahedral sites diminishes above the order-disorder transition temperature T_α.

Computer simulations can also attest to this change in the nature of disorder, and here, it is illustrated for two superionic conductors – UO_2 and CaF_2. The importance of octahedral sites in accommodating disorder can be quantified by assessing the presence of disordered ions at these sites with respect to neighboring sites [refer, Figure 3.9(*c*), for the case of UO_2 with oxygen being the mobile ion]. The fluorite unit cell is partitioned into 51 equal-sized cells along each of the *x*, *y* and *z* directions, and each oxygen ion in the system, depending on its position, is assigned to one of the 51^3 (=132,561) volume elements. Contours representing the population of the volume elements can now be drawn for any plane in the unit cell. Since each volume element is simply associated with only a scalar (number of ions), the directions in the volume elements do not play any role. Thus the contour dimensions (height and width) associated with both, for example, (100) and (110) planes are identical. Figure 3.9(*b*) depicts a (110) plane in fluorite structure containing octahedrals at mid-point of the plane as well as at the center of left and right edges, and Figure 3.9(*c*) shows the methodology that is applied in estimating the role of octahedral sites in accommodating disorder. For the octahedral at the middle of the plane, a square of length equal to 10% of the unit cell (~0.5 Å) centered on the octahedral site is constructed. If an ion occupies this square, it is considered to belong to the octahedral site. Similarly, octahedral sites exist at the mid-point of the side edges of the (110) plane and each of these is assigned an area that is half of the area assigned for the mid-of-the-plane octahedral. Finally, to estimate the relative importance of octahedral sites in accommodating disorder, the presence of displaced ions in between the dotted lines shown in Figure 3.9(*c*) is measured and estimate the contribution to this disorder from the octahedral

sites. The dotted lines are chosen sufficiently far from all oxygen ions and bound only the displaced ions.

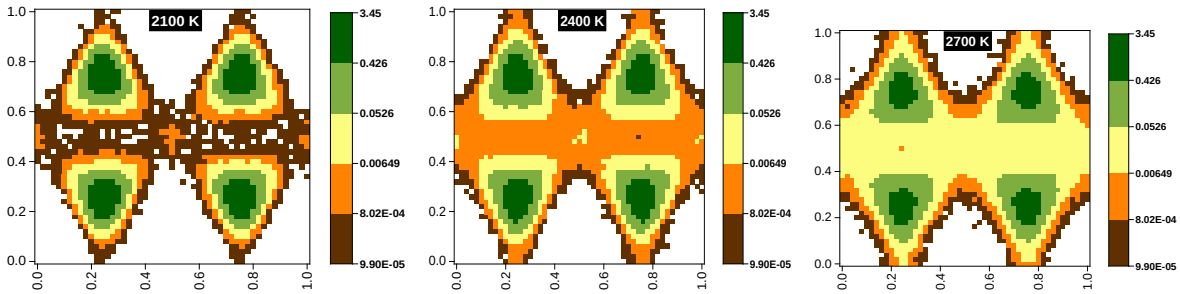

Figure 3.10 Probability contours of finding oxygen ions on the (1 1 0) plane at different temperatures for UO_2. The contours are obtained from the volume elements on the plane shown in Figure 3.9(*b*).

Figure 3.10 shows the probability contours of the distribution of oxygen ions in UO_2 along the (110) plane at different temperatures from MD simulations. The increase in disorder at higher temperatures is clearly evident. For perfectly homogeneous distribution of disorder in the area enclosed between the dotted lines shown in Figure 3.9(*c*), the contribution of disorder from octahedral sites (R_{ideal}) would be 20%. However, a higher contribution from octahedrals is expected as the large empty volume surrounding them would appeal to the thermally-displaced anions. Figure 3.11 depicts the temperature variation of R, the fraction of octahedral disorder to total disorder between the dotted lines, for both UO_2 and CaF_2. The temperature in the abscissa is normalized to the experimentally known T_λ. At temperatures close to T_α, the value of R is much higher than R_{ideal}, indicating the proclivity of displaced ions to settle at the octahedral sites. However, as temperature increases towards T_λ, the value of R decreases and the distribution of disorder becomes more and more homogeneous, in agreement with the experiments. Further, models based on scattering experiments have identified unique sites as probable locations for the disordered ions at temperatures close to T_λ [7]. However, the MD

simulation results do not give any indication for preferred positions other than the octahedral sites.

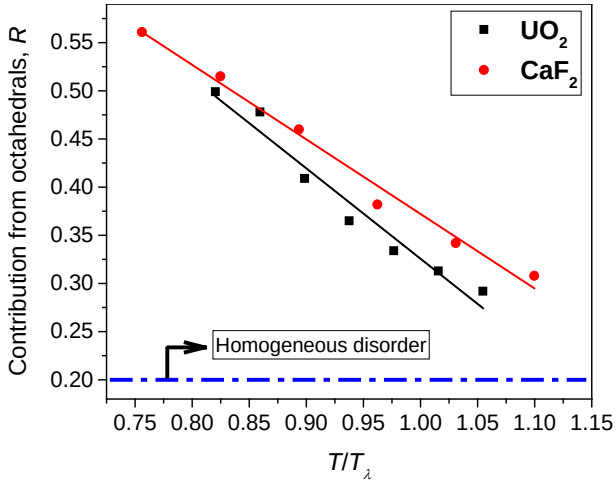

Figure 3.11 Temperature dependence of the role of octahedrals in accommodating disorder, as seen from simulations. The lower values at temperatures close to T_λ indicate the dynamical nature of disorder in superionics.

3.5 Conclusions

In this chapter, experimental evidence is provided that strongly indicates an order-disorder transition in Type II superionic conductors at a characteristic temperature T_α, marking a crossover from a crystalline state to a partially disordered state. Both neutron scattering data and conductivity measurements showed excellent agreement with each other in evaluating the order-disorder (O-D) transition. The O-D transitions are also observed from MD simulations in UO_2 and CaF_2, using both static and dynamic metrics. Further, the nature of disorder is investigated over a range of temperatures. Experiments and atomistic simulations show the presence of displaced anions mostly at octahedrals at temperatures lower than T_α. At temperatures above T_α, the displayed anions mostly hop from one native site to another without attaching any special status to the octahedral sites. In the next chapter, the correlated dynamics of the thermally active anions is brought forth through atomistic simulations.

Chapter 4: DYNAMICAL HETEROGENEITY IN THE SUPERIONIC STATE

4.1 Introduction

In Chapter 1, several phenomenological similarities between superionic conductors and supercooled states have been discussed. Despite the underlying crystalline state, the dynamics of the disordered ions in Type II superionic conductors approaching the superionic transition at T_λ has been shown to resemble that of supercooled liquids approaching the glass transition [11]. Ngai *et al.* [86] have contrasted the dynamic properties of ionically conducting glasses and crystals, and showed that they are analogous to those of glass-formers. Particularly interesting was their result on the trend of the scaled spectra of differing glass-formers and ionic conductors that have the same terminal relaxation time [87]. All these similitudes between superionics and supercooled systems elicit an intriguing but unresolved question: Do Type II superionic conductors portray dynamical heterogeneity (DH) – a definitive hallmark of supercooled and glassy states [15-18]? DH has been observed experimentally in virtually all systems that undergo glass transition [19], and becomes more pronounced with decreasing temperature towards the glass transition temperature T_g. In this chapter, the concept of DH is introduced. Subsequently, the metrics defined in Chapter 2 are used to quantify the evolution of DH in the superionic state.

4.2 Dynamical heterogeneity (DH)

Dynamical heterogeneity or spatially heterogeneous dynamics refers to the spatio-temporal correlations that partition a slowly evolving system into dynamically similar spatial subgroups.

The dynamically similar spatial groups from a molecular dynamics simulation of a two-dimensional supercooled mixture are shown schematically in Figure 4.1; the atoms are colored based on their displacements over a certain time-interval [88]. The blue colored atoms designate those that have negligible displacements while the most mobile atoms, which are displaced by at least a particle diameter, are represented as dark-red. Both the mobile and immobile particles are clearly clustered which reveal the spatially heterogeneous dynamics in an otherwise structurally homogeneous system. The spatial correlations among the dynamically evolving atoms is indicated as DH. In supercooled liquids, DH becomes more pronounced as T_g is approached from higher temperatures. Interestingly, DH is manifested by systems that are jammed or dynamically constrained.

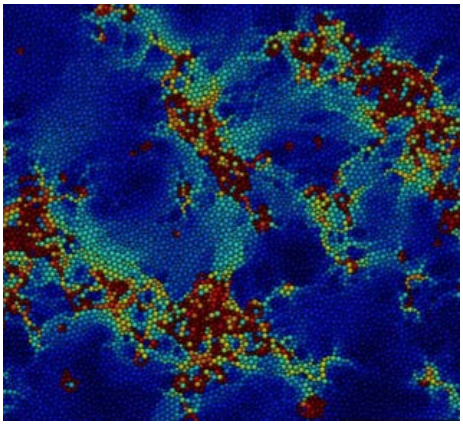

Figure 4.1 Snapshot of particle displacements in a two-dimensional supercooled mixture [88]. The blue colored atoms designate those that have negligible displacements while the most mobile atoms, which are displaced by at least a particle diameter, are represented as dark-red. A clear clustering of blue and red colored particles is evident, and this spatio-temporal segregation represents the dynamical heterogeneity of the system. The figure is reproduced from [88].

In this chapter, the signatures of dynamical heterogeneity (DH) is probed using atomistic simulations. In supercooled liquids, DH increases monotonically when cooled towards the

glass transition temperature (T_g). The somewhat imprecise correspondence between T_λ and T_g posited in earlier works [11] suggests that DH may increase monotonically in Type II superionics as the temperature approaches T_λ from below. The simulation results in this work instead shows a waxing and waning behavior of DH with increasing temperatures with the DH peaking between the temperatures T_α and T_λ. UO_2 is the chosen model fluorite material for demonstrating the DH behavior as the disordered state spans a wide temperature range ($T_\alpha \approx$ 1900 *K*, $T_\lambda \approx$ 2650 *K*) that will allow an unambiguous examination and interpretation of DH.

4.3 Detecting DH in the superionic state

Detecting DH in a superionic state is challenging for two reasons: First, the superionic states are completely in equilibrium enveloped by two well-defined thermodynamic states – liquid and crystal (solid). A supercooled state, in stark contrast, is in a frustrated, non-equilibrium condition, and is bounded by an equilibrium liquid and a non-equilibrium glassy state. Typically, DH is quantified by the generalized four point susceptibility function (χ_4) or through similar metrics [63, 89-92]. $\chi_4(t)$ has been introduced in Chapter 2, and the mathematical expression is given in Equation 2.33. In supercooled systems, the magnitude of $\chi_4(t)$-*max* shows a monotonic increase with decreasing temperature [93], illustrating the growing spatial correlations. For perfect crystals, $\chi_4(t)$ rather grows unbounded without decay, which indicates a practical difficulty to differentiate deeply supercooled states from the crystalline states, especially with MD simulations that have limited time windows. This can be seen in Figure 4.2 showing the variation of χ_4 for various temperatures. For temperatures slightly above T_α, in the range 1900 – 2300 *K*, χ_4 grows unbounded during the simulation time window (100 *ps*). Hence, χ_4 is not a suitable metric for studying superionic conductors owing to its inability to differentiate a crystalline state from a very deeply supercooled state.

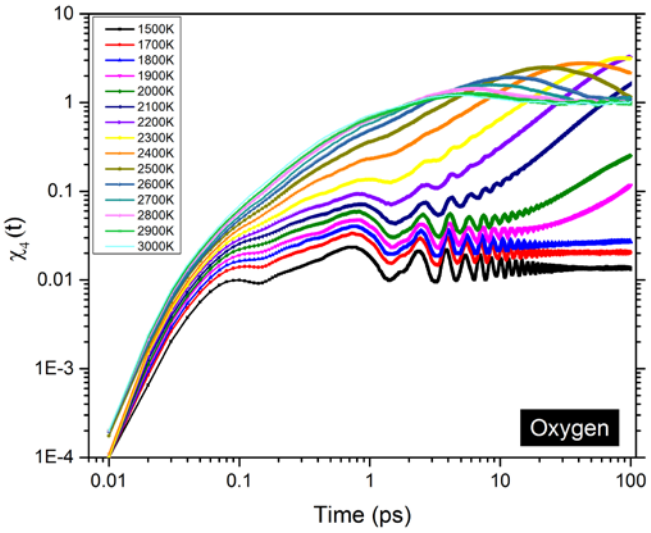

Figure 4.2 Variation of $\chi_4(t)$ for various temperatures in UO_2.

In this work, an alternate metric, namely, the correlation in the propensity – defined as the mean square displacement of an ion in an isoconfigurational ensemble [65, 94] – and the van Hove self–correlation function [59] are employed to uncover the onset of DH. The spatial correlation of the propensity (C_d) has been introduced in Chapter 2 and it is given by Equation 2.34. The equivalence of C_d and χ_4 in assessing spatially heterogeneous dynamics in supercooled systems is brought out in Figure 4.3, showing the time corresponding to the peak value of C_d and χ_4 at various temperatures, as observed in Kob-Andersen binary model system [14]. The correspondence of times as observed shows that C_d is also an excellent measure of DH. Most importantly, the mean value of C_d is nearly zero at all times for perfectly crystalline states, especially at low temperatures – MD simulations for several materials at temperatures close to 0 K have verified this. While thermal vibrations enhance the magnitude of C_d, it remains nearly constant, unlike χ_4, which increases monotonically, without bounds, with time in the crystalline states. The difference between χ_4 and C_d comes from the pair correlation in the latter that decays very quickly in the crystalline state.

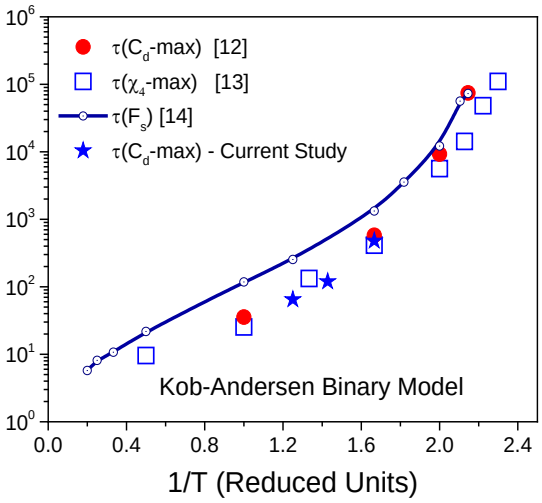

Figure 4.3 Comparison of $\tau(C_d\text{-max})$ [66] evaluated at r = 1 Å, $\tau(\chi_4\text{-max})$ [93] and α-relaxation time $\tau(F_s \rightarrow 0)$ [95] for the A atoms of Kob-Andersen binary model system [95]. $\tau(C_d\text{-max})$ is defined as the time at which C_d shows a maximum; $\tau(\chi_4\text{-max})$ is defined analogously. $\tau(F_s \rightarrow 0)$ is defined as the time for the density correlator to decay to an arbitrarily negligible value. While $\tau(\chi_4\text{-max})$ denotes scaled Monte-Carlo (MC) steps, $\tau(C_d\text{-max})$ and $\tau(F_s \rightarrow 0)$ for k = 7.25 are shown in MD reduced units followed in [95]. The good correlation between $\tau(C_d\text{-max})$ and $\tau(F_s \rightarrow 0)$ [as well as $\tau(\chi_4\text{-max})$] indicates that the spatial correlation of dynamic propensity $C_d(r,t)$ is a realistic metric that is comparable to $\chi_4(t)$ for predicting the dynamical heterogeneity (DH).

Figure 4.4 delineates the main result of our investigation on DH using $C_d(r,t)$ – it shows the progression of C_d evaluated at r = 2.63 Å, which is close to the O–O interionic separation distance; C_d is averaged over 100 independent isoconfigurational runs Further, Δr is chosen as 0.25 Å in this work. At 1500 *K*, C_d shows an oscillatory behavior that emanates from the vibratory motion of the oxygen ions; the mean value, however, remains constant for the whole duration of the simulation (500 *ps*). On increasing the temperature, C_d exhibits two discernible changes: (*i*) the magnitude of C_d that represents the strength of the correlation increases, and (*ii*) the magnitude gently increases and then decreases after passing through a maximum. Unlike in the supercooled states, C_d, however, exhibits a plateau-like period before decay. Thus

the correlation in the propensity draws out the transition from a crystalline state into a superionic state through an increased correlation strength, and a peaking and decay behavior in C_d that signifies the emergence of dynamical heterogeneity. With increasing temperature, the magnitude of C_d increases with the peaks being exhibited at lower times – the maximum amplitude can be observed at 2500 *K*. And on further increase in the temperature, the amplitude of C_d decreases.

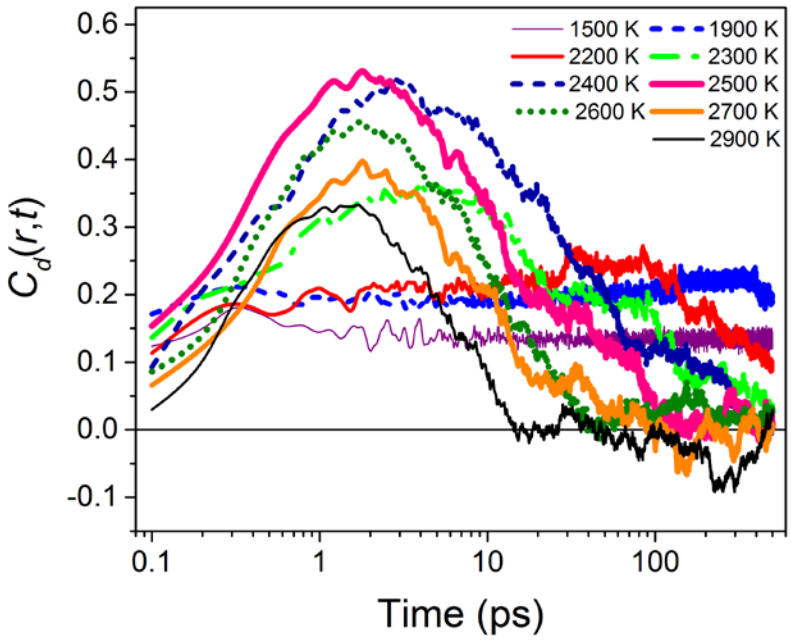

Figure 4.4 Spatial correlation of the dynamic propensity (C_d) of the oxygen ions in UO_2 evaluated in a restricted, isoconfigurational ensemble for different temperatures.

Figure 4.5 shows the variation of the peak magnitude of C_d, which depicts the waxing and waning behavior of DH among the oxygen ions. For temperatures 2200 *K* and 1900 *K*, the peak amplitude of C_d is determined as the mean value during the 'plateau' period: 30-80 *ps* and 200-400 *ps* for 2200 *K* and 1900 *K*, respectively. Based on the peak magnitudes of C_d, the maximum DH intensity can be regarded to fall in the temperature range of 2400 – 2500 *K*.

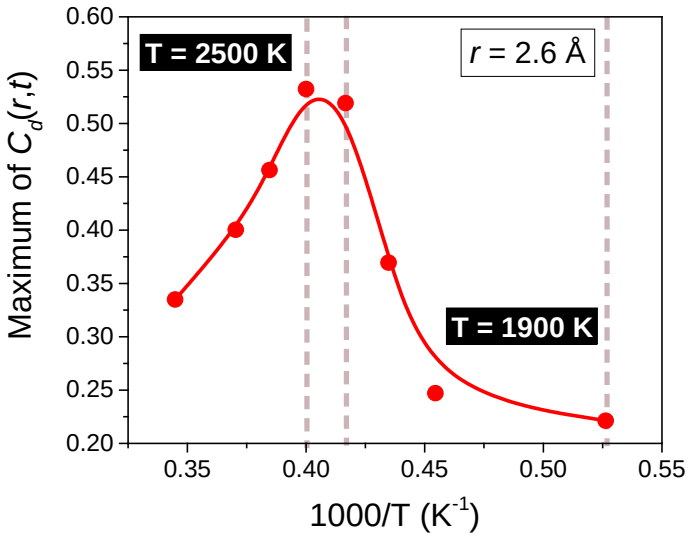

Figure 4.5 Waxing and waning of dynamical heterogeneity (DH) among the oxygen ions in UO_2, illustrated by the variation of the peak amplitude of C_d with temperature.

The temporal behavior of C_d reveals an early and late stage DH behavior with the former corresponding to the lower temperatures near T_α (1900 K – 2200 K) while the latter corresponding to the higher temperatures near T_λ (2300 K – 2900 K). The early stage is characterized by deviations from a constant C_d, low correlation strength, and relatively long periods of a plateau-like behavior, signifying correlated but hindered ionic motion. The low correlation strength also indicates that only a relatively small number of ions participate in the DH process. The early DH stage is distinctively different from that observed in typical supercooled liquids; given the preceding crystalline state, it can be characterized as solid-like. In contrast, the late DH stage is characterized by a significant strength in the correlations and a peaking behavior that is analogous to supercooled liquids. While only 500 *ps* to 1 *ns* have been simulated for the lower temperatures with MD, we have verified that the system remains in a vibratory state at temperatures lower than T_α using temperature accelerated dynamics (TAD) [48]. Since no transitions have been accepted in a perfect UO_2 crystal, TAD simulation results confirm the absence of diffusive motion for temperatures lower than T_α.

The crossover from the solid-like DH behavior to a more liquid-like response (at ~2300 *K*) has a structural origin. This is evident from Figure 4.6, which depicts the Wendt and Abraham ratio (R^{WA}) using the RDF of U-O ions. Even though the R^{WA} ratio for U-O ions has been shown earlier in Figure 3.7, the variation with inverse temperature is plotted here to highlight a two-state dynamical behavior. R^{WA} registers a slow increase from 1900 *K* to 2300 *K*, which corresponds to a low temperature (α_T) DH stage, followed by a more rapid increase at higher temperatures (λ_T stage). This result also shows that there is a discernible structural relaxation involving cations that contribute to the dynamical response. A similar conclusion can also be drawn from the O–O radial distribution function as well.

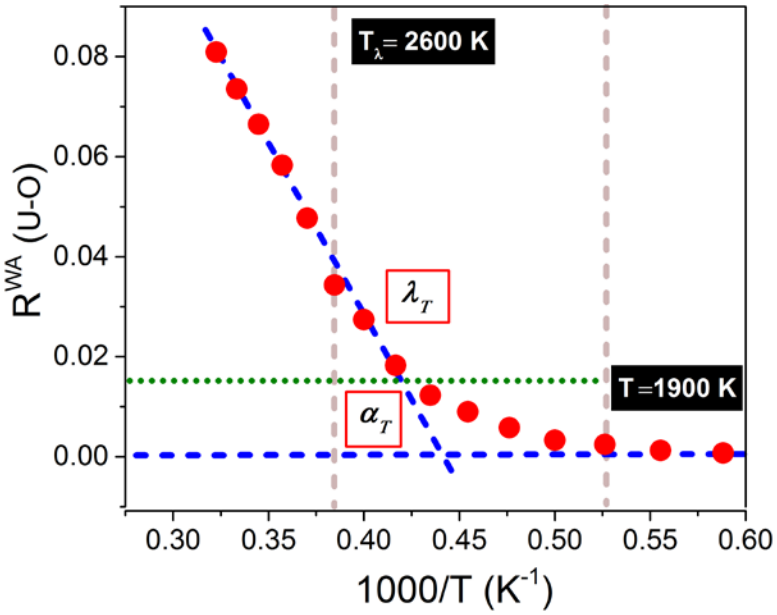

Figure 4.6 Wendt and Abraham ratio $R^{WA} \equiv g_{min}/g_{max}$, where g_{max} is the first peak value and g_{min} is the first minimum in the U-O RDF, respectively, showing a two stage dynamical behavior.

More evidence for the evolution of DH, as well as for the cross-over from solid-like to liquid-like behavior of the oxygen ions, can accessed through propensity maps. As introduced in

Chapter 2, propensity is defined as the mean square displacement of an atom or ion in an iso-configurational ensemble. Propensity maps have been used in the past [94, 96] to visually identify the dynamical clustering of atoms in the supercooled states; these are constructed in this dissertation by assigning a sphere of radius (r) to every oxygen ion, which is expressed as [97]:

$$r = R_{\min} \exp\left\{\left|\frac{(R_i - N/2)}{(1 - N/2)}\right| \log\left(\frac{R_{\max}}{R_{\min}}\right)\right\} \tag{4.1}$$

The initial position of oxygen ion in the iso-configuration ensemble is assigned a radius r, given by Equation 4.1, with $R_{\min}$ and $R_{\max}$ taking the values 0.01 Å and 0.5 Å, respectively [97]. R_i is a sorted integer rank of the propensity values from smallest to largest and varies from 1 to N, where N is the total number of oxygen ions in the simulation. The more mobile (top-half) ions are then colored green and by definition, the largest green spheres represent the most mobile oxygen ions in the system. For ions with rank R_i varying from 1 to $N/2$ (less mobile), the ranks are reversed before evaluating their radii; these are then assigned the color red. In this way, the largest red spheres represent the least mobile ions. The propensity maps are shown in Figure 4.7 for the oxygen ions in UO_2 for temperatures varying from 1900 K to 2900 K; DH is evaluated at a time when C_d shows a maximum in Figure 4.4. A remarkable evolution of DH among the oxygen ions can be noticed, which is depicted by the formation of heterogeneous clusters of slow (red) and fast (green) moving ions. From the onset at ~2000 K, the DH spreads spatially with increasing temperatures, and becomes most prominent at a temperature of 2500 K. DH then retracts with further increase in temperature, and by 2900 K, the dynamically heterogeneous regions have shrunk considerably. Thus a visually striking growth and reduction of DH in Type II superionics can be observed through the propensity maps.

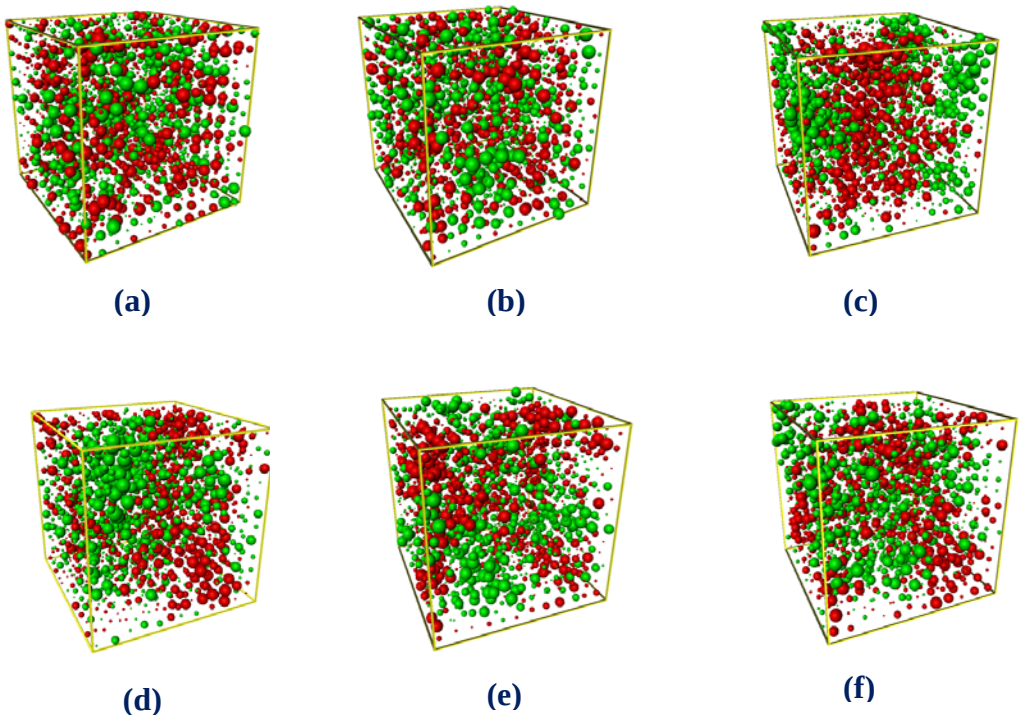

Figure 4.7 Propensity maps depicting the waxing and waning of dynamical heterogeneity of oxygen ions with temperature at times corresponding to the maximum in C_d. The maps correspond to temperatures, T = 1900 *K* at 100 *ps* (*a*), 2200 *K* at 80 *ps* (*b*), 2400 *K* at 3 *ps* (*c*), 2500 *K* at 2 *ps* (*d*), 2600 *K* at 2 *ps* (*e*) and 2900 *K* at 2 *ps* (*f*).

Another metric that is useful to characterize DH is the van Hove self-correlation function or $G_s(r,t)$. In equilibrium states, $G_s(r,t)$ is nearly Gaussian while in jammed states the tail of the distribution shows an exponential behavior [59]. Figure 4.8 depicts the time evolution of $G_s(r,t)$ for the oxygen ions in UO_2 at different temperatures. Two striking features can be observed: at temperatures above 1900 *K*, $G_s(r,t)$ deviates from the Gaussian shape and develops a tail, which (*i*) depicts discernible peaks, particularly prominent at longer times, and (*ii*) vary exponentially with distance at a time when C_d exhibits a peak amplitude (τ_α). The peaks are characteristic of hopping processes wherein ions undergo discrete jumps [98]; we have verified that the peak locations agree closely with the nearest neighbor positions in the O–O radial distribution function as shown in Figure 4.9. The exponential tail in $G_s(r,t)$, on the other hand,

connotes the presence of faster moving ions – the characteristic signature of DH – which is also observed in supercooled liquids, colloids and granular materials [59]. With increasing temperature, the exponential tail at τ_α strengthens, which confirms the presence of DH. The early and late stage DH can also be distinguished from the progression of the exponential tail. At 2200 *K*, the exponential tail in G_s at τ_α (80 *ps*), which is somewhat underdeveloped with corrugations, sustains for long periods of time suffering only a modest change, signifying a solid-like, early stage DH response. In contrast, at a temperature of 2400 *K* (and above), the G_s tail at τ_α is smoother, which is analogous to that in typical supercooled liquids, signifying a liquid-like, late stage DH response. At higher temperatures, the exponential tail of G_s also deteriorates faster.

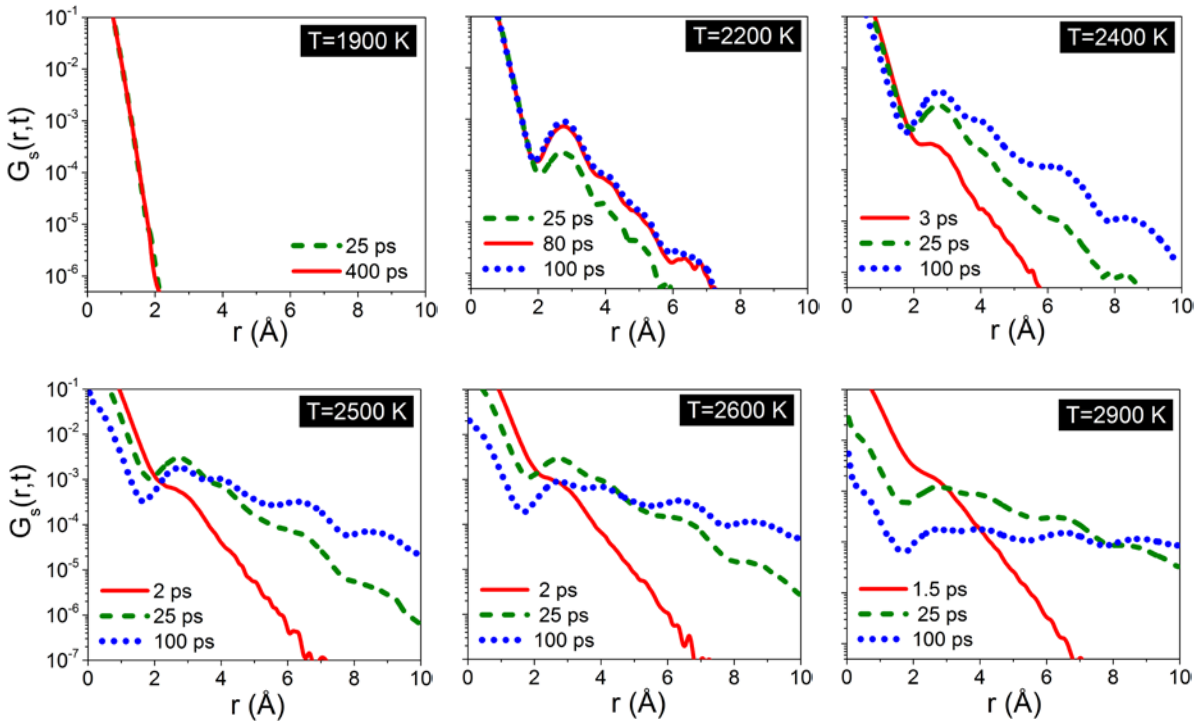

Figure 4.8 The evolution of van Hove self-correlation function $G_s(r,t)$ for the oxygen ions at different temperatures – the solid line corresponds to the time when C_d exhibits the peak amplitude.

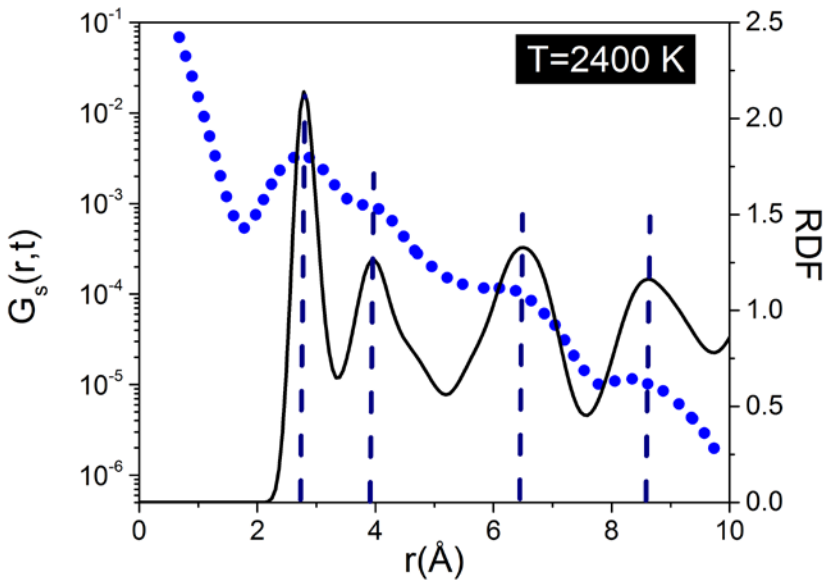

Figure 4.9 van Hove self-correlation function $G_s(r,t)$ for the oxygen ions at 2400 *K*, along with the corresponding anion RDF at the same temperature. The peaks in $G_s(r,t)$ match very well with the nearest neighbor positions obtained from the RDF.

Next the liquid-like behavior of the oxygen ions is analyzed through the density correlator $F(\mathbf{k},t)$ (see Figure 4.10) at various temperatures. A wave-vector of 0.28 $Å^{-1}$ is employed, which corresponds to the longest wavelength of the system. At lower temperatures, the long wavelength density fluctuations are correlated for somewhat longer periods of time, whereas at higher temperatures, they decay more rapidly with time. It is interesting to note that the tail of $F(\mathbf{k},t)$ at higher temperatures starts developing a low frequency oscillation, which is otherwise absent at lower temperatures. To analyze this frequency response, the Fourier transform of $F(\mathbf{k},t)$, also known as dynamic structure function, is investigated; it is delineated in Figure 4.11.

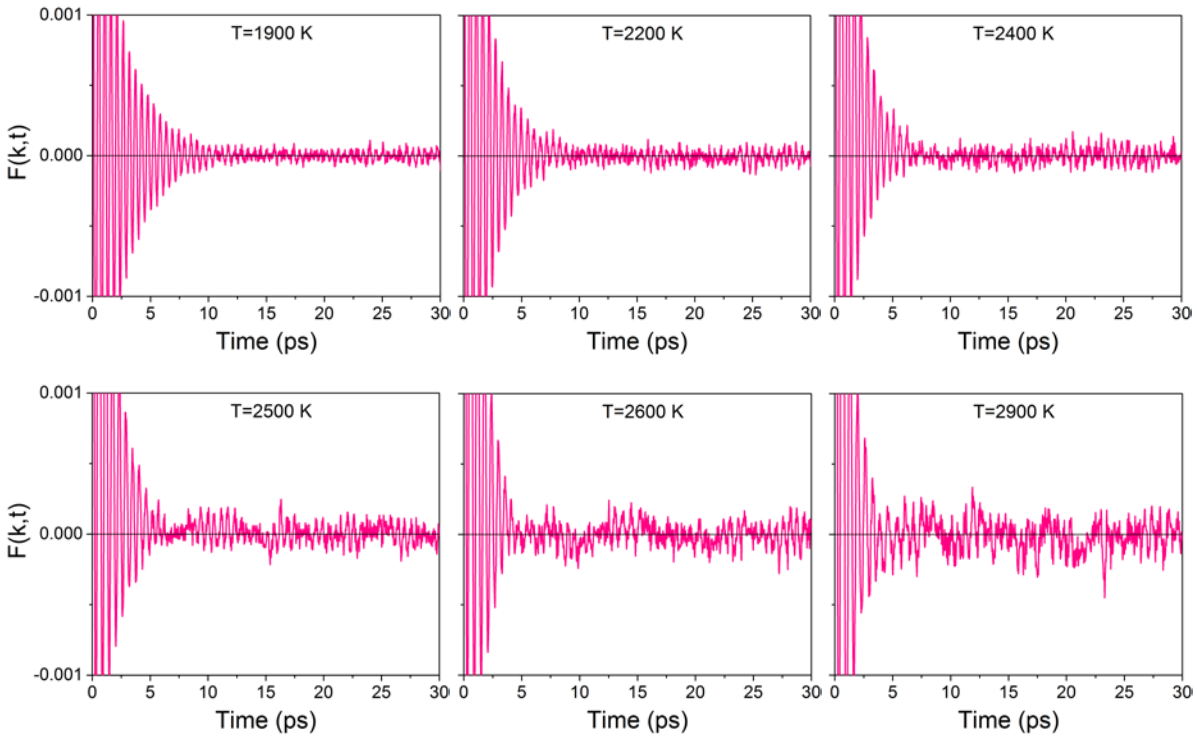

Figure 4.10 Intermediate scattering function for oxygen ions at different temperatures in UO_2. The wave vector, *k*, is chosen as 0.28 $Å^{-1}$, which is representative of the hydrodynamic limit.

At all temperatures, there is a prominent peak at higher frequencies (around 2 T*Hz*) – known as elastic peak, indicating the vibratory motion of ions. For 1900 $K > T < 2200$ *K*, a partially-formed hydrodynamic (at $\nu \approx 0$) is discernible, indicating a somewhat lethargic disordering mechanism. This peak, also known as Rayleigh peak, represents the cooperative motion of oxygen ions. The Rayleigh peak, however, becomes unmistakable with increasing temperature and its magnitude relative to that of the elastic peak again confirms a liquid-like state beyond 2400 *K*. Thus the cross-over from a solid-like state to a more liquid–like state can be confirmed through the evolution of the dynamic structure function.

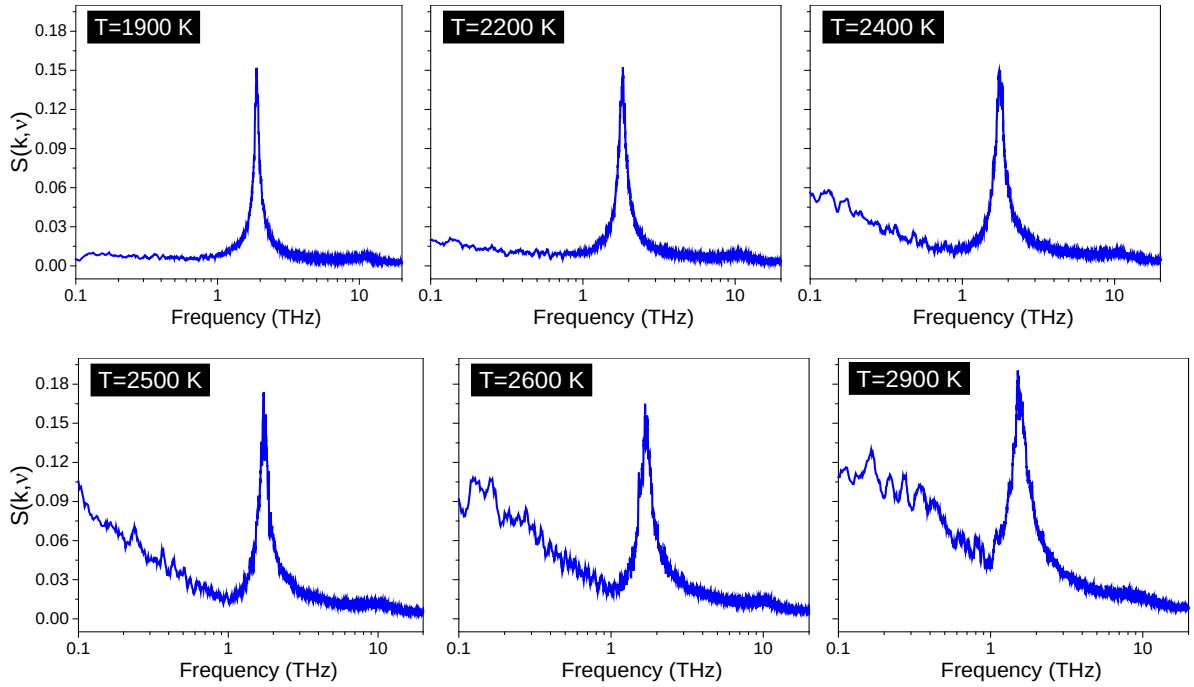

Figure 4.11 Partial dynamic structure function for oxygen ions (arbitrary units) for a wave vector of $k = 0.28$ Å^{-1}, which is representative of the hydrodynamic limit.

4.4 Conclusions

This chapter has addressed the question: Do superionic conductors exhibit dynamical heterogeneity (DH) – a characteristic and a universal feature of glassy and jammed states? Using molecular dynamics (MD) simulations of UO_2, a model Type II superionic conductor, a complex manifestation of DH among the oxygen ions over a range of temperatures has been demonstrated. Illustrated by the correlations in the propensity, DH has been shown to advance from a well–marked onset temperature (T_α), peak at an intermediate temperature between T_α and T_λ, and then recede. This work has also highlighted an importance difference in that the strengthening of DH and cooperativity in supercooled liquids is aided by decreasing entropy, whereas, the DH in superionic conductors evolves against the destabilizing effect of entropy. Hence, unlike in supercooled liquids, the DH in superionic conductors waxes and wanes with increasing temperature [84] – a non-monotonic behavior that is noticeably absent in supercooled liquids.

Chapter 5: MOBILITY PROPAGATION AND DYNAMIC FACILITATION IN TYPE II SUPERIONIC CONDUCTORS

5.1 Introduction

In Chapter 4, it is established that the disordered mobile anions exhibit non-monotonic variation of dynamical heterogeneity (DH) in Type II superionic conductors [84]. This non-monotonic behavior is different from the well-known linear increase of DH in supercooled liquids when cooled towards the glass-transition temperature, T_g. In this chapter, the underlying mechanism for the observed rise and fall of DH in superionics is investigated using the concept of *dynamic facilitation* (DF).

While unambiguous support for DH in supercooled and glassy states comes from several experiments as well as theoretical work [16], a clear mechanistic origin for DH is nebulous. In the Random First Order Transition (RFOT) theory, it is postulated that a dynamically arrested liquid exhibits a diverse number of metastable states and the state of the system assumes a mosaic structure with different patches corresponding to the metastable states or inherent states [99]. It has been shown recently that RFOT predicts different shapes for the cooperatively rearranging regions (CRRs) [100]; string-like configurations dominate near the Mode Coupling Transition (MCT) temperature (T_c) while compact configurations are expected near the glass transition temperature (T_g). According to kinematically constrained models [101], DH arises as a consequence of mobile atoms facilitating mobility to the adjacent

atoms [102]. It is also shown that structural relaxation in glass-forming liquids arises through the dynamics of elementary excitations that are facilitated and hierarchical [88].

5.2 Dynamic facilitation (DF)

The spatial segregation of relaxation times leading to spatially-heterogeneous dynamics can be explained by means of dynamic facilitation (DF). The concept of DF is closely related to DH in that the mobile clusters can be decomposed into smaller dynamical subunits [103] with spatiotemporal correlations between them; the dynamical events facilitate subsequent dynamics in neighboring particles leading to large-scale DH over time. Hence, DF forecasts that when particles in a microscopic region are mobile, they assist the particles in neighboring regions to become mobile, thereby allowing mobility to propagate continuously and in a spatially correlated way. To illustrate this, in Figure 5.1, a sample two-dimensional lattice system is portrayed depicting two possible evolutions of mobility in superionics. The left panel (*a*) represents a system exhibiting DF, wherein the mobility is propagated only through mobile atoms while the right panel (*b*) represents random evolution of mobility. The former encapsulates the idea of facilitated dynamics of Garrahan and Chandler [104] where ion mobility is sparse and directional with mobile ions imparting their mobility to physically adjacent ions.

Dynamic facilitation, in the approach developed by Chandler, Garrahan and co-workers, plays a key role in the structural response of an arrested state; a jammed region can become unjammed only if it is physically adjacent to a mobile region [105]. This particularly restrictive condition make the DF idea unique [101] and at odds with the spontaneous and random generation of mobile and immobile regions [106]. DF is also predicted within the RFOT approach though not as a cause but as a consequence of relaxation of the mosaic regions

[107]. In this chapter, atomistic simulations of two Type II superionic conductors, UO_2 and CaF_2 are performed to probe the presence of DF. The chief metric applied to identify DF is the *mobility transfer function* that has been used in the past to quantify DF in supercooled liquids. The general simulation details are given in Section 3.3 of Chapter 3. In the next section, the formulation of mobility transfer function is presented along with the relevant results.

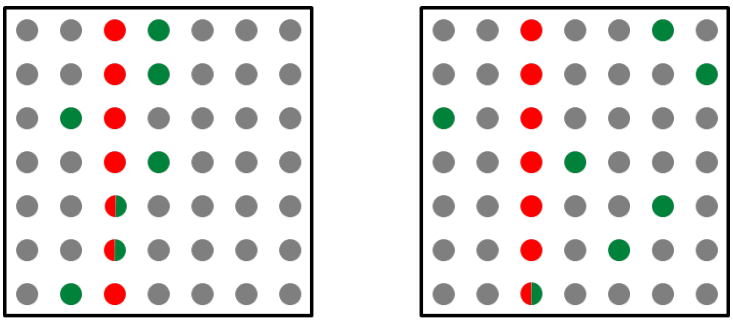

Figure 5.1 Illustration of DF on a two-dimensional lattice. Δt_{12} and Δt_{23} are back-to-back time intervals of equal length. Red (green) ions represent the most mobile ions – top 5%, during time interval Δt_{12} (Δt_{23}). Dual colored ions represent the most mobile ions for both time intervals. Left panel (*a*) represents a system exhibiting DF, where mobility is propagated only through mobile atoms while right panel (*b*) represents random evolution of mobility.

5.3 Mobility transfer function

In this work, the Mobility Transfer Function [108-110] is employed to assess whether dynamics is facilitated in superionic conductors. This function gives the probability of a neighbor of a mobile ion becoming mobile, relative to that of a random ion becoming mobile. Values close to unity indicate that the mobility is randomly transferred while higher values indicate the proclivity for mobile ions to transfer their mobility to physically adjacent immobile ions. Ion mobility in a time interval Δt_{12} (from time t_1 to t_2) is first evaluated followed by constructing a list of all the ions that are most mobile; the top 5%, is employed in this work,

which is consistent with the past investigations of supercooled liquids. It should be noted here, however, that only anions are considered as only they become mobile above T_α; they typically hop from one lattice site to another in a collective manner [84] without forming permanent defects. Also note that only the anions have been considered in the study of DH in Chapter 4. Next a second list of the most mobile ions (top 5%) in the subsequent time interval, Δt_{23}, is generated; here, Δt_{12} and Δt_{23} are back-to-back time intervals with $\Delta t_{12} = \Delta t_{23} = \Delta t$. A probability distribution $P_F(r,\Delta t)$ of finding the smallest distance r between an ion that is mobile in Δt_{23} but not in Δt_{12}, and any of the mobile ions in Δt_{12} is then computed; the configuration of system at the intermediate time t_2 is employed in evaluating these relative distances. This distribution is then compared with $P_F^*(r,\Delta t)$, a distribution representing random ion mobility. In the latter case, all the mobile ions in Δt_{23} are randomly selected from non-mobile ions in Δt_{12}. If dynamics is facilitated, then $P_F(r,\Delta t)$ will have a higher first neighbor peak relative to that in $P_F^*(r,\Delta t)$. Identical distributions, however, will reflect random mobility propagation in the system [108-110].

Figure 5.2 depicts the spatial variation of $P_F(r,\Delta t)$ and $P_F^*(r,\Delta t)$ for CaF_2 at two different temperatures, T = 1400 K and 1600 K with a Δt of 1.0 ps. The lower temperature (1400 K) is below T_λ where DH is expected to be most prominent, while the higher temperature (1600 K) is above T_λ but below the melting point. As noticed from the left panel (*a*), the first neighbor peak for $P_F(r,\Delta t)$ is significantly higher than that of $P_F^*(r,\Delta t)$, which demonstrates that the probability of an anion becoming mobile in Δt_{23} is much higher if it is located in close proximity to an anion that was mobile during Δt_{12}. However, for the same Δt at 1600 K (see right panel in Figure 5.2), the two distributions are almost identical implying that mobile ions in back-to-back time intervals are almost uncorrelated. Thus dynamics is strongly facilitated

at a temperature of 1400 *K* but not at 1600 *K*. The distributions delineated in Figure 5.3 invoke an identical conclusion for UO_2 thereby strongly suggesting that facilitated dynamics and the ensuing dynamical heterogeneity is likely to be a hallmark of a large class of Type II superionic conductors.

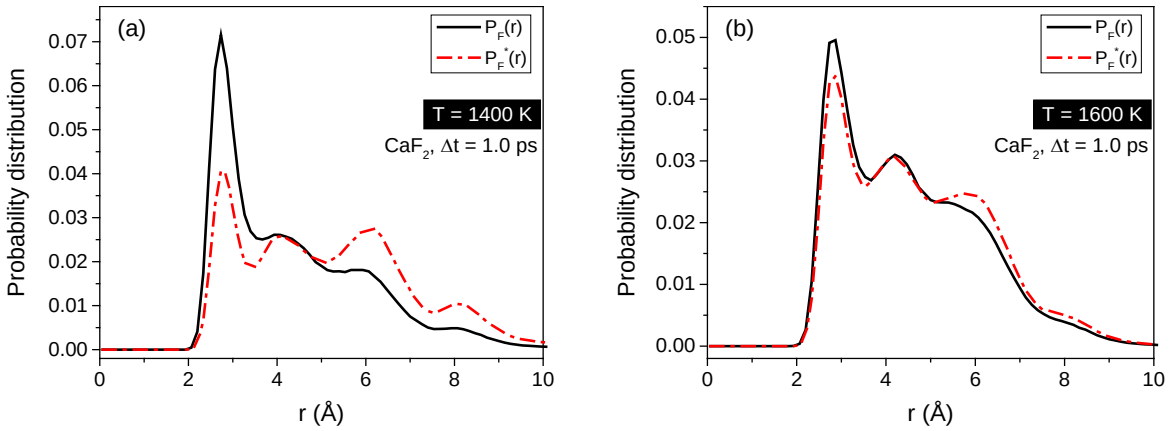

Figure 5.2 Probability distributions $P_F(r)$ and $P_F^*(r)$ for fluorine ions at (*a*) 1400 *K* and (*b*) 1600 *K*.

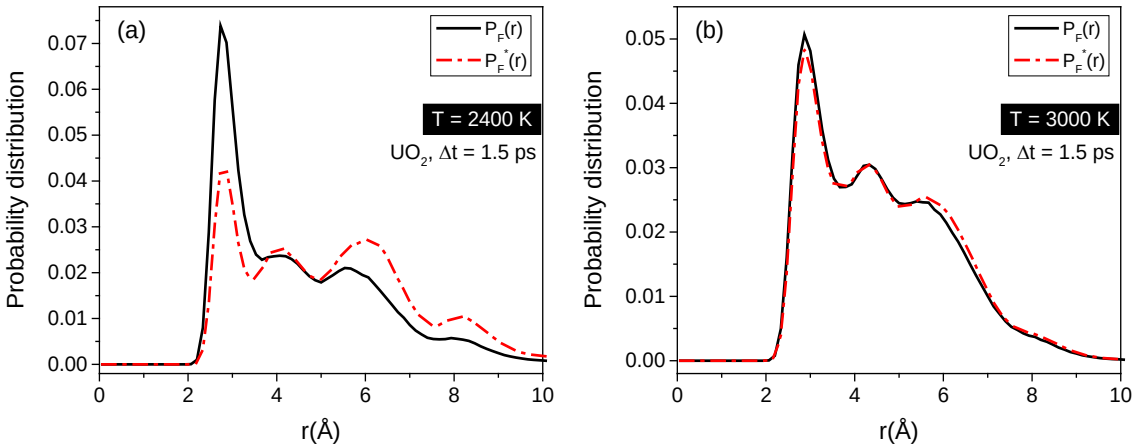

Figure 5.3 Probability distributions $P_F(r)$ and $P_F^*(r)$ for oxygen ions at (*a*) 2400 *K* and (*b*) 3000 *K*.

The strength of DF at any temperature T can now be quantified by using mobility transfer function [111], defined as:

$$F\left(\Delta t,T\right)=\frac{\int_0^{r_{min}} P_F\left(r,\Delta t,T\right)}{\int_0^{r_{min}} P_F^*\left(r,\Delta t,T\right)} \tag{5.1}$$

where r_{min} denotes the first non-zero minimum in the anion partial radial-distribution function at the temperature of interest. Thus $F(\Delta t,T)$ is a measure of the probability for an immediate neighbor of a mobile ion becoming mobile (left panel in Figure 5.1) relative to that of a random ion becoming mobile (right panel in Figure 5.1). Values close to 1 indicate that the mobility is randomly transferred but higher values indicate the proclivity for mobile regions to arise near regions that were previously mobile. In Figure 5.4, $F(\Delta t)$ for both CaF_2 (left panel) and UO_2 (right panel) for various values of Δt and at different temperatures are depicted.

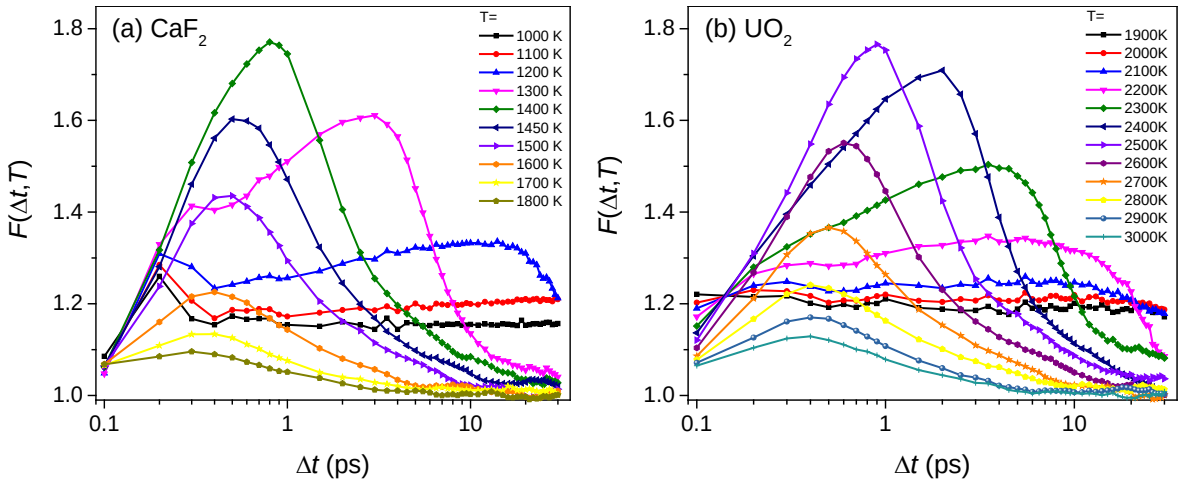

Figure 5.4 Mobility transfer function $F(\Delta t,T)$ representing the strength of dynamic facilitation, for (*a*) CaF_2 and (*b*) UO_2 over different temperatures and time-intervals. Both CaF_2 and UO_2 show similar variation of $F(\Delta t,T)$ which may indicate a universality of dynamic facilitation in Type II superionic conductors.

For temperatures below T_α, $F(\Delta t)$ shows a near-flat response over all values of Δt indicating that the dynamics is mostly random and non-facilitated. At temperatures near and slightly above T_α (1200 *K* for CaF_2, and 2200 *K* for UO_2), a distinct but not a fully formed peak can be identified at long times for both CaF_2 and UO_2. Thus an early signature of DF can be detected above the order-disorder transition temperature. In other words, with the advent of disorder in the anions, the dynamics is distinctly manifested as facilitated and not random. The peak in $F(\Delta t)$ increases with increasing temperatures; the shifting to lower values of Δt shows that the relaxation time is significantly shorter at higher temperatures. The peak value of $F(\Delta t)$ becomes maximum at a characteristic temperature close to T_λ for both CaF_2 and UO_2. Interestingly, the peak value of 1.8 (in both cases) is very similar to that observed in moderately supercooled states [108, 109] as well as in colloidal suspensions [112]. Thus there appears to be a convincing evidence to conjecture that dynamic facilitation is inherent to all Type II superionic conductors.

5.4 Comparison of mobility transfer function with the correlations in propensity

In Chapter 4, DH is established at temperatures above T_α using dynamical correlations of propensity (C_d) in UO_2. It is revealed that the peak value in C_d starts increasing at a temperature close to T_α, portrays a maximum at an intermediate temperature near T_λ, and then recedes. Figure 5.5 depicts the peak values of $F(\Delta t)$ at different temperatures for UO_2 and CaF_2, and compares that of C_d (only for UO_2). It is interesting to note that both the metrics show a near identical variation. This remarkable waxing and waning behavior of the peak values of C_d and $F(\Delta t)$ is compelling enough to conclude that dynamic facilitation is intimately associated with the spatially heterogeneous dynamics in Type II superionic conductors.

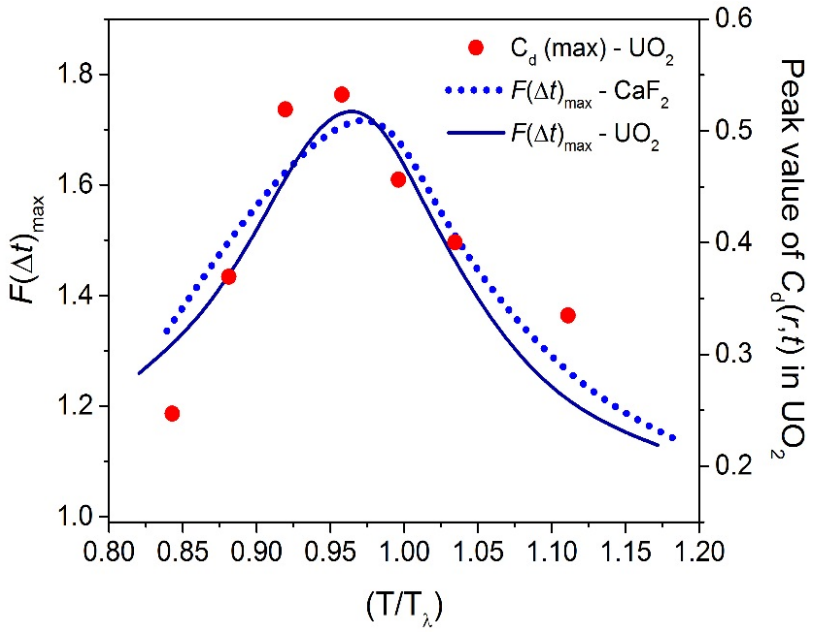

Figure 5.5 Waxing and waning behavior of DF in CaF_2 and UO_2 illustrated by the variation of maximum value of $F(\Delta t)$ – a measure of DF – with temperature, and comparison to the peak values of C_d (for UO_2) – a measure of DH.

5.5 Conclusions

In Chapter 4, the spatially-heterogeneous dynamics of anions in UO_2 as accompanied by the presence of dynamical heterogeneity (DH) is revealed. In the present chapter, using atomistic simulations, it is demonstrated that, in tandem with DH, there is a very clear evidence for dynamical facilitation (DF) in two model superionic conductors, CaF_2 and UO_2 [113]. DF, as originally introduced in the investigation of supercooled liquids, asserts that spatial regions that undergo relaxation *facilitates* subsequent relaxation in neighboring regions. Using a standard marker of DF, the mobility transfer function, DF in superionics is shown to vary non-monotonically with temperature with an initial rise starting at the order-disorder transition temperature (T_α), peaking at an intermediate temperature, and rapidly decreasing at temperatures close to the superionic transition temperature (T_λ). Both the metrics quantifying

DH and DF show remarkable correspondence; the intensity of facilitated relaxation is observed to be closely correlated to the strength of DH, as would be expected if DH originates through facilitated dynamics. Thus, in this chapter, it is established that dynamic facilitation is most likely to underpin the heterogeneous dynamics in Type II superionic conductors.

Chapter 6: ONE-DIMENSIONAL STRING-LIKE MOTION OF MOBILE IONS IN SUPERIONIC CONDUCTORS

6.1 Introduction

It is now increasingly accepted that jammed systems that vary widely in microscopic detail such as glasses, supercooled liquids and granular media show similar dynamical behavior. The current work has strengthened the known similarities between superionics and prototypical glassy states [11, 87] by establishing the manifestation of dynamical heterogeneity (DH) and dynamic facilitation (DF) in the former [84, 113]. As discussed in Chapter 1, superionics have a close correspondence with fragile glasses with similar relaxation of time-correlation functions and a non-Arrhenius variation of slowly varying properties (such as resistivity and viscosity) with temperature. In glasses, it is known that the loss of fluidity close to T_g is largely dynamic in nature without significant structural changes; the relaxation in such crowded or jammed states occurs through cooperative rearrangement regions (CRR) involving many particle units. Several studies have demonstrated that the cooperative motion can take place in the form of string-like particle rearrangements and they may be a concrete realization of the CRR [114, 115]; as discussed earlier [100], string-like configurations are known to dominate near the Mode Coupling Transition (MCT) temperature (T_c) while compact configurations are expected near the glass transition temperature (T_g). In this chapter, the presence of low-dimensional string-like mobile units is investigated in Type II superionic conductors above and below the order-disorder transition temperature (T_α). Even though superionics are devoid

of obvious crowded or jammed conditions, string-like cooperative motion may explain the high ionic conductivities in superionic conductors.

6.2 Cooperative motion in superionic conductors

In Chapter 1, it has been discussed that the temperature variation of conductivity displays a non-Arrhenius character, signifying the presence of more complex processes aiding ion diffusion, apart from a simple vacancy or interstitial migration. Added to that, the Haven's ratio [116], defined as the ratio of observed conductivity to that obtained from the Nernst-Einstein equation assuming independent motion of defects, is greater than unity suggesting a possible cooperative behavior during the motion of defects [11]. Except for a lone theory of cooperative motion by Yokota [117, 118], there has been no fundamental inquiries into the mechanism of high ionic conductivities in superionics. The *caterpillar* mechanism proposed by Yokota rationalizes the observed decrease in the ratio of self-diffusion coefficient (D) to the mobility (μ) of mobile Ag^+ ions in superionic α-Ag_2S and similar Ag_2X compounds [117, 118]. The value of D has been estimated using radioactive tracer diffusion technique and the mobility from ionic-conductivity measurements, with μ proportional to the measured conductivity. Yokota argued for a caterpillar kind of motion that evolves from correlated successive jumps of a diffusing ion (which is non-Markovian, by definition). In this mechanism, an ion occupying a regular site is able to jump not only to a vacant neighboring site but also, with somewhat smaller probability, into an occupied one by inducing the ion on the latter site to make a jump. A sequence of jumps, with each ion replacing the next lattice ion, takes place culminating with an ion jumping into an adjoining vacant site (see Figure 6.1). The ions participating in the caterpillar mechanism thus make cooperative jumps along a line or at least are positively correlated with the jump direction of first ion. The n successive jumps

shown in Figure 6.1 will contribute *n* steps to the electrical/mutual diffusion conduction process while contributing only one step to the self-diffusion of any ion involved in the chain. The smallness of the activation energies for the diffusion of disordered silver ions in these compounds (~ 0.1 *eV*) is the cited justification for the possibility of correlated ion jumps into an occupied site as shown in Figure 6.1.

Figure 6.1 Caterpillar mechanism [117]: Cooperative jumps of *n* ions. All the sites from 0 to *n*-1 are initially filled and the caterpillar event displaces (shown by arrows) each ion by one atomic distance, or, equivalently, transfers the vacancy by *n* steps in the opposite direction.

In this work, we search for possible string-like, cooperative motion among the mobile species of Type II superionics. Slow but cooperative atomic motion has been observed in MD simulations of bulk dynamics of a wide range of glass forming liquids [119], grain boundaries of polycrystalline materials [120], and in the interfaces of nanoparticles [121]. In these systems, the identification of collective motion starts with a consideration of the relative displacement of particles. Since in superionics the ions hop between quantized lattice (tetrahedral) sites with very brief sojourn away from them (this will be explained in Chapter 7 in more detail), a new methodology is developed for identifying possible string-like motion. During any time-interval, all the ions that hop to a new lattice site are considered and any possible string-like motion, in which each ion replaces the next ion in the string, is easily detected; an illustration of this kind of motion is shown in Figure 6.2. Note that the string-like motion as defined would differ from caterpillar mechanism in that the ions involved in the concerted string motion can jump in *any* direction, which is uncorrelated to the jump direction of the remaining ions. The length of the string *n* is defined as the number of ions participating

in correlated motion. For example, the string in Figure 6.2, ($A \rightarrow B$, $B \rightarrow C$, $C \rightarrow D$), has $n = 3$. The study of string-like motion is ubiquitous in supercooled glass-forming systems and is known to aid in structural relaxation, with the length of the strings growing with decreasing temperatures. It is plausible that string motion, if detected in superionics, can explain the higher conductivities as numerous ions will be displaced in one event, or, as can more easily be seen from Figure 6.2, a vacancy/defect can be transported several atomic steps through a single concerted displacement.

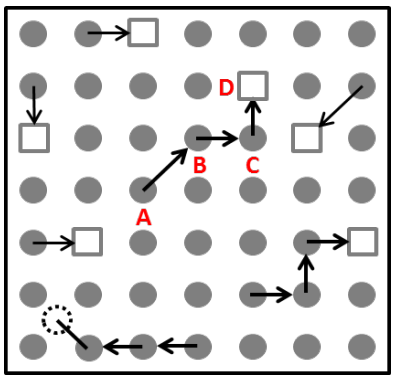

Figure 6.2 A schematic of a two-dimensional system with string-like cooperative event taking place on adjoining lattice sites *A*, *B*, *C*, and *D*. The ions initially belonging to *A*, *B*, and *C* make *simultaneous* transitions (represented by arrows) to *B*, *C*, and *D*, respectively. In this manner, each ion replaces the next ion in the string. While several transitions are shown, the string-like events are distinguished by thicker arrows.

6.3 Simulations

For temperatures above T_α where the anions show appreciable diffusion, standard atomistic (MD) simulations are conducted to investigate plausible string-like cooperative motion of ions. At lower temperatures where diffusive-events take place on the time-scale of microseconds or longer (and beyond the reach of normal MD simulations), temperature-accelerated dynamics (TAD) is applied to investigate the ionic motion. TAD is a method for accelerating the

dynamics of activated events in the solid state and is discussed in Chapter 2. Two model superionic conductors, UO_2 and CaF_2, are investigated in this work. The general simulation details are given in Section 3.3. To identify string-like correlated motion, the system is compared to a zero-defect perfect crystal structure of similar volume; an ion is assigned to one of the lattice sites if it is inside a sphere of radius 1 Å centered on the site. By checking the configuration of the system at regular intervals and making a list of all recent ion jumps, it is possible to identify any string-like cooperative motion. For the case of TAD analysis, the software package LAMMPS is used to perform the simulations [122]. For identifying cooperative motion, the configuration of the system is tracked only when any of the ions in the system has moved at least a pre-defined distance (chosen as $a/2$, the closest distance between two anion sites).

6.3.1 One-dimensional string-like motion of mobile atoms from MD simulations

A string-like cooperative motion involves *simultaneous* jumps of more than one ion to neighboring lattice sites, each ion supplanting the next ion in the string and culminating with the last ion jumping into a vacant site or into a site by inducing an existing ion to an interstitial position (hence, no further simultaneous transition is possible from this site). Figure 6.2 shows a three-ion string-like motion in which every ion replaces the next ion in the string. The ion displacement can be in any direction spanned by the three-dimensional space. An ion making a transition (hopping) between two lattice sites, say, *A* to *B*, can reside in an interstitial position for any amount of time after leaving *A*, and before entering *B*. However, all hoppings to the new sites must occur during the same-interval to be considered for participating in a cooperative event. In this work, the presence of strings are investigated for various time-

intervals Δt; here, the successive configurations of the system are separated by Δt for identifying string-like motion. In Figure 6.2, if the first ion makes a transition to *B* (i.e. lying within 1 Å from site *B*), second ion to *C*, and third ion to *D* during the same time interval, it's considered a string-like cooperative motion. By making a list of all ions and their respective lattice sites and identifying all ion jumps between successive configurations, all cooperative jumps can be detected.

In fluorite-superionics, the anions generally diffuse by rare and intermittent hopping, rather than continuous liquid-like diffusion even at high temperatures. This is evident from Table 6.1 which depicts the ratio of average residence time at a lattice site (before the ion is associated with a different site) per transition to the average hopping time for oxygen ions in UO_2. For example, at 2100 *K*, an oxygen ion stays at a lattice site, on average, for ~1 *ns* before making a jump, which typically takes only ~0.5 *ps*. From Table 6.1, it can be noted that the residence time is one to three orders of magnitude larger compared to the hopping time, indicating an occasional hopping event interspersed between prolonged tethering at the native lattice sites. Similar dynamical patterns are also observed for CaF_2, and are likely to be universal for all Type II superionic conductors.

The reason for very infrequent hopping can become apparent by evaluating the average lifetime of a vacant site, before it is filled, on the mobile ion sub-lattice. Longer lifetime shows that ions are slow to hop onto available neighboring sites (kinetically-inhibited), while shorter lifetimes indicate that rare hopping motion is a consequence of very few vacancies generated (thermally-inhibited). In Figure 6.3, the average lifetime of an anion vacant site before it is occupied by a hopping ion for both UO_2 and CaF_2 is depicted.

Table 6.1 Ratio of residence time to hopping time for oxygen ions at different temperatures in UO_2. The hopping time typically varies between 0.4 to 0.5 *ps* at all the temperatures. Note that $T_\alpha \sim 2000\ K$, and $T_\lambda \sim 2650\ K$ for UO_2.

Temperature (*K*)	Average residence time per hopping (*ps*)	Ratio of residence time to hopping time
2000	2621	5118
2100	983	1984
2200	280	602
2300	106	236
2400	45.65	104.4
2500	19.44	44.51
2600	10.70	24.3
2700	6.92	15.57

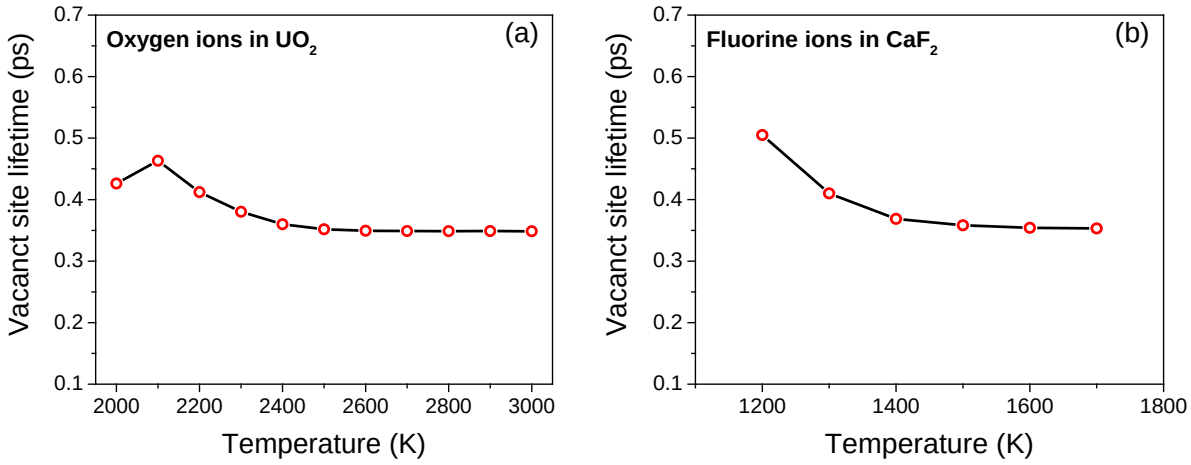

Figure 6.3 Vacant site lifetime as a function of temperature for (*a*) oxygen sub-lattice in UO_2 and (*b*) fluorine ions in CaF_2. The lifetime is close to 0.4 *ps* at all temperatures studied.

Figure 6.3 indicates that once a vacancy is generated, by the migration of an ion on that site to an interstitial position or a neighboring site, it takes nearly 0.4 *ps* for a new ion to exchange position with the vacancy. Since the duration of hopping motion is also close to 0.4 – 0.5 *ps*, hence, once a vacancy is created, an ion from an adjacent lattice site *swiftly* jumps to replace the vacancy. This poses a question: apart from ions that jump as soon as on detecting a nearby

thermally-generated vacancy, are there any ions that jump on to an occupied neighboring site and induces the ions occupying them to make a further transition? Figure 6.4 depicts the probability distribution of finding a string of length *n* versus *n* at three different temperatures among the oxygen ions in UO_2; a time-interval (Δt) of 0.2 *ps* is employed, which is half of the average hopping time. The figure clearly indicates the cooperative nature during the motion of anions, with each ion inducing the next ion in the string to move cooperatively.

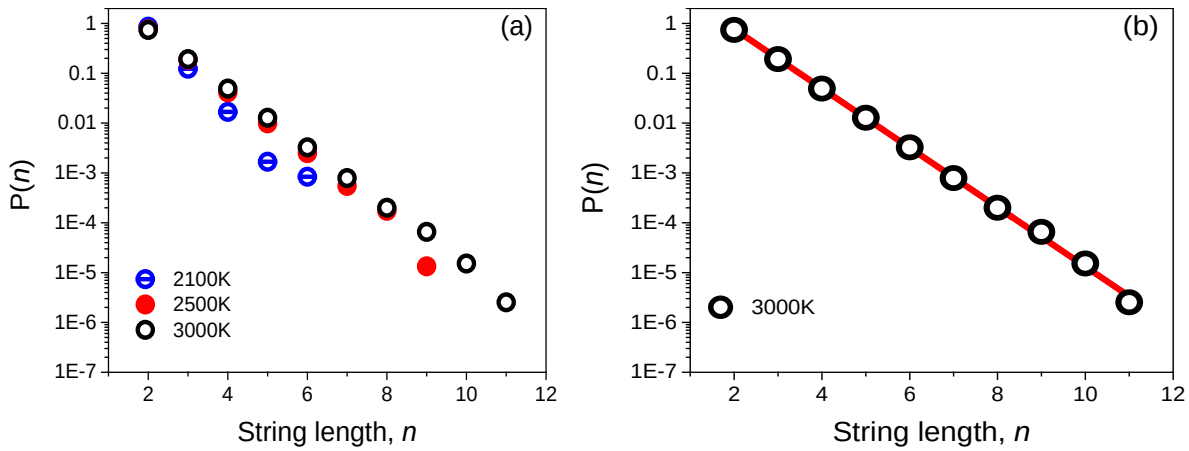

Figure 6.4 (*a*) Probability distribution of a string of length *n* versus *n* at three different temperatures in UO_2. The time interval is chosen as 0.2 *ps*. (*b*) The exponential nature of string probability distribution at 3000 *K*.

As in supercooled and jammed states, string-like ion displacements are clearly observed in superionics; the manifestation of longer strings with increasing temperature is also quite clear from Figure 6.4. It is somewhat surprising to observe long strings comprising of as many as 11 oxygen ions for such a short time-interval, even though most of the strings are comprised of two or three participating ions. Remarkably, the probability distribution of the length of the strings is exponential. Similar exponential behavior has been identified for supercooled liquid states [123]. An illustration of the configuration of ions exhibiting string-like cooperative

motion in UO_2 is shown in Figure 6.5. Here, a string of 11 ions is chosen, at a temperature of 3000 *K* and $\Delta t = 0.2$ *ps*. Each ion replaces the next ion in the string within Δt.

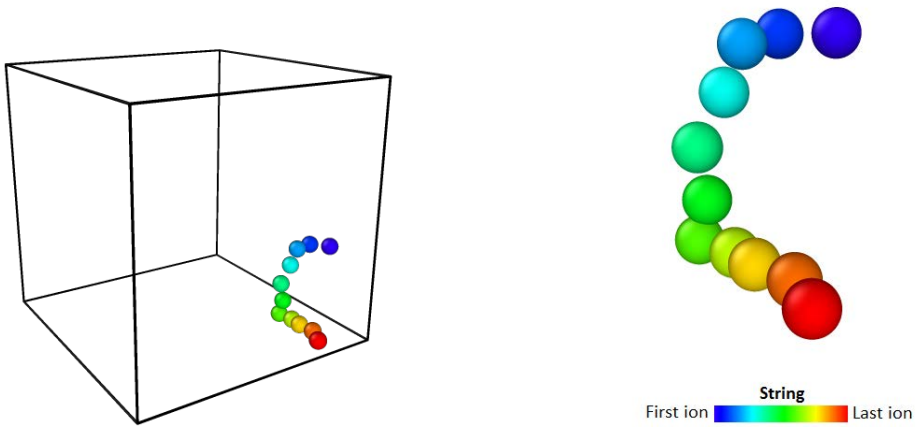

Figure 6.5 An illustration of string-like cooperative motion of oxygen ions in UO_2 at 3000 *K*. Each ion jumps to the position of next ion in the string within the time-interval of 0.2 *ps*. To show the direction of the ion-replacements, the ions are colored from first to last ion of the string.

By choosing longer time intervals between the snapshots of the particle configurations, longer strings can be observed. This can be understood as follows: Since the mobile ions in superionics sporadically hop onto neighboring sites, by choosing a longer interval between two configurations, more number of ions can be seen to make a transition during this period, resulting in a higher probability for detecting a string-like cooperative motion. However, very long intervals can result in non-physical strings with some of the ions jumping much farther than neighboring sites and being involved in more than one hopping. Table 6.2 shows the time-interval between two configurations that would enable 1% of the mobile ions to be involved in a string-like cooperative motion in UO_2. The time-interval decreases rapidly in accordance to the decrease in the residence time of the ions at higher temperatures.

Table 6.2 Time interval between two configurations to enable 1 percent of mobile ions to be involved in string-like cooperative motion.

Temperature (*K*)	Time (*ps*)
2100	21.0
2200	5.0
2300	1.5
2400	0.8
2500	0.4
2600	0.3
2700	0.2

It is of interest to study the dimensionality or directionality of the ion jumps involved in a cooperative event. The ions that participate in the caterpillar model of Yokota [117] have a jump-directionality of 1, because all the ions of any particular caterpillar will jump in the same direction. The directionality of strings observed in the current work is evaluated using the following expression:

$$< \cos\theta >= \frac{\sum_{\text{for all strings}} \left(\sum_{i=1}^{n} \sum_{j>i}^{n} \hat{X}_i . \hat{X}_j \right)}{\sum_{\text{for all strings}} \left(\frac{n(n-1)}{2} \right)} \qquad (6.1)$$

Here X_1, X_2, .. X_n are vectors specifying the jump direction of all the n ions involved in any particular string; for example, X_i can be pointed in the <1 1 0> direction. $\hat{X}_i$ in Equation 6.1 represents the associated unit vector and the factor $n(n\text{-}1)/2$ in the denominator accounts for the possible number of pair-combinations (double summation) for a string of length n in the numerator. For the caterpillar mechanism, in which all the ions jump in the same direction, the dimensionality metric $< \cos\theta >$ is exactly 1. The vectors are normalized to unit magnitude to emphasize that fact that it is the direction of vectors, and not their magnitudes that are of importance in the evaluation of dimensionality of the string; further, this choice makes the value of $< \cos\theta >$ for caterpillar-like motion to be 1 in any direction. It can be verified that for

completely random jump directions the metric $<\cos\theta>$ is identically zero. Figure 6.6 shows $<\cos\theta>$ for the strings observed for time-intervals (Δt) of 0.2 and 1.0 *ps*, respectively, at various temperatures for oxygen ions in UO_2.

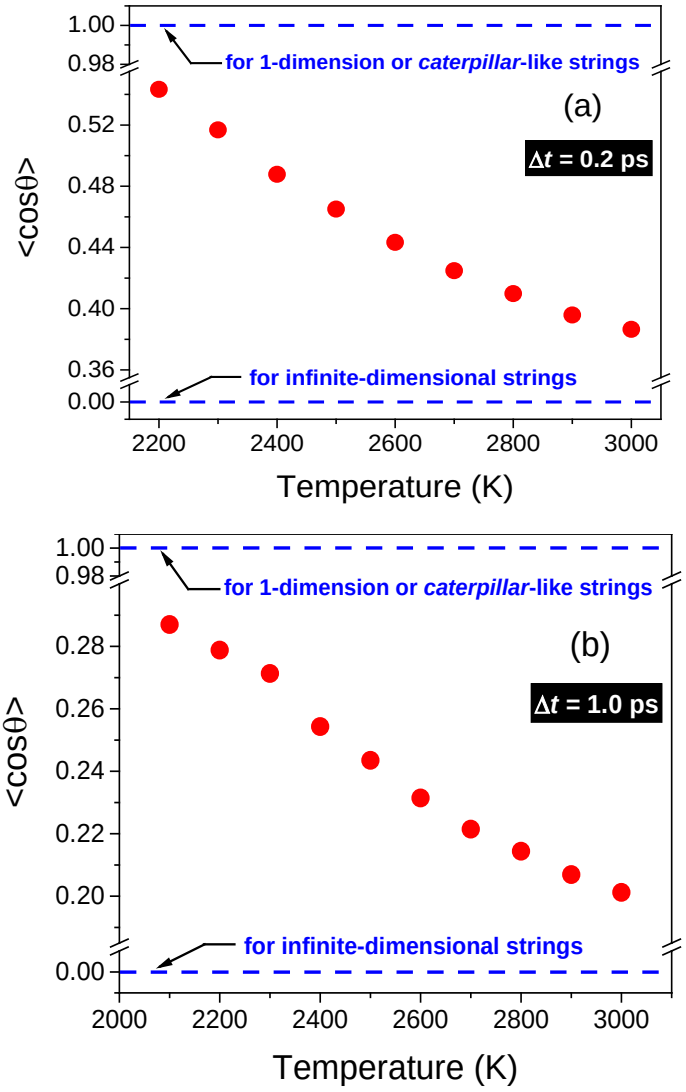

Figure 6.6 Dimensionality of the strings among oxygen ions in UO_2 for two values of Δt: (*a*) 0.2 and (*b*) 1.0 *ps*, in UO_2. The dimensionality decreases with temperatures although it exceeds the value corresponding to random displacements.

Although the strings generated in the simulations are far from caterpillar-like, they still show positive values of $<\cos\theta>$ indicating directionality in their character. The increase in the randomness of the jump directions at higher temperatures, for the same time-interval, arises from the higher probability of forming longer strings at these temperatures. Strings of the same length have similar directionalities (*i.e.* $<\cos\theta>$) at different temperatures, although with increasing temperature, longer strings are manifested that have more randomness in their direction. Since longer strings are observed for larger time-intervals, $<\cos\theta>$ will decrease for all temperatures with increasing Δt (compare Figure 6.6(*a*) and (*b*)). The manifestation of string-like motion and the positive directionality is a key observation for Type II superionics; this establishes that high diffusivities in superionics at temperatures above T_α can be attributed to collective string-like hopping motion of the ions.

6.3.2 TAD simulations

At temperatures much less than T_α atomistic simulations become prohibitively expensive. As discussed before, TAD simulations, therefore, have been performed to investigate the diffusive motion of an anion vacancy in both UO_2 and CaF_2 at temperatures less than T_α. As mentioned previously, TAD requires specification of both the system temperature (T_{low}) and a higher temperature (T_{high}); For UO_2, T_{high} is chosen to be 1500 *K*, while a value of 1000 *K* is prescribed for CaF_2. The high temperatures are chosen such that they are below T_α. TAD also requires the specification of the threshold distance, which is chosen as $a/2$ – the distance between two adjacent anion sites. All the simulations have been performed with LAMMPS using a lattice corresponding to 0 *K*. [122]; other inputs for the simulations are *delta* = 0.001 and *tmax* = 0.5 (with time in units of pico-second). TAD generates and identifies the most probable state-to-state configurations (positions of ions) of the system. The final results, as depicted in Figure 6.7, show that the defect (vacancy) migrates several atomic distances through a low-

dimensional string-like motion. The ionic displacements typically span three dimensions but the topologically constrained displacements are clearly evident from Figure 6.7. String-like cooperative motion is also observed in CaF_2 simulations as shown in Figure 6.8. As in UO_2, the anions in CaF_2 are observed to exhibit topologically constrained displacements reminiscent of dislocation in metals.

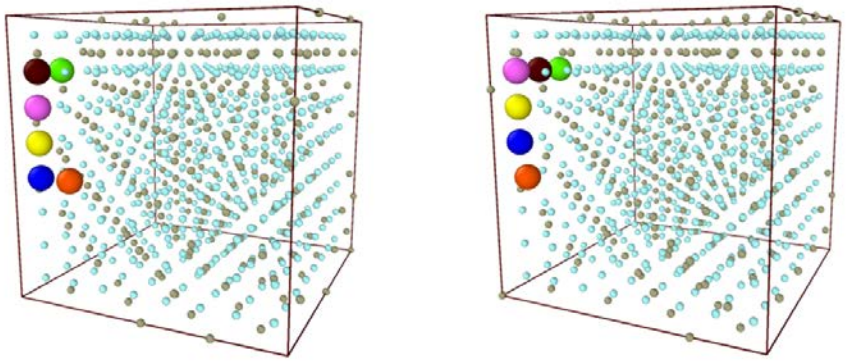

Figure 6.7 Observation of string-like cooperative motion at 300 *K* in UO_2 using TAD simulations. T_{high} is chosen as 1500 *K*. Ions participating in the string motion are shown bigger in size and in multiple colors.

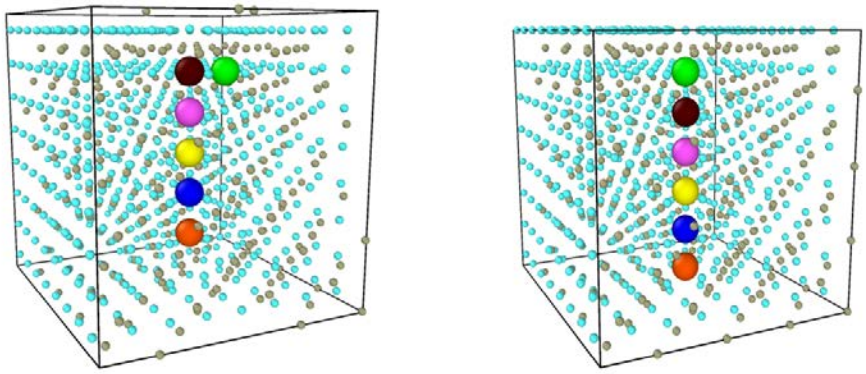

Figure 6.8 String motion observed in CaF_2 at 300 *K* using temperature accelerated dynamics.

6.4 Conclusions

String-like displacements are ubiquitous in kinematically jammed systems; such low dimensional displacements are known to dominate near the Mode Coupling Transition (MCT) temperature (T_c) in supercooled liquids [100]. In this chapter, it is established that string-like displacements exist in Type II superionic conductors too. Atomistic simulations at temperatures above T_α for both UO_2 and CaF_2 show low-dimensional topologically constrained string-like ionic displacements. The ion jumps involved in the strings are also found to have positive-directionality, rather than random directions; this observation can likely explain the high ionic conductivities/diffusivities at high temperatures. Remarkably, the probability of finding a string of length n shows an exponential distribution at temperatures above T_α – a variation that is typically shared by supercooled liquids and jammed states, in general. Interestingly, string-like ionic displacements are also observed below T_α using temperature accelerated dynamics (TAD). Based on the TAD and atomistic results for CaF_2 and UO_2, it is conjectured that hopping between native lattice sites, and topologically constrained low dimensional string-like motion are characteristic features in all Type II superionic conductors at all temperatures.

Chapter 7: DYNAMICAL RECOVERY IN UO_2 FOLLOWING RADIATION

7.1 Introduction

Fluorite-structured UO_2 is the quintessential nuclear fuel in nuclear reactors. During reactor operation, the nuclear fuel is subjected to various kinds of radiation all of which degrade the crystalline structure of the fuel. As discussed earlier, the oxygen anions arrange themselves in a simple-cubic lattice with the uranium cations occupying alternate cube centers (also known as the tetrahedral sites). It is inferred from experiments that at temperatures well below T_α, the dominant defects are anion Frenkel pairs, with the interstitial ions mostly occupying the octahedral sites, the unoccupied cube centers of the fluorite structure [7].

UO_2 is known to be tolerant against amorphization when subjected to intense nuclear radiations that are generated during the fission and decay processes inside the fuel. Sickafus and co-workers have demonstrated the ability of fluorite structures to accommodate disorder by virtue of low defect formation energies, thereby avoiding lattice instability and amorphization [25]. Further, it is observed that compounds with natural atomic disordering tendencies or, equivalently, having low order-disorder (O-D) transformation energies, are associated with better resistance to amorphization [26]. While several atomistic simulations on radiation response of UO_2 have been reported, none have investigated the superionic characteristics of UO_2 such as correlated dynamics and string-like ionic displacements. Thus the second part of this dissertation deals with non-equilibrium displacement cascade

simulations of UO_2 with the objective to analyze the short-time dynamical response of UO_2 following radiation impacts.

7.2 Importance of dynamics in promoting tolerance to amorphization

UO_2 is a ceramic material and a number of investigations exist on the irradiation-induced crystalline-to-amorphous transformation in ceramics [124-126]. Amorphization in ceramics is observed to occur either homogeneously or heterogeneously [125]. In a recent work, Jiang *et al.* have investigated two ceramics silicon carbide (SiC) and zirconium carbide (ZrC) that are known to have contrasting response to irradiation [126]. Both SiC and ZrC have similar structures containing two interpenetrating face centered cubic (FCC) sublattices. SiC, having applications in nuclear systems, amorphizes beyond a certain irradiation dose when exposed below a critical temperature [127], whereas ZrC is highly resistant to amorphization under irradiation. The intrinsic mechanical instability of the silicon sublattice, as reckoned from the imaginary phonon frequencies, with respect to displacements on carbon sublattice has been proposed as the principal reason for the susceptibility of silicon carbide to amorphize under irradiation [126]. On the other hand, zirconium lattice in zirconium carbide, another ceramic material that has potential applications in nuclear industry, is revealed to be mechanically stable with respect to a highly defective carbon (C) sublattice generated under irradiation [126]. This investigation indicates that the native vibratory dynamics, as inferred through phonon dispersion curves, plays a crucial role in determining whether a material possesses amorphization tolerant properties.

7.3 Native dynamics of UO_2 in equilibrium

It has been discussed in Chapter 3 that an order-disorder transition occurs in all Type II superionic conductors [84]. Beyond a characteristic temperature (T_α), the anions become disordered and mobile contributing to most of the observed high ionic conductivity; the cation sublattice on the other hand maintains its crystalline structure until melting. Dynamically, the disorder manifests itself as a diffusion process wherein the anions typically hop between native anion sites, as evidenced from incoherent quasi-elastic scattering studies [128].

Atomistic simulations show that oxygen ions in UO_2 intermittently jump from one site to the neighboring sites in the superionic state [29]; string-like motion described in the earlier chapter is a manifestation of a correlated and simultaneous hopping process. Most of the jumps take place along the <100> direction separated by a distance of *a*/2, but a fraction of the oxygen ions also jump along the <110> and <111> directions. Figure 7.1(*a*) depicts the hopping motion of oxygen ions obtained from equilibrium atomistic simulations along the <100> direction; this characteristic motion is different from that in typical liquids. On an average, the oxygen ions have a prolonged sojourn at their native sites, vibrating back and forth, before making a jump to a neighboring site. Hopping motion along <110> and <111> directions are also illustrated in Figure 7.1(*b*). At 3000 *K*, it is estimated that 84% of oxygen ions hop between the nearest neighbor positions (along <100> direction), and 13% and 3% of the oxygen ions along the <110> and <111> directions, respectively. These values are in reasonable agreement with an earlier study of CaF_2 indicating 79% of the fluorine ions hopping along <100> direction, with the remaining 21% among the sites along the <110> direction [129]. One of the objectives of this dissertation is to investigate whether the dynamics exhibited by oxygen ions in equilibrium, *i.e*. the native hopping motion and the string-like cooperative behavior, is also manifested during a non-equilibrium displacement cascade simulation that

mimics a perturbation from radiation impacts, and whether the native dynamics plays a role in the defect recovery following radiation.

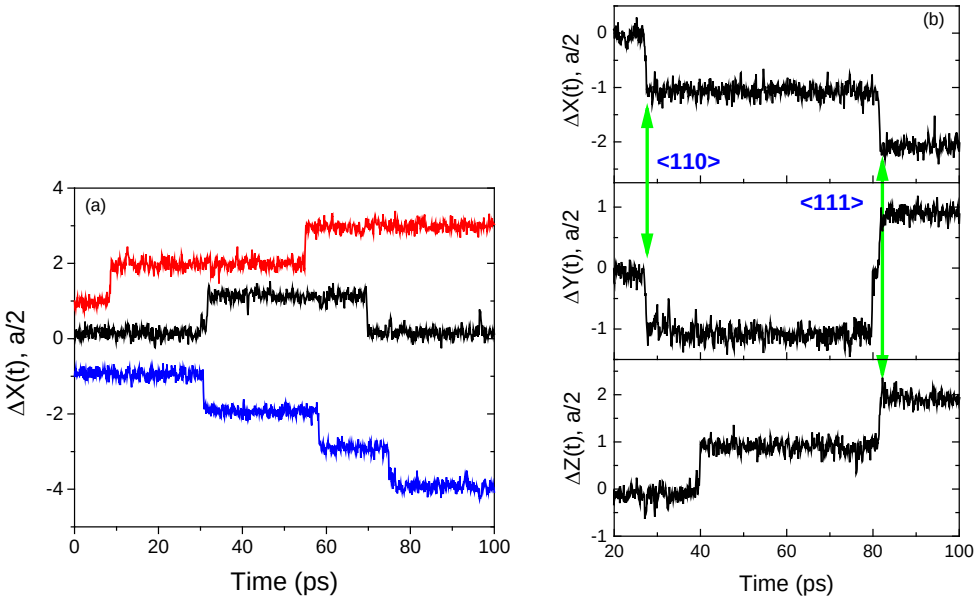

Figure 7.1 (*a*) Three trajectories of oxygen ions depicting hopping motion along <100> direction at 2500 *K*. The first and third ion displacements (shown in red and blue) have been shifted by (*a*/2) and (-*a*/2), respectively, for clarity. Note that hopping of one ion is also often accompanied by a simultaneous hopping of another ion; this characteristic feature manifests as simultaneous peaks in $G_s(r,t)$ described in Chapter 4. (*b*) Hopping along <110> and <111> directions.

7.4 Displacement cascade atomistic simulations

In the past, atomistic simulations of displacement cascades in UO_2 have mainly been devoted to quantifying both simple and complex defect structures [130, 131]. The primary objective of the current work, as stated before, is to analyze the dynamical recovery of oxygen ions following radiation impacts, and to inspect whether the superionic characteristics of UO_2 are profitable in the dynamical recovery process. The details of equilibrium atomistic simulations

of UO_2 have been discussed in Section 3.3; the displacement cascade simulations also use the same potential, however, augmented by a screened Columbic potential at close distances. The "universal" ZBL potential [42], a screened Coulombic repulsive potential between the nuclei, is applied for distances less than 1 Å and this potential is joined smoothly by a Fermi function [132] to the equilibrium pair-potential of Yakub *et al.* [39]; the construction of the potentials has been described in Chapter 2. The ions are initially arranged on a crystalline fluorite lattice and each ion is assigned an initial velocity based on a Maxwell-Boltzmann distribution centered at 300 *K*. Next, the system is allowed to attain equilibrium by maintaining the simulation cell at 300 *K* for several picoseconds at zero pressure. Non-equilibrium displacement cascades are then initiated by imparting excess momentum and energy to an ion, usually designated as the primary knock-on atom (PKA), situated at the center of the simulation box. A uranium ion is chosen as the PKA in all the simulations; statistically averaged dynamical results do not change if an oxygen ion is knocked instead. The PKA can be considered to act like a recoil nucleus after undergoing an α-decay, which subsequently creates a 'cascade' of secondary displacements of neighboring ions.

All the simulations are carried out on a cubic UO_2 single crystal containing 96,000 to 165,888 ions; the chosen size is such that the PKA remains inside the simulation cell for energies up to 10 *keV*. A previous study has shown that the initial PKA direction has negligible effect on the final defect state in UO_2 [130]; hence the simulations in the current work has been restricted to one direction (along <100>). Thermostats are places at the edges of the simulation cell to absorb the shock generated from the PKA impact. The response of the system following radiation is monitored for approximately 6 *ps*; during this period, pertinent variables such as thermodynamic properties, defects, and time resolved correlation functions are collected.

To identify the defects, we compare configuration of the evolving system with the initial zero-defect structure. A lattice site is considered a vacancy if it does not contain an atom within a sphere of radius 1 Å, centered on the site. Similarly, an atom is considered an interstitial if it is inside a similar sphere centered on an interstitial site. A total of 130 independent runs are performed, deemed sufficient for good statistics, and all the results are averaged over the independent runs. It has been shown recently that the irradiation spectrum plays a very important role in determining the radiation tolerance of pyrochlores, a close variant of fluorite-structured oxides, by demonstrating the titanate pyrochlores as characterized by either poor radiation tolerance or robust behavior depending on the energy of the PKA [133]. Keeping this in mind and seeking to examine our results at higher PKA energies, we have done additional 10 *keV* displacement cascade simulations on a 24×24×24 UO_2 system having 165,888 ions. A total of 80 independent runs are performed in this case. The results obtained, as will be shown, are in very good agreement with the 2 *keV* simulations.

7.5 Results

7.5.1 Variation of defects

In Figure 7.2(*a*), the time variation of the instantaneous number of point defects, arising from the displacement cascade, for both uranium and oxygen ions, are shown. An ion is considered a defect if it does not belong to any lattice site within a specified cut-off distance (chosen as 1 Å in this study); anti-site defects are also considered when ions switch positions. The well-known, two-stage behavior of cascade defect evolution can be observed in Figure 7.2, with the number of defects peaking initially (ballistic stage) followed by the defect recovery stage. The inherent or native stability of UO_2 structure against a dynamic perturbation is quite evident from the high rate of instantaneous defect recovery; the residual number of defects after just a

few picoseconds is a small fraction of the total number of defects at the end of ballistic stage. These results are also in agreement with an earlier simulation study that showed the inability of Frenkel pairs to stabilize in UO_2 [24]. Further, no anti-site defects were observed at the end of the simulations, terminated at 6 *ps*, approximately.

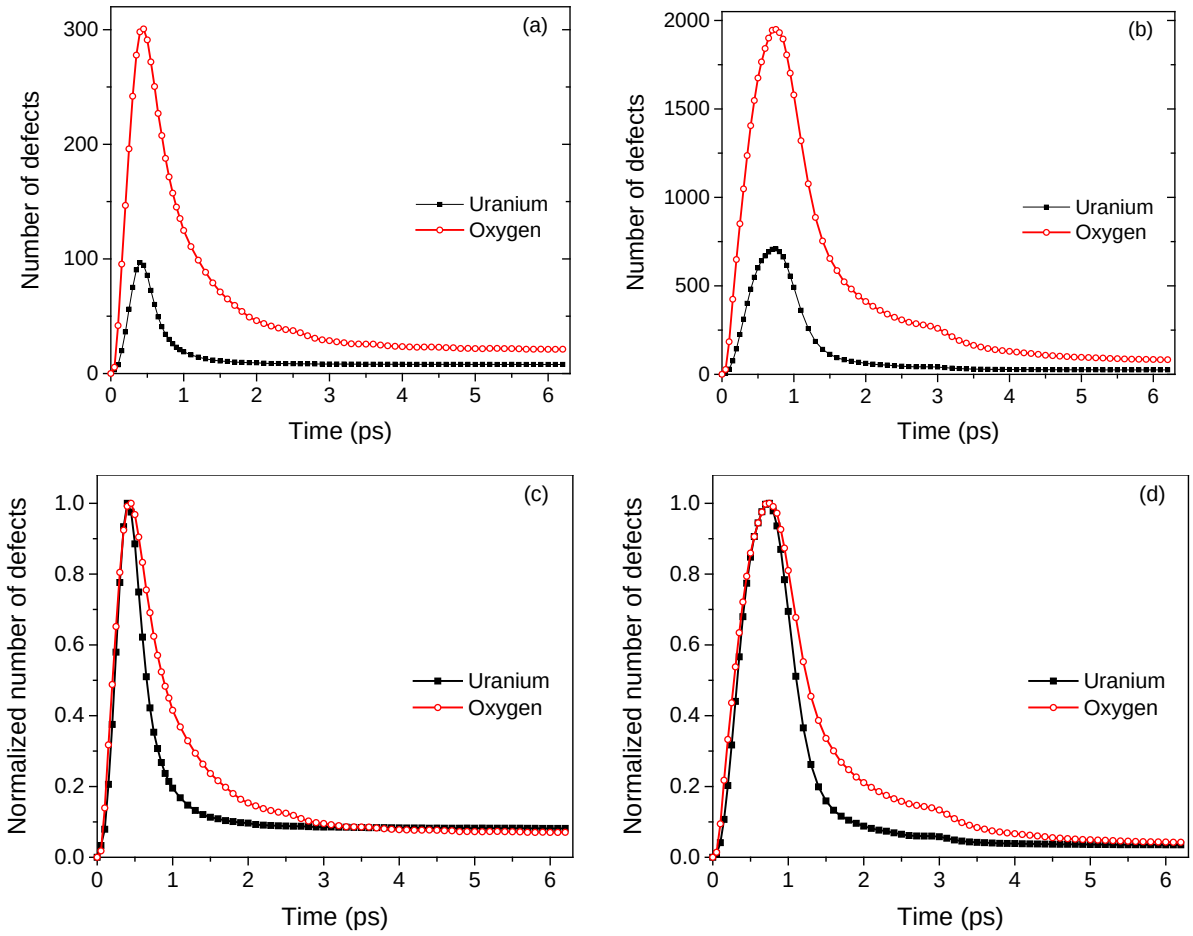

Figure 7.2 (*a*) Temporal variation of transient defects for a 2 *keV* knock, initiated at $t = 0$, in UO_2 at 300 *K*. The number of defects shows a maximum at 0.5 *ps*, approximately. (*b*) Temporal variation for a 10 *keV* knock. (*c*) and (*d*) show the variation of normalized number of defects for 2 *keV* and 10 *keV* simulations, respectively.

Analogous results can be observed for 10 *keV* simulations from Figure 7.2(*b*). The variation of defects, normalized to their peak values, is shown in Figure 7.2(*c*) and (*d*). It is clear that oxygen and uranium defects peak around the same time and their decay also follows a similar pattern; hence, the defects have a similar dynamics though their behavior is vastly different.

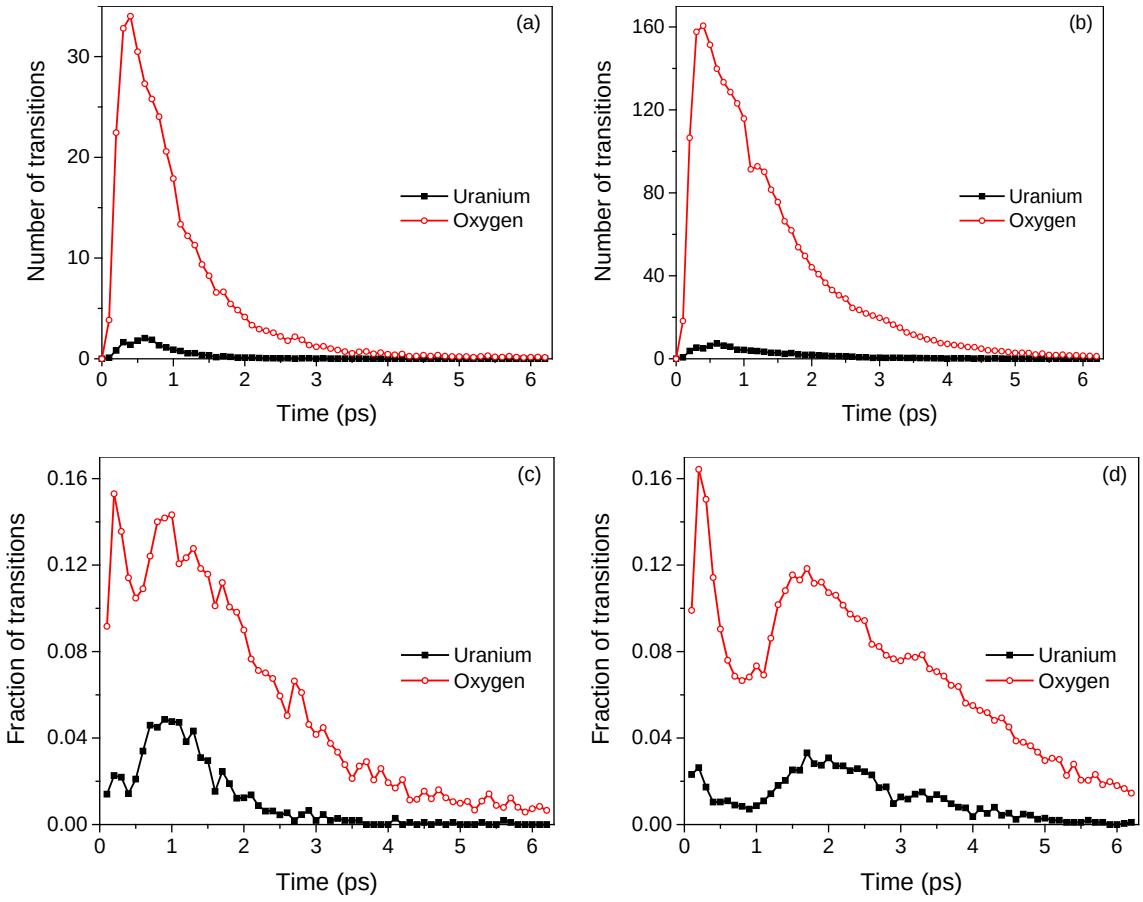

Figure 7.3 (*a*) Temporal variation of the number of replacement transitions of uranium and oxygen ions to identical neighboring sites for 2 *keV* and (*b*) 10 *keV* radiation knock. (*c*) and (*d*) depict the time variation of the ratio of number of transitions to number of defects for 2 *keV* and 10 *keV* simulations, respectively.

In the case of uranium ions, the rapid rise and fall in the number of defects is mainly attributed to the ions initially displaced by the cascade, thereby becoming interstitials, and later reverting

to their original sites. Only a few uranium defects jump to a new cation site to get annihilated. The situation is completely different for oxygen ions. A significant number of anion defects are annihilated by means of making transitions to neighboring lattice sites. This is evident from Figure 7.3(*a*), which shows the temporal variation (during an interval of 0.1 *ps*) of number of replacement transitions made by uranium and oxygen ions. The fraction of existing defects that are annealed by replacement transitions is shown in Figure 7.3(*c*); this is calculated as the ratio of number of replacement transitions to number of defects. A higher fraction of oxygen ions are clearly seen to make a transition to annihilate, while only a few of the uranium ions undergo jump to a neighboring site. Analogous results can be observed for 10 *keV* simulations from Figure 7.3(*b*) and (*d*). Thus, the uranium ions are mostly immobile upon a radiation knock. In the subsequent sections, the main focus will be on the motion of oxygen ions, which are more mobile thermally and following a radiation perturbation.

7.5.2. van Hove self-correlation function

Previously in Section 4.3, the self-part of van Hove correlation function, introduced in Section 2.5.1, was employed for identifying ionic jumps and heterogeneous dynamics among oxygen ions in in UO_2 at temperatures above T_α. For a system of N ions, $G_s(r,t)$ is given by the expression [57]:

$$G_s(r,t) \equiv \left\langle \frac{1}{N} \sum_{i=1}^{N} \delta\left(r - \left|\boldsymbol{r}_i(t) - \boldsymbol{r}_i(0)\right|\right) \right\rangle \tag{7.1}$$

Equation 7.1 specifies the average displacement of a particle and as shown before it is a useful metric to analyze the temporal motion of ions. Under equilibrium conditions, $G_s(r,t)$ assumes a Gaussian shape at large times; in non-equilibrium or jammed conditions, however, the tail of the $G_s(r,t)$ is seen to portray an exponential behavior. For an isotropic system, $4\pi r^2 G_s(r,t)$

represents the probability that an ion has displaced a distance *r* around *dr* during a time-interval *t*. This isotropic metric is employed to uncover the oxygen ion dynamics following a radiation knock. Figure 7.4 depicts evolution of time-averaged $G_s(r,t)$ following a radiation knock for two knock energies, 2 *keV* and 10 *keV*, respectively. At small times following the radiation knock (0.2 *ps*), the tail of distribution deviates considerably from that of the equilibrium distribution (also shown in the figure at 300 *K*). As observed in high temperature equilibrium simulations (see Section 4.3), the tail depicts prominent peaks at longer times indicating that ions are cooperatively jumping from one lattice site to another. Not surprisingly, the peak positions correspond to the nearest neighbor locations of the oxygen ions in the equilibrium state as shown by the radiation distribution function at 300 *K*. Since the peaks denote a diffusional hopping process, described earlier in Section 4.3 and in [98], it is concluded that oxygen transient defects annihilate by engaging in *collective* jumps to neighboring sites. It is further seen that as the PKA energy increases, the cooperative motion becomes more intense as exemplified by 4 peaks with 10 *keV*, which is double the value observed for 2 *keV*.

The time-resolved variation of $4\pi r^2 G_s(r,t)$ shows that anion motion following a radiation perturbation is very similar to what is observed in UO_2 at temperature above T_α. To check whether the excess thermal energies are responsible for the cooperative jumps, the instantaneous temperature along a plane at the center of the system, with the PKA directed from left to right, is depicted in Figure 7.5 for 2 *keV* and 10 *keV*, respectively. The high local temperatures near the disordered region confirm that the excess thermal energy lays the platform for the anions to undergo collective hopping from one site to another.

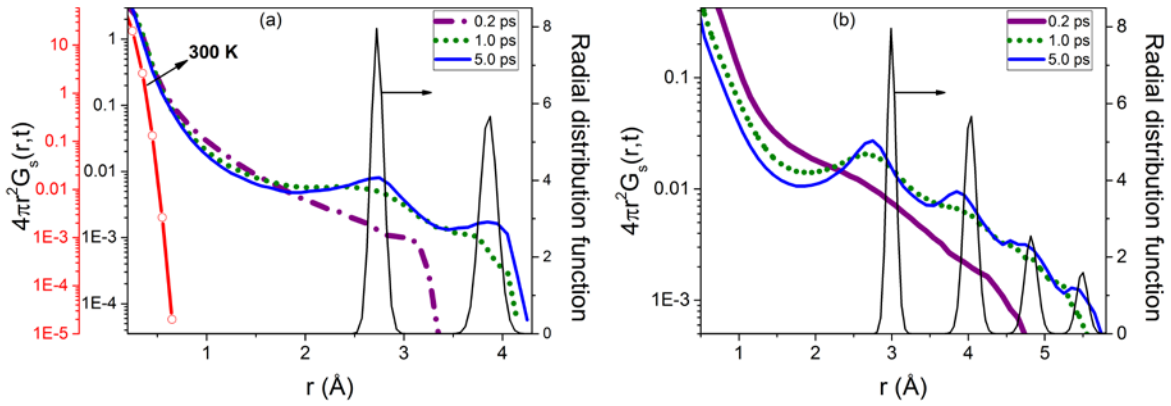

Figure 7.4 Time-resolved isotropic *van Hove* self-correlation function for oxygen ions at different times following radiation impact, with a knock energy of (*a*) 2 *keV*, and (*b*) 10 *keV* at 300 *K*. The radial distribution function (RDF) of oxygen ions at 300 *K* is also shown; the two peaks in RDF correspond to the nearest <100> and <110> lattice spacing. For comparison, $4\pi r^2 G_s(r,t)$ for oxygen ions in equilibrium simulation at 300 *K* is also shown in the left panel (corresponding to the *y*-axis shown in red).

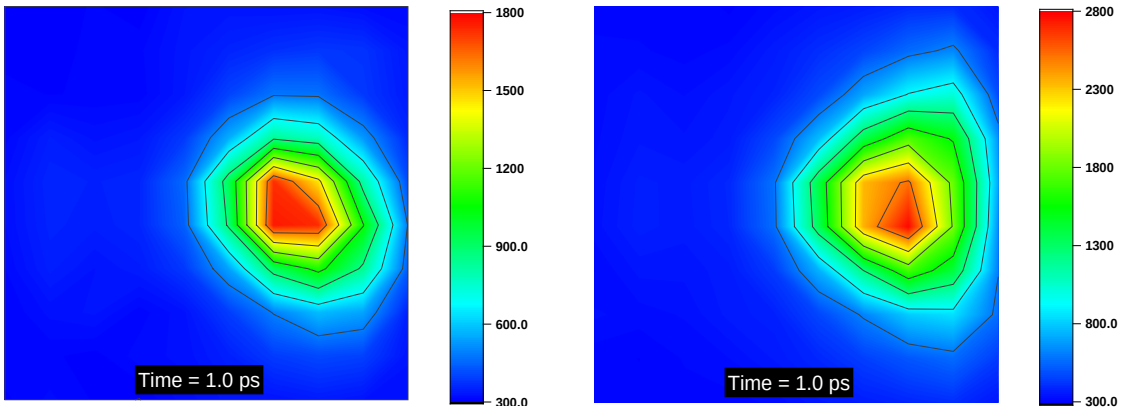

(a) **(b)**

Figure 7.5 Temperature contours (in Kelvin) along a plane at the center of the simulation box, with the initial PKA starting at the center of the plane and directed from left to right, for (*a*) 2 *keV* and (*b*) 10 *keV* cascade simulations. Both the contours demonstrate very high temperatures at the disordered regions that assist in the observed hopping motion of oxygen ions.

7.5.3. String-like cooperative motion

The peaks in the tail of $G_s(r,t)$ indicate that ions hop from one native site to another simultaneously. As delineated in Chapter 6, the ions are displaced in a string-like fashion when multiple peaks are observed in $G_s(r,t)$. In the string-like cooperative motion, which involves *sequential* jumps of more than one ion to neighboring lattice sites, each ion supplants the next ion in a pseudo-one dimensional string-like fashion, culminating with the last ion jumping into a vacant site or into a site by pushing the existing ion into an interstitial position (hence, no further simultaneous transition is possible from this site to a neighboring lattice position).

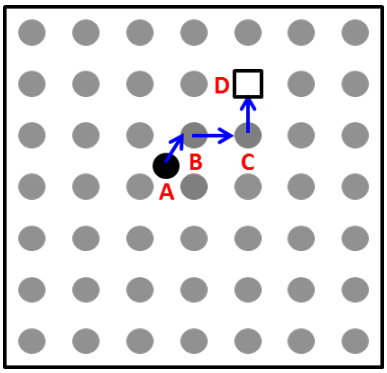

Figure 7.6 A sample 2-dimensional lattice with an interstitial and a vacancy. The site *A* is an interstitial position while *B*, *C* and *D* are lattice sites. The atoms at *A*, *B* and *C* make sequential jumps and, after the transition, will be at *B*, *C* and *D*, respectively.

Figure 7.6 shows three ions performing string-like correlated motion in which every ion replaces the next ion in the string. The jump of the ions could be in any direction in three-dimensional space during the simulations. An ion making a transition between two lattice sites, say, *A* to *B*, could be staying in an interstitial position for any amount of time after leaving site *A*, and before entering site *B*. However, all the transitions to new sites must occur within a small timeframe to be considered as a string-like sequential motion. In this work, the presence

of strings are probed every 0.05 *ps* intervals during the first pico-second following the PKA knock, and then at every 0.1 *ps* intervals for the rest of the simulation.

As described earlier, Frenkel-pair is the dominant defect type following a radiation knock. The Frenkel-pairs usually get annihilated by means of simple vacancy-interstitial recombination. In this process, a vacancy has to migrate to a site adjoining an interstitial or/and an interstitial jumps towards a vacancy thereby both getting annihilated eventually. The whole process involves several independent steps, if the vacancy and interstitial are initially far apart. Figure 7.7 depicts this mechanism in a two-dimensional system.

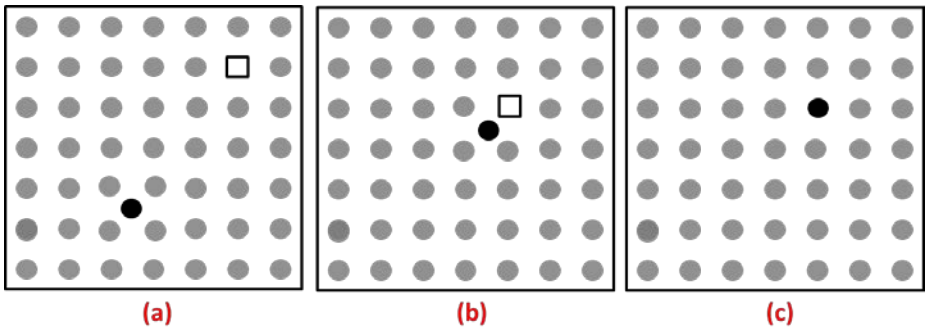

Figure 7.7 A vacancy-interstitial recombination. (*a*) A well-separated vacancy and an interstitial. (*b*) Vacancy and interstitial moving closer to each other. (*c*) Vacancy-interstitial annihilation.

However, during a string-like motion, an ion jumps not only to a vacant neighboring site but also induces the ion on the latter site to make a jump to another neighboring lattice site. Performed this way, an interstitial can recombine with a vacancy several steps away much faster and efficiently using fewer number of steps, than it would be possible by simple vacancy-interstitial recombination. Figure 7.8 shows an example of cooperative sequential motion exhibited by oxygen ions observed during an MD simulation, where the initial defects are annihilated at the end of the transition.

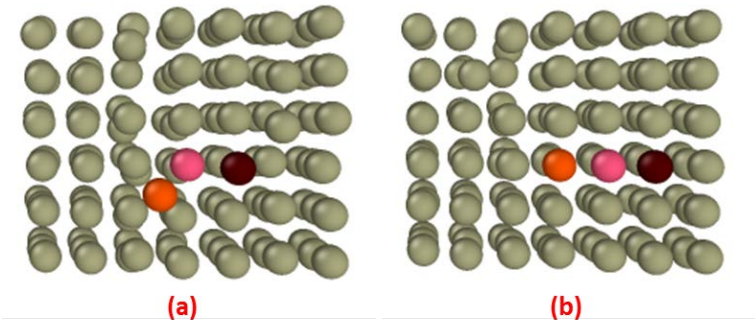

Figure 7.8 An example of cooperative motion among oxygen ions during cascade simulations of UO_2 – (*a*) and (*b*) represent snapshots of the system at two successive time intervals. Both the octahedral interstitial and the vacancy, which are three steps apart, get annihilated by means of string-like correlated jumps. The configurations are shown using OVITO [134].

7.5.4. Kinetics of string-like motion in cascade simulations

As noted previously, an ion belongs to a lattice site if it is inside a sphere of radius 1 Å centered on the site. For the ion in Figure 7.6 making a transition between lattice sites *B* and *C* (from *B* to *C*): if t_1 is the most recent time the ion belonged to *B* and t_2 is the time when it first belongs to *C*, the lifetime of ion involved in this transition is (t_2-t_1). This lifetime indicates the time period an ion has spent at the interstices of the lattice before making a transition, with longer lifetimes corresponding to a longer sojourn at an interstitial site (as a defect). The length of the string (n) is defined as the number of ions involved in cooperative motion; e.g. the string in Figure 7.6 has n = 3. In the current simulations, most of the strings (approximately, 90%) correspond to n = 2 while strings involving as many as 6 ions have been observed following a radiation knock.

The probability distribution of the length of string, $P(n)$, is shown in Figure 7.9(*a*) and (*b*) for 2 *keV* and 10 *keV* simulations, respectively. As observed in equilibrium simulations discussed in Chapter 6, the string distribution is exponential following a radiation knock.

Similar exponential variation has also been associated with the strings observed in equilibrium simulations of glass-forming supercooled investigations [15].

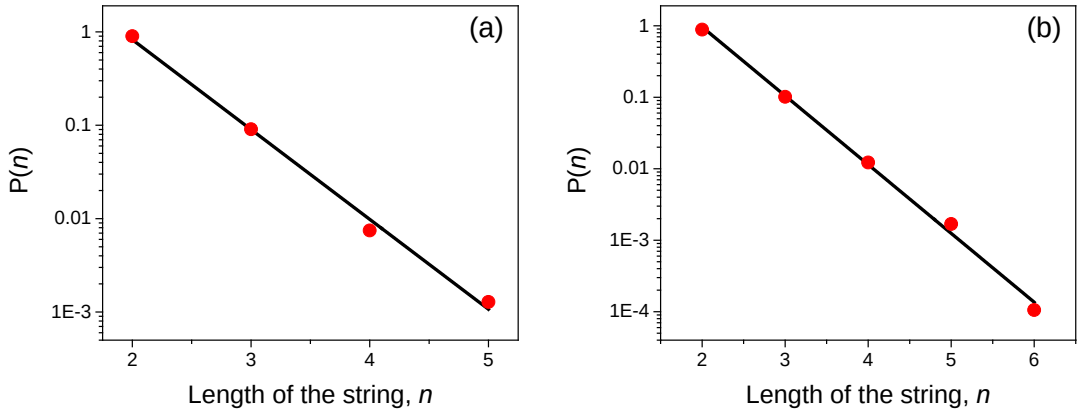

Figure 7.9 Probability distribution of length of the strings observed following (*a*) 2 *keV* and (*b*) 10 *keV* radiation knocks.

Next the role of the string initiator ion is discussed. In Figure 7.6, the first ion making a transition from *A* to *B* is termed as the "initiator" of string. Even though every string has two ions at its edges (for $n = 2$, both ions involved are at the edges), only the initiator ion replaces next ion in the string during a cooperative string-like motion. Hence, there is a unique initiator ion for any chosen string. The rest of the ions participating in the string motion are simply termed as "participants." In this work, it is shown that the string-like cooperative motion is mostly *initiated* by oxygen ions that have long been displaced from their actual positions to interstitial sites, *i.e.* an *initiator* ion in any particular string has, on an average, longer lifetime compared to that of the *participant* ions.

Figure 7.10, depicts the probability histograms of lifetime of all ions, divided into two groups – initiators and participants, involved in cooperative string-like motion following a 2 *keV* knock. The histograms are normalized with the number of ions in their respective groups. Figure 7.10 clearly indicate that participant ions in the string have preference towards shorter

lifetimes while the initiator ions have higher probabilities than participant ions at longer lifetimes. The ratio ($\tau_{i\text{-}n}$) for of initiator group lifetime to that of participant ions is evaluated to be 1.92. Thus, the initiator ions have, on an average, almost twice the lifetime compared to that of the participant ions in the string. This indicates that string-like cooperative motion is initiated by oxygen ions that are displaced for a longer time.

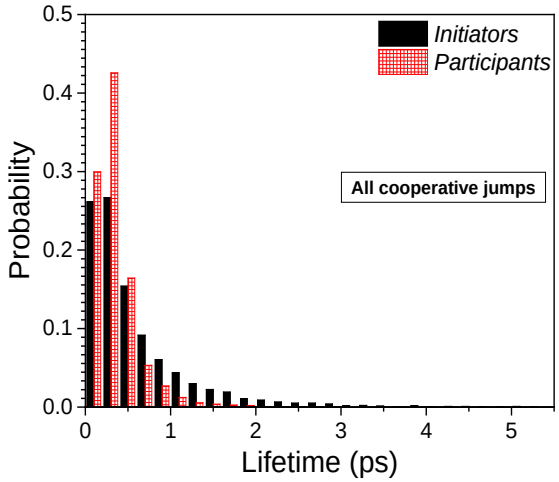

Figure 7.10 Lifetime probability histogram for initiator and participants ions that participate in string-like correlated motion. The average initiator ions lifetime is almost twice that of participant ions lifetime.

More compelling evidence that initiator ions of cooperative motion are the long-lived defects can be obtained if only the cooperative jumps starting from a time subsequent to the ballistic phase is considered. In this work, strings are observed for two initial starting times: after t = 0.5 *ps*, and t = 1.0 *ps*. In both the cases, the cooperative jumps during the ballistic phase have been discarded; the resulting histograms are shown in Figure 7.11. The propensity for the participant ions to have shorter lifetimes is more pronounced now, so does the tendency of the initiator ions to have longer lifetimes. The ratio of initiator group lifetime to that of participant group lifetime ($\tau_{i\text{-}n}$) is 2.07 and 2.54, for the two cases, respectively.

Table 7.1 illustrates $\tau_{i\text{-}n}$ for different starting times. It can be noted that the average lifetime of the initiator ions is almost seven times compared with that of the participant ions, if a starting time of 5 *ps* is considered. From Figure 7.10, Figure 7.11 and Table 7.1, it is quite clear that cooperative string-like motion is mostly *initiated* by long-lived oxygen ions.

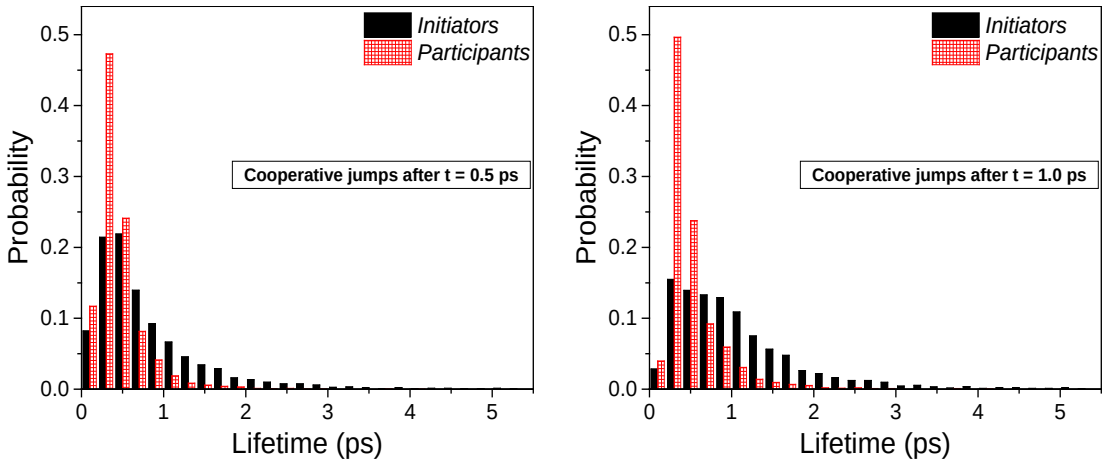

Figure 7.11 Lifetime probability histogram for oxygen ions involved in cooperative string-like jumps that occur with starting times (*a*) t = 0.5 *ps* and (*b*) t = 1.0 *ps*.

Table 7.1 The lifetimes of initiator ions, normalized to the participant ion lifetimes for various starting times with 2 *keV* radiation knock.

Starting time (*ps*)	Ratio of *initiator* group to *participant* group lifetimes, $\tau_{i\text{-}n}$
0	1.92
0.5	2.07
1.0	2.54
1.5	3.30
2.0	4.27
2.5	5.07
3.0	5.66
3.5	6.78

Similar results are observed for the case of 10 *keV* displacement cascade simulations. Figure 7.12 and Table 7.2 depict these results.

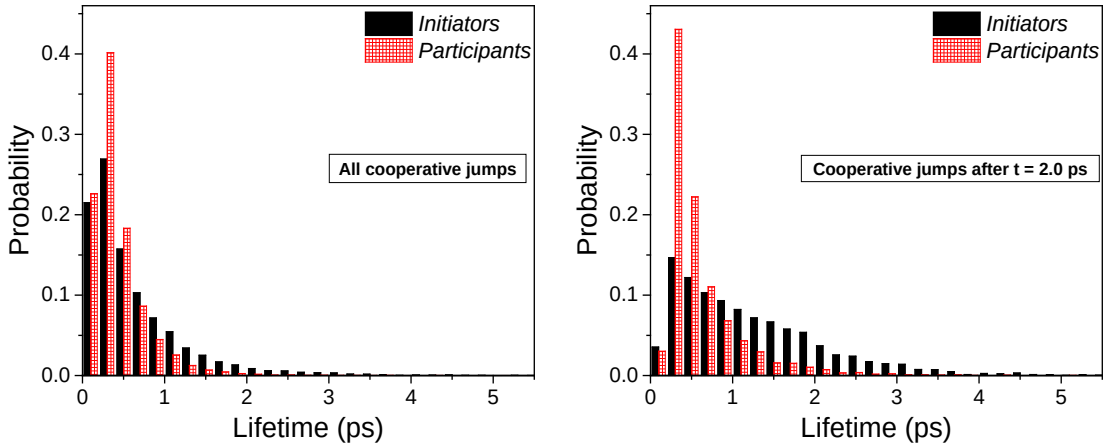

Figure 7.12 Lifetime probability histogram for ions participating in string-like cooperative motion for a 10 *keV* knock with starting times (*a*) t = 0 *ps* and (*b*) t = 2.0 *ps*.

Table 7.2 Results for 10 *keV* cascade simulations. In this case, longer starting times, compared to 2 *keV* case, are considered as the defect concentration saturates at a later time.

Starting time (*ps*)	Ratio of *initiator* group to *participant* group lifetimes, $\tau_{i\text{-}n}$
0	1.60
1.0	1.79
1.5	2.02
2.0	2.35
2.5	2.71
3.0	3.00
3.5	3.58
4.0	4.05
5.0	7.08

The analysis thus far has demonstrated that long-lived interstitial defects have a higher propensity to become initiator ions and subsequently undergo a string-like transport mechanism that annihilates an interstitial-vacancy pair. But what is fraction of interstitials

undergoes cooperative sequential motion? This fraction is identified by considering all the annihilated oxygen interstitials that have made replacement jumps onto neighboring oxygen sites and evaluating the fraction that initiates a string motion during their recovery. From Figure 7.13 several things are worth noting. First, it is observed that a quarter of the oxygen interstitials are annihilated by means of the string-like cooperative motion; the rest by the more ubiquitous vacancy-interstitial mechanism. Second, this fraction remain approximately constant for a range of lifetimes of the interstitials varied between 0.2 to 2 *ps*, and for both 2 *keV* and 10 *keV* knocks. The lifetime indicates the time period an ion has spent at the interstices of the lattice before recovery and is earlier defined. Note that the interstitials partaking in string motion above include both the initiator or participant ions of the string. However, as discussed before, the probability of an interstitial initiating a string increases with increase in lifetime of the interstitial; from the figure, it can be observed that the probability has increased from 10 to 23 percent by varying its lifetime from 0.2 *ps* to 2 *ps*. This result confirms the earlier observation that the longer the time an interstitial has been in a defective state, the higher the probability that it will be annihilated by initiating a correlated string-like transition. This may be a result of ions neighboring an interstitial arranging themselves to facilitate a cooperative event. Apparently, the probability of an interstitial being a participant of the string decreases with increasing lifetime. This explains why the probability of defects annihilated for different lifetimes remain largely unaltered for different life-times of the interstitial. From Figure 7.13, it is apparent that string-like correlated motion is an important mode of defect annihilation, especially for long-lived defects even though most of the recovery takes place by simple vacancy-interstitial combination.

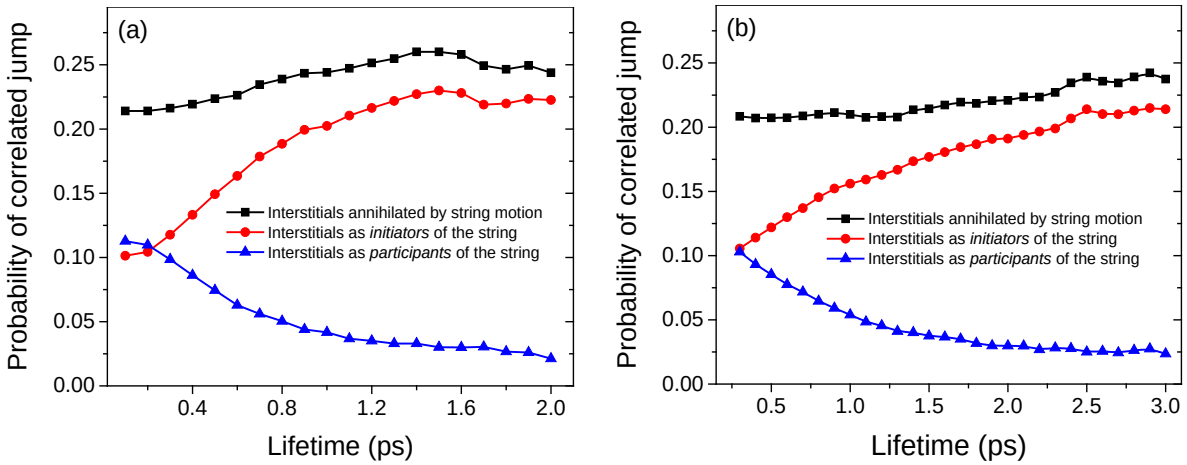

Figure 7.13 Probability of interstitials to get annihilated through a string-like transport mechanism, (*a*) 2 *keV* and (*b*) 10 *keV* knocks.

7.6 Validation using a different interatomic potential

It is known that interatomic potentials vary in their ability to make consistent prediction especially under out-of-equilibrium thermodynamic conditions. As discussed in Section 2.1.4, a competing potential by Basak *et al*. [40] also reproduces a variety of equilibrium properties and has been widely used for studying cascade simulations in UO_2 [77, 78]. The form of the potential is given in Equation 2.5, which is the same as for Yakub *et al*. potential, and the parameters are listed in Table 2.2. In Figure 7.14, the variation of number of defects is calculated using the new potential, and a good agreement with earlier calculations is shown. The other results obtained using Basak *et al.* potential are also in very good agreement with the results obtained from Yakub *et al*. potential.

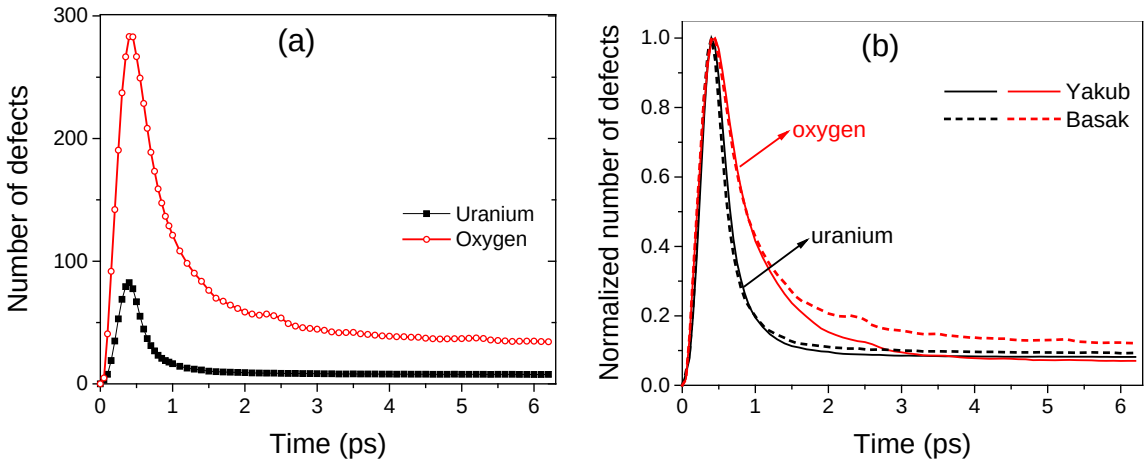

Figure 7.14 Comparison of Yakub *et al*. [39] and Basak *et al*. [40] potentials. (*a*) Time variation of number of defects from 2 *keV* cascade simulations using Basak *et al.* potential. (*b*) Contrasting the variation of defects from Yakub *et al.* and Basak *et al.* potential. Solid lines represent normalized defect variation obtained using Yakub *et al.* potential, for both uranium and oxygen ions, while dashed lines represent results using Basak *et al.* potential.

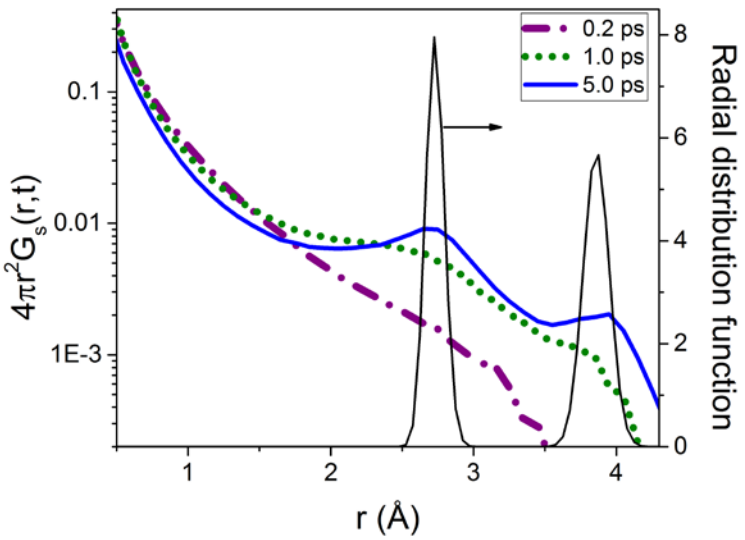

Figure 7.15 Temporal variation of $G_s(r,t)$ with Basak *et al*. potential [40]. The radial distribution function (RDF) of oxygen ions at 300 *K* is also shown, with the peaks of $G_s(r,t)$ at longer times matching with that of nearest neighbor distances obtained from RDF. $G_s(r,t)$ from Yakub *et al.* [39] and Basak *et al.* [40] potentials are nearly identical – see Figure 7.4.

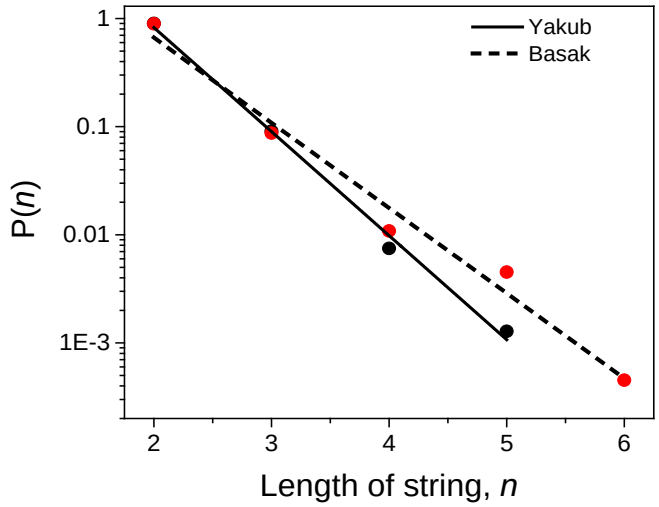

Figure 7.16 Comparison of probability distribution of string lengths with Yakub *et al*. [39] and Basak *et al*. [40] potentials for 2 *keV* knock.

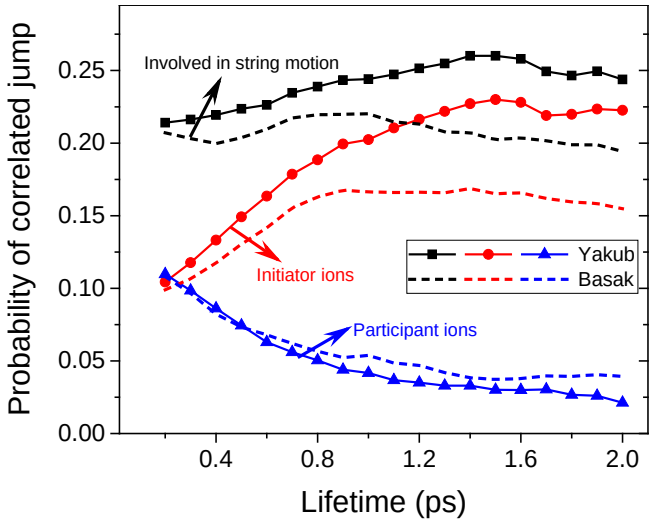

Figure 7.17 Comparison of the probability of getting an interstitial annihilated through string transport with Yakub *et al*. [39] and Basak *et al*. [40] potentials for 2 *keV* knock.

7.7 Conclusions

In this chapter, atomistic simulations have been performed to investigate the kinetic evolution of defects following a radiation knock in UO_2, with one cascade of displacements per

simulation without any overlaps. Fast dynamical recovery is observed with most of the defects getting annihilated within a few pico-seconds after the radiation-knock. The van Hove self-correlation function, $G_s(r,t)$, indicates that the displaced oxygen ions hop from one native site to another. The hopping of ions indicate but does not conclusively prove that defects are annihilated through a cooperative motion of ions.

Further analysis show that most of these replacements take place through the familiar vacancy-interstitial recombination**.** However, a hitherto undiscovered cooperative motion of oxygen ions, which can be regarded as string-like, is shown to play an important role in the dynamic recovery in UO_2 following a radiation impact. The ions participating in a sequential string-like transport mechanism are divided into two groups: initiators, those ions which initiate the string-like motion, and the participants, which include the remaining member ions of the string. It is observed that the initiator ions have, on an average, almost twice the lifetime of the participant ions implying that long-lived defects are more likely to induce a sequential string-like cooperative motion. Further, it is established that the longer an oxygen ion has been displaced to a defect site, the more probable it will be for the ion to get annihilated through a string-like transport mechanism.

Chapter 8: CONCLUSIONS

Superionic or fast ion conductors are multicomponent systems that are characterized by rapid diffusion of one of the ionic species below the melting temperature [1]. Thus superionic materials exhibit exceptional ionic conductivities in the solid state facilitating their utilization in several technologically important applications such as in high-energy-density batteries and fuel cells [135, 136]. Superionic materials are classified into two broad categories depending on the nature of transition to the highly conducting state; Type I conductors exhibit an abrupt jump in the conductivity by several orders of magnitude at a critical temperature that corresponds to a thermodynamic phase change, whereas in Type II conductors, the conductivity rises gradually over a broad temperature range [7]. While there is no noticeable first order phase transformation in Type II conductors, a second order phase transition – also known as superionic or lambda transition [7] – occurs in all Type II conductors, which is manifested as a divergent specific heat at a critical temperature below the melting point (T_λ). While the lambda transition and the associated thermodynamical changes are well-established, the ionic dynamics and the collective behavior that give rise to the pre-melting behavior is less certain.

In the first part of this dissertation, it is shown (from reported neutron scattering and diffraction data) that an order-disorder transition exists at a characteristic temperature (T_α) marking a cross-over from a crystalline state to a partially disordered state. Using molecular dynamics (MD) simulations of UO_2, it is then established that the disordered species (anions) manifest dynamical heterogeneity (DH) – a definitive hallmark of supercooled liquids [15-18]. Using dynamical correlations in propensity (C_d), and self-van-Hove correlations extracted from MD simulations, it is shown that DH grows with increasing temperature from T_α, peaks

at an intermediate temperature between T_α and T_λ and then ebbs at higher temperatures. Not surprisingly, the DH attributes are not uniform across the temperatures – the current investigation shows a low temperature (α_T) stage DH, which is characterized by weak correlations and a plateau-like period in the correlations of the propensity, and a high temperature (λ_T) stage DH with strong correlations that are analogous to those in typical supercooled liquids. This work, which has rigorously identified the onset of superionicity, paves a new direction in understanding the dynamical nature of the superionic state, and in interpreting scattering experiments on the basis of statistical, correlated dynamics.

Similarities between superionics and supercooled liquids, especially, fragile liquids [13] have been reported earlier [11]; the cooperativity among the ions of the disordered species has been likened to that in supercooled liquids approaching glass transition [137]. This correspondence is based on a similar variation of resistivity (inverse of conductivity) for superionics and viscosity for supercooled liquids, and a two-step relaxation in time-correlation functions with an initial fast decay and a stretched-exponential relaxation at longer times. In contrast, the current work has highlighted an importance difference in that the strengthening of DH and cooperativity in supercooled liquids is aided by decreasing entropy, whereas, the DH in superionic conductors evolves against the destabilizing effect of entropy. Thus unlike in supercooled liquids, the DH in superionic conductors waxes and wanes with increasing temperature [84] – a non-linear behavior that is noticeably absent in supercooled liquids.

Atomistic simulations on UO_2 and CaF_2 further confirm that DH in fast ion conductors arises from facilitated dynamics (DF) [113]. Using a mobility transfer function, which gives the probability of a neighbor of a mobile ion becoming mobile relative to that of a random ion becoming mobile, it is shown that mobility propagates continuously to the neighboring ions with the strength of the DF increasing at the order-disorder temperature (T_α), exhibiting a

maximum at an intermediate temperature, and then decreasing as the temperature approaches T_λ. This waxing and waning behavior with temperature is identical to the variation of the correlation in propensity (C_d) that has been used earlier to establish the onset, rise and fall of DH. The close correspondence between DH and DF strongly suggests that DF underpins the heterogeneous dynamics in superionic conductors.

In a dynamically facilitated system, a jammed region can become unjammed only if it is physically adjacent to a mobile region. Remarkably, a string-like displacement of ions, the quintessential mode of particle mobility in jammed systems, is shown to operate in Type II superionics as well. The probability distribution of the length of the string is shown to vary exponentially, which is identical to that observed in supercooled and jammed states. Thus the demonstration of DH, DF and string-like cooperative ionic displacements in superionics establishes Type II superionics as a prototypical jammed system above the O-D transition temperature (T_α) but bounded by the superionic transition temperature (T_λ).

The second part of this dissertation deals with non-equilibrium displacement cascade simulations of UO_2 that is widely used as a nuclear fuel. The radiations from nuclear chain reactions as well as from radioactive decay reactions change the structure and dynamics of the fuel, clad and other structural members over a timespan that ranges from nanoseconds to several years. UO_2 is known to resist amorphization even when subjected to intense nuclear radiations. While analyses based on structure and energy do explain this behavior from a thermodynamic perspective, the dynamical characteristics of the annealing process are largely unknown.

Using non-equilibrium atomistic simulations, it is shown in this dissertation that oxygen ions following a radiation perturbation exhibit correlated motion, which is similar to

that in high temperature superionic state [138]. Quite remarkably, the displaced oxygen ions also undergo fast recovery to their native sites through collective string-like displacements that show an exponential distribution. Interestingly, the ions initiating the string motion have a higher mean lifetime relative to that of the ions, which are simply participating in the string motion. Thus the superionic characteristics of UO_2 under equilibrium conditions are also instrumental in fast defect recovery following a radiation perturbation.

BIBLIOGRAPHY

[1] Chandra, S., *Superionic Solids: Principles and Applications* (North-Holland, 1981).

[2] Faraday, M., Phil. Trans. R. Soc. 90 (1838).

[3] Norby, T., "*The promise of protonics,"* Nature **410**, 877 (2001).

[4] Hayashi, A., Noi, K., Sakuda, A., and Tatsumisago, M., "*Superionic glass-ceramic electrolytes for room-temperature rechargeable sodium batteries,"* Nat. Commun. **3**, 856 (2012).

[5] Chen, P., Xiong, Z. T., Luo, J. Z., Lin, J. Y., and Tan, K. L., "*Interaction of hydrogen with metal nitrides and imides,"* Nature **420**, 302 (2002).

[6] Liu, H., Shi, X., Xu, F., Zhang, L., Zhang, W., Chen, L., Li, Q., Uher, C., Day, T., and Snyder, G. J., "*Copper ion liquid-like thermoelectrics,"* Nat. Mater. **11**, 422 (2012).

[7] Hull, S., "*Superionics: crystal structures and conduction processes,"* Rep. Prog. Phys. **67**, 1233 (2004).

[8] Goff, J. P., Hayes, W., Hull, S., and Hutchings, M. T., "*Neutron powder diffusion study of the fast-ion transition and specific heat anomaly in β-lead fluoride,"* J. Phys.: Condens. Matter **3**, 3677 (1991).

[9] Dickens, M. H., Hayes, W., Hutchings, M. T., and Smith, C., "*Investigation of the structure of strontium chloride at high temperatures using neutron diffraction,"* J. Phys. C: Solid State Phys. **12**, L97 (1979).

[10] Hutchings, M. T., Clausen, K., Dickens, M. H., Hayes, W., Kjems, J. K., Schnabel, P. G., and Smith, C., "*Investigation of thermally induced anion disorder in fluorites using neutron scattering techniques,"* J. Phys. C: Solid State Phys. **17**, 3903 (1984).

[11] Gray-Weale, A. and Madden, P. A., "*Dynamical arrest in superionic crystals and supercooled liquids,"* J. Phys. Chem. B **108**, 6624 (2004).

[12] Gray-Weale, A. and Madden, P. A., "*The energy landscape of a fluorite-structured superionic conductor,"* J. Phys. Chem. B **108**, 6634 (2004).

[13] Angell, C. A., "*Formation of glasses from liquids and biopolymers,"* Science **267**, 1924 (1995).

[14] Kob, W. and Andersen, H. C., "*Scaling behavior in the β-relaxation regime of a supercooled Lennard-Jones mixture,"* Phys. Rev. Lett. **73**, 1376 (1994).

[15] Glotzer, S. C., "*Spatially heterogeneous dynamics in liquids: insights from simulation,"* J. Non-Cryst. Solids **274**, 342 (2000).

[16] Ediger, M. D., "*Spatially heterogeneous dynamics in supercooled liquids,"* Annu. Rev. Phys. Chem. **51**, 99 (2000).

[17] Kegel, W. K. and van Blaaderen, A., "*Direct observation of dynamical heterogeneities in colloidal hard-sphere suspensions,"* Science **287**, 290 (2000).

[18] Dauchot, O., Marty, G., and Biroli, G., "*Dynamical heterogeneity close to the jamming transition in a sheared granular material,"* Phys. Rev. Lett. **95**, 265701 (2005).

[19] Biroli, G. and Garrahan, J. P., "*Perspective: The glass transition,"* J. Phys. Chem. **138**, 12A301 (2013).

[20] Matzke, H. and Whitton, J. L., "*Ion-bombardment-induced radiation damage in some ceramics and ionic crystals - Determined by electron diffraction and gas release measurements,"* Can. J. Phys. **44**, 995 (1966).

[21] Naguib, H. M. and Kelly, R., "*Criteria for bombardment-induced structural changes in non-metallic solids,"* Radiat. Eff. Defects Solids **25**, 1 (1975).

[22] Trachenko, K., "*Understanding resistance to amorphization by radiation damage,"* J. Phys.: Condens. Matter **16**, R1491 (2004).

[23] Hobbs, L. W., "*Topology and geometry in the irradiation-induced amorphization of insulators,"* Nucl. Instrum. Methods Phys. Res., Sect. B **91**, 30 (1994).

[24] Van Brutzel, L., Chartier, A., and Crocombette, J. P., "*Basic mechanisms of Frenkel pair recombinations in UO_2 fluorite structure calculated by molecular dynamics simulations,"* Phys. Rev. B **78**, 024111 (2008).

[25] Sickafus, K. E., Minervini, L., Grimes, R. W., Valdez, J. A., Ishimaru, M., Li, F., McClellan, K. J., and Hartmann, T., "*Radiation tolerance of complex oxides,"* Science **289**, 748 (2000).

[26] Sickafus, K. E., Grimes, R. W., Valdez, J. A., Cleave, A., Tang, M., Ishimaru, M., Corish, S. M., Stanek, C. R., and Uberuaga, B. P., "*Radiation-induced amorphization resistance and radiation tolerance in structurally related oxides,"* Nat. Mater. **6**, 217 (2007).

[27] Pannier, N., Guglielmetti, A., Van Brutzel, L., and Chartier, A., "*Molecular dynamics study of Frenkel pair recombinations in fluorite type compounds,"* Nucl. Instrum. Methods Phys. Res., Sect. B **267**, 3118 (2009).

[28] Chartier, A., Catillon, G., and Crocombette, J.-P., "*Key role of the cation interstitial structure in the radiation resistance of pyrochlores,"* Phys. Rev. Lett. **102**, 155503 (2009).

[29] Lunev, A. V. and Tarasov, B. A., "*A classical molecular dynamics study of the correlation between the Bredig transition and thermal conductivity of stoichiometric uranium dioxide,"* J. Nucl. Mater. **415**, 217 (2011).

[30] Sinnott, S. B. and Uberuaga, B. P., "*Role of atomistic simulations in understanding fission product accommodation in ceramic nuclear fuel,"* Am. Ceram. Soc. Bull. **93**, 28 (2014).

[31] Olander, D. R., *Fundamental Aspects of Nuclear Reactor Fuel Elements* (Technical Information Center, Office of Public Affairs, Energy Research and Development Administration, 1976).

[32] Ewing, R. C., Weber, W. J., and Lian, J., "*Nuclear waste disposal-pyrochlore ($A_2B_2O_7$): Nuclear waste form for the immobilization of plutonium and "minor" actinides,"* J. Appl. Phys. **95**, 5949 (2004).

[33] Matzke, H., Turos, A., and Linker, G., "*Polygonization of single crystals of the fluorite-type oxide UO_2 due to high dose ion implantation,"* Nucl. Instrum. Methods Phys. Res., Sect. B **91**, 294 (1994).

[34] Noirot, J., Desgranges, L., and Lamontagne, J., "*Detailed characterisations of high burn-up structures in oxide fuels,"* J. Nucl. Mater. **372**, 318 (2008).

[35] Sonoda, T., Kinoshita, M., Ray, I. L. F., Wiss, T., Thiele, H., Pellottiero, D., Rondinella, V. V., and Matzke, H., "*Transmission electron microscopy observation on irradiation-induced microstructural evolution in high burn-up UO_2 disk fuel,"* Nucl. Instrum. Methods Phys. Res., Sect. B **191**, 622 (2002).

[36] Sickafus, K. E., in *Comprehensive Nuclear Materials*, edited by R. J. M. Konings (Elsevier, Oxford, 2012), pp. 123.

[37] Born, M. and Oppenheimer, R., "*Quantum theory of molecules,"* Annalen Der Physik **84**, 0457 (1927).

[38] Car, R. and Parrinello, M., "*Unified approach for molecular dynamics and density-functional theory,"* Phys. Rev. Lett. **55**, 2471 (1985).

[39] Yakub, E., Ronchi, C., and Staicu, D., "*Computer simulation of defects formation and equilibrium in non-stoichiometric uranium dioxide,"* J. Nucl. Mater. **389**, 119 (2009).

[40] Basak, C. B., Sengupta, A. K., and Kamath, H. S., "*Classical molecular dynamics simulation of UO_2 to predict thermophysical properties,"* J. Alloys Compd. **360**, 210 (2003).

[41] Gillan, M. J., "*Collective dynamics in superionic CaF_2: I. Simulation compared with neutron-scattering experiment,"* J. Phys. C: Solid State Phys. **19**, 3391 (1986).

[42] Ziegler, J. F., Biersack, J. P., and Littmark, U., *The Stopping and Range of Ions in Solids* (Pergamon, 1985).

[43] Devanathan, R. and Weber, W. J., "*Simulation of collision cascades and thermal spikes in ceramics,"* Nucl. Instrum. Methods Phys. Res., Sect. B **268**, 2857 (2010).

[44] Tuckerman, M., *Statistical Mechanics: Theory and Molecular Simulation* (OUP Oxford, 2010).

[45] Pathria, R. K. and Beale, P. D., *Statistical Mechanics* (Elsevier Science, 1996).

[46] McQuarrie, D. A., *Statistical Mechanics* (Harper & Row, 1976).

[47] Schroeder, D. V., *An Introduction to Thermal Physics* (Addison Wesley, 2000).

[48] Voter, A. F., Montalenti, F., and Germann, T. C., "*Extending the time scale in atomistic simulation of materials,"* Annu. Rev. Mater. Res. **32**, 321 (2002).

[49] Voter, A. F. and Sorensen, M. R., "*Accelerating atomistic simulations of defect dynamics: Hyperdynamics, parallel replica dynamics, and temperature-accelerated dynamics,"* Mat. Res. Soc. Symp. Proc. **538**, 427 (1999).

[50] Sorensen, M. R. and Voter, A. F., "*Temperature-accelerated dynamics for simulation of infrequent events,"* J. Chem. Phys. **112**, 9599 (2000).

[51] Voter, A. F., "*A method for accelerating the molecular dynamics simulation of infrequent events,"* J. Chem. Phys. **106**, 4665 (1997).

[52] Voter, A. F., "*Hyperdynamics: Accelerated molecular dynamics of infrequent events,"* Phys. Rev. Lett. **78**, 3908 (1997).

[53] Voter, A. F., "*Parallel replica method for dynamics of infrequent events,"* Phys. Rev. B **57**, 13985 (1998).

[54] Eyring, H., "*The activated complex in chemical reactions,"* J. Chem. Phys. **3**, 107 (1935).

[55] Wigner, E., "*Concerning the excess of potential barriers in chemical reactions,"* Zeitschrift Fur Physikalische Chemie-Abteilung B-Chemie Der Elementarprozesse Aufbau Der Materie **19**, 203 (1932).

[56] Jonsson, H., Mills, G., and Jacobsen, K. W., *Classical and Quantum Dynamics in Condensed Phased Simulations* (World Scientific, 1998).

[57] Hansen, J. P. and McDonald, I. R., *Theory of Simple Liquids* (Academic Press, 1986).

[58] Rapaport, D. C., *The Art of Molecular Dynamics Simulation* (Cambridge University Press, 2004).

[59] Chaudhuri, P., Berthier, L., and Kob, W., "*Universal nature of particle displacements close to glass and jamming transitions,"* Phys. Rev. Lett. **99**, 060604 (2007).

[60] David, R. R. and Patrick, C., "*Mode-coupling theory,"* J. Stat. Mech.: Theory Exp. P05013 (2005).

[61] Boon, J. P. and Yip, S., *Molecular Hydrodynamics* (Dover Publications, 1980).

[62] March, N. H. and Tosi, M. P., *Introduction to Liquid State Physics* (World Scientific, 2002).

[63] Toninelli, C., Wyart, M., Berthier, L., Biroli, G., and Bouchaud, J. P., "*Dynamical susceptibility of glass formers: Contrasting the predictions of theoretical scenarios,"* Phys. Rev. E **71**, 041505 (2005).

[64] Chandler, D., Garrahan, J. P., Jack, R. L., Maibaum, L., and Pan, A. C., "*Lengthscale dependence of dynamic four-point susceptibilities in glass formers,"* Phys. Rev. E **74**, 051501 (2006).

[65] Widmer-Cooper, A., Harrowell, P., and Fynewever, H., "*How reproducible are dynamic heterogeneities in a supercooled liquid?,"* Phys. Rev. Lett. **93**, 135701 (2004).

[66] Razul, M. S. G., Matharoo, G. S., and Poole, P. H., "*Spatial correlation of the dynamic propensity of a glass-forming liquid,"* J. Phys.: Condens. Matter **23**, 235103 (2011).

[67] Clausen, K., Hayes, W., Macdonald, J. E., Osborn, R., and Hutchings, M. T., "*Observation of oxygen Frenkel disorder in uranium dioxide above 2000 K by use of neutron-scattering techniques,"* Phys. Rev. Lett. **52**, 1238 (1984).

[68] Hull, S., Norberg, S. T., Ahmed, I., Eriksson, S. G., and Mohn, C. E., "*High temperature crystal structures and superionic properties of $SrCl_2$, $SrBr_2$, $BaCl_2$ and $BaBr_2$,"* J. Solid State Chem. **184**, 2925 (2011).

[69] Dickens, M. H., Hayes, W., Hutchings, M. T., and Smith, C., "*Investigation of anion disorder in PbF_2 at high temperatures by neutron diffraction,"* J. Phys. C: Solid State Phys. **15**, 4043 (1982).

[70] Ralph, J. and Hyland, G. J., "*Empirical confirmation of a Bredig transition in UO_2,"* J. Nucl. Mater. **132**, 76 (1985).

[71] Yakub, E., Ronchi, C., and Staicu, D., "*Molecular dynamics simulation of premelting and melting phase transitions in stoichiometric uranium dioxide,"* J. Chem. Phys. **127**, 094508 (2007).

[72] Hutchings, M. T., "*High-temperature studies of UO_2 and ThO_2 using neutron scattering techniques,"* J. Chem. Soc., Faraday Trans. 2 **83**, 1083 (1987).

[73] Ruello, P., Desgranges, L., Baldinozzi, G., Calvarin, G., Hansen, T., Petot-Ervas, G., and Petot, C., "*Heat capacity anomaly in UO_2 in the vicinity of 1300 K: an improved description based on high resolution X-ray and neutron powder diffraction studies,"* J. Phys. Chem. Solids **66**, 823 (2005).

[74] Voronin, B. M. and Volkov, S. V., "*Ionic conductivity of fluorite type crystals CaF_2, SrF_2, BaF_2, and $SrCl_2$ at high temperatures,"* J. Phys. Chem. Solids **62**, 1349 (2001).

[75] Comins, J. D., Ngoepe, P. E., and Catlow, C. R. A., "*Brillouin-scattering and computer-simulation studies of fast-ion conductors: A review,"* J. Chem. Soc., Faraday Trans. **86**, 1183 (1990).

[76] Govers, K., Lemehov, S., Hou, M., and Verwerft, M., "*Comparison of interatomic potentials for UO_2. Part I: Static calculations,"* J. Nucl. Mater. **366**, 161 (2007).

[77] Devanathan, R., Yu, J., and Weber, W. J., "*Energetic recoils in UO_2 simulated using five different potentials,"* J. Chem. Phys. **130**, (2009).

[78] Taller, S. A. and Bai, X.-M., "*Assessment of structures and stabilities of defect clusters and surface energies predicted by nine interatomic potentials for UO_2,"* J. Nucl. Mater. **443**, 84 (2013).

[79] Murphy, S. T., Rushton, M. J. D., and Grimes, R. W., "*A comparison of empirical potential models for the simulation of dislocations in uranium dioxide,"* Prog. Nucl. Energy **72**, 27 (2014).

[80] Ida, Y., "*Interionic repulsive force and compressibility of ions,"* Phys. Earth Planet. Inter. **13**, 97 (1976).

[81] Potashnikov, S. I., Boyarchenkov, A. S., Nekrasov, K. A., and Kupryazhkin, A. Y., "*High-precision molecular dynamics simulation of UO_2-PuO_2: Pair potentials comparison in UO_2,"* J. Nucl. Mater. **419**, 217 (2011).

[82] Wolf, D., Keblinski, P., Phillpot, S. R., and Eggebrecht, J., "*Exact method for the simulation of Coulombic systems by spherically truncated, pairwise r^{-1} summation,"* J. Chem. Phys. **110**, 8254 (1999).

[83] Wendt, H. R. and Abraham, F. F., "*Empirical criterion for glass transition region based on Monte Carlo simulations,"* Phys. Rev. Lett. **41**, 1244 (1978).

[84] Annamareddy, V. A., Nandi, P. K., Mei, X., and Eapen, J., "*Waxing and waning of dynamical heterogeneity in the superionic state,"* Phys. Rev. E **89**, 010301(R) (2014).

[85] Nield, V. M. and Keen, D. A., *Diffuse Neutron Scattering from Crystalline Materials* (Clarendon Press, 2001).

[86] Ngai, K. L., "*An extended coupling model description of the evolution of dynamics with time in supercooled liquids and ionic conductors,"* J. Phys.: Condens. Matter **15**, S1107 (2003).

[87] Ngai, K. L., Habasaki, J., Leon, C., and Rivera, A., "*Comparison of dynamics of ions in ionically conducting materials and dynamics of glass-forming substances: Remarkable similarities,"* Z. Phys. Chem. **219**, 47 (2005).

[88] Keys, A. S., Hedges, L. O., Garrahan, J. P., Glotzer, S. C., and Chandler, D., "*Excitations are localized and relaxation is hierarchical in glass-forming liquids,"* Phys. Rev. X **1**, 021013 (2011).

[89] Glotzer, S. C., Novikov, V. N., and Schroder, T. B., "*Time-dependent, four-point density correlation function description of dynamical heterogeneity and decoupling in supercooled liquids,"* J. Chem. Phys. **112**, 509 (2000).

[90] Dalle-Ferrier, C., Thibierge, C., Alba-Simionesco, C., Berthier, L., Biroli, G., Bouchaud, J. P., Ladieu, F., L'Hote, D., and Tarjus, G., "*Spatial correlations in the dynamics of glassforming liquids: Experimental determination of their temperature dependence,"* Phys. Rev. E **76**, 041510 (2007).

[91] Karmakar, S., Dasgupta, C., and Sastry, S., "*Analysis of dynamic heterogeneity in a glass former from the spatial correlations of mobility,"* Phys. Rev. Lett. **105**, 015701 (2010).

[92] Karmakar, S., Dasguptaa, C., and Sastry, S., "*Growing length and time scales in glass-forming liquids,"* Proc. Natl. Acad. Sci. U.S.A. **106**, 3675 (2009).

[93] Berthier, L. and Kob, W., "*The Monte Carlo dynamics of a binary Lennard-Jones glass-forming mixture,"* J. Phys.: Condens. Matter **19**, 205130 (2007).

[94] Widmer-Cooper, A., Perry, H., Harrowell, P., and Reichman, D. R., "*Irreversible reorganization in a supercooled liquid originates from localized soft modes,"* Nat. Phys. **4**, 711 (2008).

[95] Kob, W. and Andersen, H. C., "*Testing mode-coupling theory for a supecooled binary Lennard-Jones mixture. II. Intermediate scattering function and dynamic susceptibility,"* Phys. Rev. E **52**, 4134 (1995).

[96] Mei, X. and Eapen, J., "*Dynamic transitions in molecular dynamics simulations of supercooled silicon,"* Phys. Rev. B **87**, (2013).

[97] Matharoo, G. S., Razul, M. S. G., and Poole, P. H., "*Structural and dynamical heterogeneity in a glass-forming liquid,"* Phys. Rev. E **74**, 050502(R) (2006).

[98] Kob, W. and Andersen, H. C., "*Testing mode-coupling theory for a supercooled binary Lennard-Jones mixture: The van Hove correlation function,"* Phys. Rev. E **51**, 4626 (1995).

[99] Karmakar, S., Dasgupta, C., and Sastry, S., "*Growing length scales and their relation to timescales in glass-forming liquids,"* Annu. Rev. Condens. Matter Phys. **5**, 255 (2014).

[100] Stevenson, J. D., Schmalian, J., and Wolynes, P. G., "*The shapes of cooperatively rearranging regions in glass-forming liquids,"* Nat. Phys. **2**, 268 (2006).

[101] Berthier, L. and Biroli, G., "*Theoretical perspective on the glass transition and amorphous materials,"* Rev. Mod. Phys. **83**, 587 (2011).

[102] Chandler, D. and Garrahan, J. P., "*Dynamics on the way to forming glass: Bubbles in space-time,"* Annu. Rev. Phys. Chem. **61**, 191 (2010).

[103] Gebremichael, Y., Vogel, M., and Glotzer, S. C., "*Particle dynamics and the development of string-like motion in a simulated monoatomic supercooled liquid,"* J. Chem. Phys. **120**, 4415 (2004).

[104] Garrahan, J. P. and Chandler, D., "*Geometrical explanation and scaling of dynamical heterogeneities in glass forming systems,"* Phys. Rev. Lett. **89**, 035704 (2002).

[105] Garrahan, J. P. and Chandler, D., "*Coarse-grained microscopic model of glass formers,"* Proc. Natl. Acad. Sci. U.S.A. **100**, 9710 (2003).

[106] Stillinger, F. H. and Hodgdon, J. A., "*Translation-rotation paradox for diffusion in fragile glass-forming liquids,"* Phys. Rev. E **50**, 2064 (1994).

[107] Bhattacharyya, S. M., Bagchi, B., and Wolynes, P. G., "*Facilitation, complexity growth, mode coupling, and activated dynamics in supercooled liquids,"* Proc. Natl. Acad. Sci. U.S.A. **105**, 16077 (2008).

[108] Vogel, M. and Glotzer, S. C., "*Spatially heterogeneous dynamics and dynamic facilitation in a model of viscous silica,"* Phys. Rev. Lett. **92**, 255901 (2004).

[109] Bergroth, M. N. J., Vogel, M., and Glotzer, S. C., "*Examination of dynamic facilitation in molecular dynamics simulations of glass-forming liquids,"* J. Phys. Chem. B **109**, 6748 (2005).

[110] Gokhale, S., Nagamanasa, K. H., Ganapathy, R., and Sood, A. K., "*Growing dynamical facilitation on approaching the random pinning colloidal glass transition,"* Nat. Commun. **5**, 4685 (2014).

[111] Elmatad, Y. S. and Keys, A. S., "*Manifestations of dynamical facilitation in glassy materials,"* Phys. Rev. E **85**, 061502 (2012).

[112] Mishra, C. K., Nagamanasa, K. H., Ganapathy, R., Sood, A. K., and Gokhale, S., "*Dynamical facilitation governs glassy dynamics in suspensions of colloidal ellipsoids,"* Proc. Natl. Acad. Sci. U.S.A. **111**, 15362 (2014).

[113] Annamareddy, A. and Eapen, J., "*Mobility propagation and dynamic facilitation in superionic conductors,"* J. Chem. Phys. **143**, 194502 (2015).

[114] Gebremichael, Y., Vogel, M., Bergroth, M. N. J., Starr, F. W., and Glotzer, S. C., "*Spatially heterogeneous dynamics and the Adam-Gibbs relation in the Dzugutov liquid,*" J. Phys. Chem. B **109**, 15068 (2005).

[115] Starr, F. W., Douglas, J. F., and Sastry, S., "*The relationship of dynamical heterogeneity to the Adam-Gibbs and random first-order transition theories of glass formation,*" J. Chem. Phys. **138**, 12A541 (2013).

[116] Murch, G. E., "*The Haven ratio in fast ionic conductors,*" Solid State Ionics **7**, 177 (1982).

[117] Yokota, I., "*On deviation from Einstein relation observed for diffusion of Ag^+ ions in α-Ag_2S and others,*" J. Phys. Soc. Jpn. **21**, 420 (1966).

[118] Okazaki, H., "*Deviation from the Einstein relation in average crystals self-diffusion of Ag^+ ions in α-Ag_2S and α-Ag_2Se,*" J. Phys. Soc. Jpn. **23**, 355 (1967).

[119] Weeks, E. R., Crocker, J. C., Levitt, A. C., Schofield, A., and Weitz, D. A., "*Three-dimensional direct imaging of structural relaxation near the colloidal glass transition,*" Science **287**, 627 (2000).

[120] Zhang, H., Srolovitz, D. J., Douglas, J. F., and Warren, J. A., "*Grain boundaries exhibit the dynamics of glass-forming liquids,*" Proc. Natl. Acad. Sci. U.S.A. **106**, 7735 (2009).

[121] Keys, A. S., Abate, A. R., Glotzer, S. C., and Durian, D. J., "*Measurement of growing dynamical length scales and prediction of the jamming transition in a granular material,*" Nat. Phys. **3**, 260 (2007).

[122] Plimpton, S., "*Fast parallel algorithms for short-range molecular dynamics,*" J. Comput. Phys. **117**, 1 (1995).

[123] Donati, C., Douglas, J. F., Kob, W., Plimpton, S. J., Poole, P. H., and Glotzer, S. C., "*Stringlike cooperative motion in a supercooled liquid,"* Phys. Rev. Lett. **80**, 2338 (1998).

[124] Devanathan, R., Weber, W. J., and de la Rubia, T. D., "*Computer simulation of a 10 keV Si displacement cascade in SiC,"* Nucl. Instrum. Methods Phys. Res., Sect. B **141**, 118 (1998).

[125] Weber, W. J., "*Models and mechanisms of irradiation-induced amorphization in ceramics,"* Nucl. Instrum. Methods Phys. Res., Sect. B **166**, 98 (2000).

[126] Jiang, C., Zheng, M. J., Morgan, D., and Szlufarska, I., "*Amorphization driven by defect-induced mechanical instability,"* Phys. Rev. Lett. **111**, 155501 (2013).

[127] Snead, L. L., Zinkle, S. J., Hay, J. C., and Osborne, M. C., "*Amorphization of SiC under ion and neutron irradiation,"* Nucl. Instrum. Methods Phys. Res., Sect. B **141**, 123 (1998).

[128] Dickens, M. H., Hayes, W., Schnabel, P., Hutchings, M. T., Lechner, R. E., and Renker, B., "*Incoherent quasielastic neutron scattering investigation of chlorine ion hopping in the fast-ion phase of strontium chloride,"* J. Phys. C: Solid State Phys. **16**, L1 (1983).

[129] Jacucci, G. and Rahman, A., "*Diffusion of F^- ions in CaF_2,"* J. Chem. Phys. **69**, 4117 (1978).

[130] Van Brutzel, L., Delaye, J. M., Ghaleb, D., and Rarivomanantsoa, M., "*Molecular dynamics studies of displacement cascades in the uranium dioxide matrix,"* Philos. Mag. **83**, 4083 (2003).

[131] Van Brutzel, L. and Rarivomanantsoa, M., "*Molecular dynamics simulation study of primary damage in UO_2 produced by cascade overlaps,"* J. Nucl. Mater. **358**, 209 (2006).

[132] Reif, F., *Fundamentals of Statistical and Thermal Physics* (McGraw-Hill, 1965).

[133] Uberuaga, B. P., Jiang, C., Stanek, C. R., Sickafus, K. E., Scott, C., and Smith, R., "*Prediction of irradiation spectrum effects in pyrochlores,"* JOM **66**, 2578 (2014).

[134] Stukowski, A., "*Visualization and analysis of atomistic simulation data with OVITO-the Open Visualization Tool,"* Modell. Simul. Mater. Sci. Eng. **18**, 015012 (2010).

[135] Kendrick, E. and Slater, P., "*Battery and solid oxide fuel cell materials,"* Annu. Rep. Prog. Chem. Sect. A: Inorg. Chem. **108**, 424 (2012).

[136] Kamaya, N., Homma, K., Yamakawa, Y., Hirayama, M., Kanno, R., Yonemura, M., Kamiyama, T., Kato, Y., Hama, S., Kawamoto, K., and Mitsui, A., "*A lithium superionic conductor,"* Nat. Mater. **10**, 682 (2011).

[137] Adam, G. and Gibbs, J. H., "*On temperature dependence of cooperative relaxation properties in glass-forming liquids,"* J. Chem. Phys. **43**, 139 (1965).

[138] Annamareddy, V. A., Mei, X., and Eapen, J., "*Dynamical recovery in UO_2 following radiation impact,"* Trans. Am. Nucl. Soc. **110**, 967 (2014).